Control of Synchrotron X-ray Emission from Laser Wakefield Accelerators

by

Zhen Zhao

A dissertation submitted in partial fulfillment
of the requirements for the degree of
Doctor of Philosophy
(Nuclear Engineering and Radiological Sciences)
in The University of Michigan
2016

Doctoral Committee:

Professor Karl M. Krushelnick, Chair
Professor Almantas Galvanauskas
Research Scientist Anatoly Maksimchuk
Research Scientist John A. Nees
Associate Professor Alexander G. R. Thomas

“Be patient toward all that is unsolved in your heart and try to love the questions themselves, like locked rooms and like books that are now written in a very foreign tongue. Do not now seek the answers, which cannot be given you because you would not be able to live them. And the point is, to live everything. Live the questions now. Perhaps you will then gradually, without noticing it, live along some distant day into the answer.”

-*Rainer Maria Rilke*

For my mom, who never let me forget the value of education

For my wife, who has always reminded me of who I am

For Gatsby and Layla, may they never grow old

ACKNOWLEDGEMENTS

The work presented in this dissertation is the result borne from the herculean efforts of many, many people. None of this would have been possible without the guidance and mentorship of my advisor, Karl Krushelnick—thank you for giving me the opportunity and freedom to explore the exciting world of high field science. To Alec, I truly appreciated your buddhist-like patience and unhesitating attitude in helping me think through problems. I am forever grateful to the both of you.

Of course none of the research would have been possible without the HERCULES and Lambda Cubed laser staff. Thank you John Nees and Bixue Hou for showing me the ropes and getting my feet wet in Lambda Cubed. The two of you generated the spark that kept me interested and curious about the experiments. Thank you Tolya for continuously pushing me to excel in HERCULES and teaching me how to do things right the first time around. A special recognition is in order for Victor Yanovsky who has dedicated an immense amount of time and effort to the HFS group and in particular, to the operation and maintenance of the HERCULES laser system. I hope that wind surfing is in your near future.

I would also like to thank all the HFS students and graduates who have helped me with my research and made the last five years an enjoyable, once-in-a-lifetime experience. To Will, thank you for being a mentor and giving me survival tips in HERCULES; without you, things would've been a lot more painful. To Keegan, if I didn't have someone else sitting next to me during the long shot runs or standing across from me at the gas target chamber, I don't think I would've made it this long or, at the very least, I would've had some serious back pain. To Thomas, I had a great time working with you in Lambda Cubed; thanks for the unlimited hand sanitizer. Anthony, thanks for introducing me to the wonderful world of Arduino and Raspberry Pi—one day, our homes will be fully automated for a reasonable price. Jason Cole and Jonathon Wood, thank you for your help in setting up the initial two-beam experiments in the gas target chamber and making me feel welcome throughout the various Astra Gemini experiments. Darragh Corvan, you are a kindred spirit and I'll never forget the Irish countryside and my first true pint of Guinness. Mahmoad, thank you for your generosity and friendship—I hope that there will always be enjoyable places for you to take your long walks. There are so many other people that I haven't acknowledged yet but, alas, I have to write the rest of this thesis.

TABLE OF CONTENTS

CHAPTER

LIST OF FIGURES

Figure

LIST OF TABLES

Table

LIST OF APPENDICES

Appendix

LIST OF ABBREVIATIONS

ASE amplified spontaneous emission

BSI barrier suppression ionization

CCD charge coupled device

CLIC Compact Linear Collider

CPA Chirped Pulse Amplification

CUOS Center for Ultrafast Optical Science

EPROFILE electron spatial profile

ESPEC electron spectrometer

FROG frequency resolved optical gating

FWHM full width at half maximum

GVD group velocity dispersion

HERCULES High Energy Repetitive CUOS LasEr System

ICF inertial confinement fusion

LINAC linear accelerators

LPA laser plasma acceleration

LWFA Laser Wakefield Acceleration or Accelerator

OPA optical parametric amplifier

OP-CPA optical parametric chirped pulse amplification

PIC Particle-in-Cell

PMT photo-multiplier tubes

PSL photo-stimulated luminescence

PWFA Plasma Wakefield Acceleration or Accelerator

QE quantum efficiency

RF radio frequency

RFS Raman forward scattering

RMS root mean square

SHG second harmonic generation

SM-LWFA self-modulated laser wakefield acceleration

SPC single photon counting

SPM self-phase modulation

SRS stimulated Raman scattering

Ti:Sapphire Titanium-doped Sapphire

TRPE total radiated photon energy

USUI ultra-short, ultra-intense

XFEL X-ray Free Electron Laser

XPW cross-polarized wave

ABSTRACT

Control of Synchrotron X-ray Emission from Laser Wakefield Accelerators

by

Zhen Zhao

Chair: Karl M. Krushelnick

When a short-pulse, high-intensity laser irradiates a gas target, plasma is produced and electrons are accelerated to high energies due to the electric field of the laser. Irradiation of the gas produces plasma waves capable of accelerating electrons that emit high energy X-rays in the laser wakefield acceleration regime. The properties of the radiation are linked to those of the electron beam and the laser pulse parameters. Thus, efficient X-ray production requires efficient methods of injecting electrons into the wakefield and accelerating them afterwards. This thesis describes experimental and numerical work aimed at optimizing the electron generation process as well as the resulting X-ray emission using low density plasmas. Experiments were primarily carried out using the petawatt-class High Energy Repetitive CUOS LasEr System (HERCULES) at the University of Michigan.

The electron injection process into the wakefield is influenced by the drive pulse parameters. Experiments were conducted to study the combined effect of the laser pulse duration, pulse shape, and frequency chirp on the electron injection and acceleration process and the associated radiation emission for two different gas types: a 97.5% He and 2.5% N_2 mixture and pure He. In general, the shortest pulse duration

produced the highest energy and highest charge electron beams. Positively chirped pulses injected more electrons compared with pulses that were negatively chirped. A similar trend was observed for the photon flux. The relationship between the total radiated photon energy (TRPE) and the electron charge followed a linear trend over more than a threefold change in the electron density and was independent of the drive pulse characteristics. The sychrotron spectra showed that ionization injection of electrons using the mixed gas generally produced more photons than self-injection using the pure He for all pulse durations/frequency chirps and had a smaller spread in the number of photons around the peak X-ray energy.

New methods of electron generation and X-ray emission enhancement were demonstrated as well. First, control of the electron beam phase space structure was achieved by altering both the plasma density profile and laser pulse parameters. Specifically, the combination of trapping electrons using the technique of downramp injection and driving the laser wakefield using long-duration, positively chirped pulses led to the generation of a two-component electron beam. Almost an order of magnitude increase in the synchrotron radiation emission per unit electron charge was observed due to the large-amplitude transverse oscillations of the annular component of the electron beam. Numerical simulations were conducted to better understand the conditions under which these two-component beams can be created.

Secondly, experiments were conducted to show that the X-ray emission can be increased by taking advantage of a naturally occurring instability in a laser wakefield accelerator—namely, the electron hosing instability. This instability occurs due to the electron beam interacting with the laser pulse at long interaction lengths ($4-6$ mm) in the plasma and subsequently undergoing violent oscillations in the laser polarization direction, leading to an increase in the X-ray emission.

Finally, we demonstrated the ability to consistently generate dual and triple electron beams simultaneously by using two focal spots for the laser. These electron

beams are injected (and subsequently accelerated) into co-propagating wakefields. Measurements of the electron spectra show evidence of a delay in beam-loading, interaction between the wakefields that lead to the acceleration of a third electron beam, and uncharacteristically large-amplitude transverse oscillations in the electron beams. These large oscillations are a promising source for increasing the overall X-ray emission.

CHAPTER I

Introduction

1.1 Motivation

Since the discovery of X-rays in 1896 by Wilhelm Conrad Röentgen [1], their use as a diagnostic tool has assumed an increasingly important role in science, medicine, and technology. In the past fifty years, advances in modern accelerator technologies has enabled the generation of relativistic particle beams that emit X-ray radiation. For example, the SLAC National Accelerator Laboratory has accelerated electrons and positrons with energies up to 50 GeV and produced X-rays with femtosecond pulse duration with energies in the range $0.25 - 9.5$ keV, while operating at a 120 Hz repetition rate [2]. The European X-ray Free Electron Laser (XFEL), scheduled for experiments starting 2017, will be able to operate in the kilohertz regime and produce coherent X-rays with energies up to 25 keV [3]. These accelerated particles and X-rays are used extensively in areas such as the study of matter in extreme environments, understanding the dynamics of biological specimens, and probing motion on the atomic level.

While these technologies are relatively well-understood and mature, there are some limiting factors associated with their use. First among these is the maximum accelerating gradient that can be achieved in the radio frequency (RF) cavities. This gradient is on the order of tens of MV/m, even with the use of superconducting

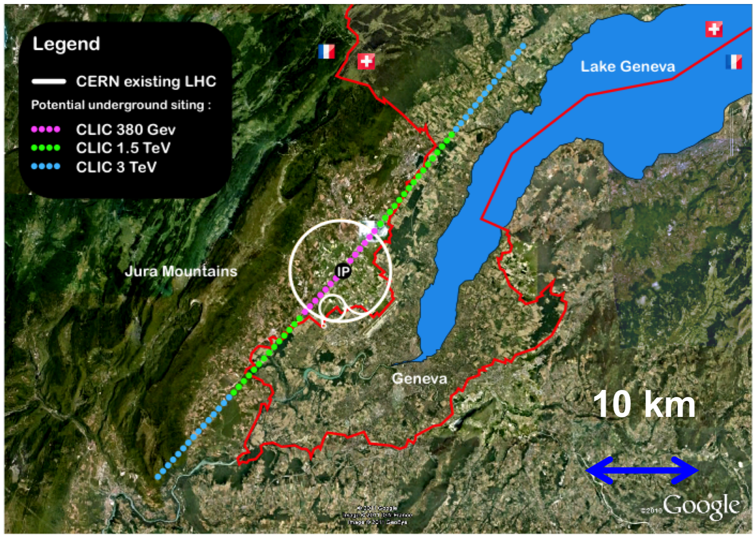

Figure 1.1: Aerial view of the proposed CLIC showing the different stages of the two-beam acceleration scheme. Figure from Ref. [6].

accelerating cavities [4]—a fundamental limit due to the onset of electric breakdown of the cavity material. Another issue is their physical size and construction cost, which is on the order of kilometers and billions of dollars, respectively. For example, the length of the main accelerator for the proposed Compact Linear Collider (CLIC) is 42 km (Fig. 1.1) and has 43 institutes from 22 countries participating in the project so far [5].

The advent of short-pulse, high-intensity laser systems in the past decade has made possible the development of high accelerating gradient schemes by using an ionized medium (i.e., a plasma) as the conducting material. These laser systems offer the unique capability to generate and control plasmas and to accelerate particles in a laboratory-scale environment at a fraction of the cost of conventional accelerator facilities. The properties of the plasma are also primarily determined by the laser pulse and the background density. This is significant since it allows for control of the plasma by simply manipulating the laser pulse parameters. In addition, the existence of strong electric fields (due to the separation of positive and negative charges within the plasma) makes it an ideal environment for accelerating particles to relativistic energies which can then be used to generate high energy radiation bursts. Because the properties of the resulting radiation are directly linked to those of the particles, the ability to generate these particles efficiently is paramount in producing high-quality X-rays.

1.2 High-intensity lasers

The short-pulse laser-plasma community is primarily concerned with the study of nonlinear optical phenomena and/or physics under extreme conditions, and high-intensity lasers are capable of creating these conditions in a laboratory-scale setting. The experiments are typically conducted in the ultra-short, ultra-intense (USUI) regime, where the temporal duration of the pulse ranges from $\sim$ 10 fs to 10 ps and the peak irradiance is greater than 10^{17} W/cm^2. In order to achieve these irradiances without detrimental effects such as nonlinear optical distortion or damage to the system optics, a technique called Chirped Pulse Amplification (CPA) is employed [7]. In CPA, a low-energy, short pulse is temporally stretched using a grating pair and amplified to high energies, prior to being compressed back to a duration similar to its input. Thus, a high-energy, short-duration pulse is produced at the output of the system. After the application of CPA to optical amplifiers, the peak irradiances at the focus of these laser pulses essentially skyrocketed and allowed new science to be explored at each step of the way as shown in Fig. 1.2. In addition, CPA made it possible to reduce the size and cost of these laser systems.

The electric field strengths of these lasers, when they are focused, can be orders of magnitude higher than the ionization energy of bound electrons in the target material. Thus, any target placed at the focus of the laser pulse will undergo rapid ionization and form a plasma. The interaction and evolution of the laser pulse and plasma differ significantly depending on the irradiated material. For solid targets, an inhomogeneous, dense plasma is formed near the target surface, which prevents the

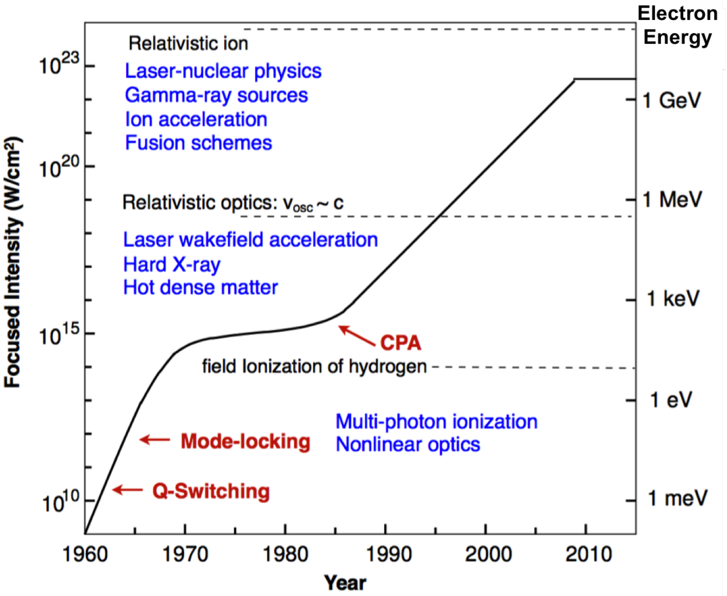

Figure 1.2: Peak laser irradiance vs. year. The application of CPA allowed higher peak irradiances to be achieved, paving the way for new science to be explored. Figure adapted from Ref. [8].

laser pulse from propagating further into the material. A portion of the laser energy is coupled into energetic electrons that propagate into the target and generate characteristic line emission and bremsstrahlung radiation. For gas targets, the complete separation of ions and electrons in the plasma sets up large electric fields that are capable of accelerating electrons to relativistic energies in just a few centimeters. In this laser-produced low-density plasma, electrons gain energy from large-amplitude plasma waves similar to how a surfer picks up energy from an ocean wave. The electron beam can become trapped behind the propagating laser pulse and emit highly collimated, bright X-rays as it is accelerated. This type of acceleration scheme is known as laser plasma acceleration (LPA).

The accelerated electron beam has desirable qualities such as a quasimonoenergetic energy spread with peak energies in the GeV range, high charge, low beam emittance, and very short pulse duration while the X-rays have high peak brightness. This is due to the fact that the plasma wakefield and phase space structure of the electrons evolve synchronously with the laser pulse. Many experiments have demonstrated the production of quasimonoenergetic, high-energy electrons along with the emission of high-brightness X-rays in a centimeter length plasma [9–13].

However, these laser systems come with their own disadvantages as well. Most ultra-short laser systems achieve amplification using either a multipass amplifier or regenerative amplifier in the near-infrared part of the electromagnetic spectrum. For terawatt or petawatt class lasers, many stages of amplification are usually required with the necessity of increasing beam size with each pass through the amplifiers, since even a stretched pulse will eventually exceed the damage threshold of the system optics. Thus, a limiting factor for the further development of CPA lasers is the beam size since the optics must also increase in size in order to accommodate these beams. Energy efficiency is also a drawback for laser-plasma technologies. For example, the "wall-plug" energy efficiency of flashlamp-pumped lasers similar to the ones used on the HERCULES laser system is typically $\leq 1\%$. A portion of the laser energy is also used to create the plasma and can be lost to various laser/plasma instabilities rather than accelerating the particles. The energy spread of the particles and the stability of the system is also poor compared with those obtained from conventional accelerators. Due to current technological constraints, most petawatt-class lasers operate in single-shot mode as opposed to the kilohertz repetition rate of most linear accelerators (LINAC).

Challenges exist in efficiently generating and accelerating electrons using high-intensity lasers due to the complex and nonlinear evolution of the electron beam. Also, as the demand for higher energy and repetition rate lasers increases, additional complexities arise in managing the cost, energy, and radiation emission of these systems. This thesis investigates the effects of the laser and plasma parameters on the laser wakefield process and the subsequent creation of the electron beams and X-rays.

1.3 Dissertation outline

The outline of the thesis is as follows:

- Chapter II provides an introduction to the pertinent physics behind high-intensity laser interactions, including topics covering laser physics, laser-plasma interactions, laser pulse propagation in an underdense plasma, and radiation generation.

- Chapter III describes the HERCULES laser system, experimental setups, the primary diagnostics, and the experimental methods used in this thesis.

- Chapter IV focuses on work conducted to investigate the effects of the laser pulse parameters on the electron beam injection and acceleration process as well as the resulting synchrotron radiation emission in the Laser Wakefield Acceleration or Accelerator (LWFA) regime using the HERCULES laser system.

- Chapter V demonstrates a unique method of electron beam phase space control that relies on manipulating both the density profile and laser pulse parameters, resulting in the injection and acceleration of a two-component electron beam with almost an order of magnitude increase in the TRPE per unit electron charge.

- Chapter VI presents an enhancement in the synchrotron emission due to an instability of the electron beam in the wakefield cavity that is seeded by an interaction with the laser pulse in a LWFA.

- Chapter VII details work on the generation of multiple electron beams injected into and accelerated by simultaneously co-propagating wakefields produced using dual laser focal spots.

- Chapter VIII concludes with an overview of the work done in this thesis and offers an outlook on the development of laser plasma-based accelerators to generate and control relativistic electron beams and high-energy radiation.

CHAPTER II

Physics of High-Intensity Laser-Plasma Interactions

In high-intensity laser interactions with matter, the underlying physics is essentially dictated by the subsequent motion of the electrons in the plasma created by the laser field. This chapter covers the theoretical basis for laser interactions in underdense plasmas, starting with the different ways a plasma can be created and concluding with the radiation emitted during these events. A more detailed version of the relevant physics can be found in Refs. [8, 14–20] . A discussion on ultrafast optics, as it pertains to the experimental results presented in this thesis, is also given at the end.

2.1 Ionization mechanisms

In order to create a plasma, an atomic electron must first become separated from its parent atom. There are several different mechanisms by which a medium can be ionized. Perhaps the most straightforward method of ionization is via the photoelectric effect as predicted by Einstein over a century ago [21]. This process occurs when energy from an incident photon is directly transferred to an electron within a material. If the photon energy is on the order of the ionization potential which the electron experiences in the vicinity of the ion, then the electron can be ejected from the atom. For typical metals, this requires a photon energy of at least several electron volts. This is higher than the energy available from most conventional lasers due to their operating wavelengths (0.25 μm - 13.4 μm) and thus, photoionization does not play a relevant role in most high-intensity laser experiments.

As the intensity of the lasers grew in the 1960s and 1970s, it became possible to consider nonlinear ionization methods. The electric field strength in a hydrogen atom at the Bohr radius is given by,

$$E_a = \frac{e}{4\pi\epsilon_0 a_B^2} \simeq 5.1 \times 10^9 \quad [\mathrm{Vm}^{-1}] \tag{2.1}$$

where e is the electron charge, ϵ_0 is the permittivity of free space, and a_B is the Bohr radius. From this, we can calculate the time-averaged intensity that matches this field strength,

$$I_a = \frac{\epsilon_0 c E_a^2}{2} \simeq 3.51 \times 10^{16} \quad [\mathrm{Wcm}^{-2}] \tag{2.2}$$

where c is the speed of light and I_a is the intensity at which the laser field matches the binding strength of the electron to the atom. Thus, if the intensity of a laser exceeds I_a, then any target material will become ionized. In fact, ionization occurs at intensities well below this value due to multiphoton ionization, a nonlinear phenomena predicted by Göppert-Mayer in the early 1930s [22] with some of the pioneering work done by the group of Mainfray and Manus in the 1990s [23]. In multiphoton ionization, an electron can be ejected from an atom if the light intensity is high enough ($I \sim 10^{11}$ W/cm^2) via simultaneous absorption of several photons. The n-photon ionization rate (for the case when $I_L \ll I_a$, where I_L is the laser intensity) is given by,

$$\Gamma_n = \sigma_n I_L^n \tag{2.3}$$

where σ_n is the interaction cross-section, and I_L is the laser intensity. Although the cross section, σ_n, decreases with n, the I_L^n dependence ensures that ionization will occur at sufficiently high intensities.

As the intensity of the laser increases, the Coulomb potential of the atom can become disturbed in such a way that an electron can tunnel through the Coulomb barrier. The atom then becomes ionized via tunneling ionization. The parameter that separates the regimes of multiphoton and tunneling ionization is given by the Keldysh parameter [24],

$$\gamma_K = \frac{\text{Tunneling Time}}{\text{Laser Period}} = \omega_L \frac{\sqrt{2m_e E_{ion}}}{eE_0} \tag{2.4}$$

where ω_L is the angular frequency of the laser, m_e is the electron mass, E_{ion} is the ionization energy, and E_0 is the laser field. From this equation, one can deduce that tunneling ionization is dominant when $\gamma_K \ll 1$ and vice versa for multiphoton ionization.

When the laser field becomes sufficiently strong, the electron can spontaneously escape from the Coulomb barrier. This is known as barrier suppression ionization (BSI) or direct field ionization and becomes significant when the entire Coulomb barrier is below the energy of the electron state and the electron is no longer bound. The intensity at which BSI dominates is given by,

$$I_{app} = \frac{cE_{ion}^4}{128\pi Z^2 e^6} \simeq 4 \times 10^9 \left(\frac{E_{ion}}{[eV]}\right)^4 Z^{-2} \quad [\mathrm{Wcm^{-2}}] \tag{2.5}$$

where Z is the atomic number and I_{app} is known as the appearance intensity. A schematic of the various ionization processes is shown in Fig. 2.1. For the intensities relevant to this thesis, ionization occurs due to the tunneling effect and BSI at the peak of the laser pulse. The appearance intensities for the two gas types used in the experiments are shown in Fig. 2.2.

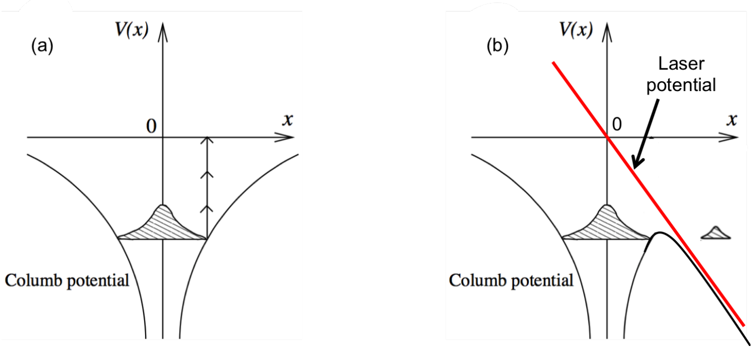

Figure 2.1: (a) Multiphoton ionization process whereby an electron with binding energy E_{ion} is released from an atom after absorbing n photons. (b) Tunneling/BSI where the laser electric field is capable of distorting the Coulomb potential, allowing the electron to either tunnel out of the Coulomb barrier or escape spontaneously via BSI. Figure adapted from Ref. [8].

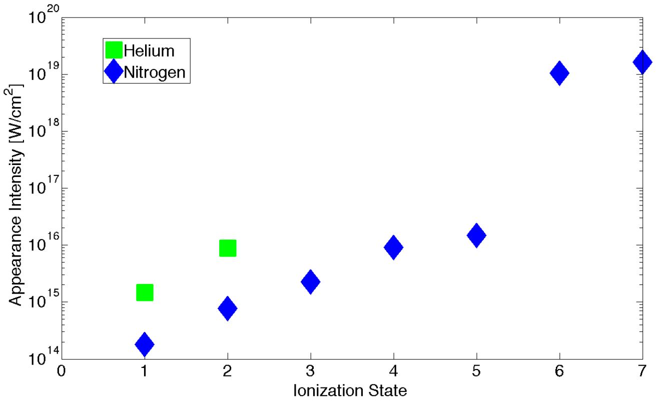

Figure 2.2: Appearance intensities for field ionization of helium and nitrogen using the BSI model.

Another form of ionization that can occur is collisional (avalanche) ionization. In this scheme, fast electrons that are quivering in the laser field undergo inelastic collisions within an atom and can create several secondary electrons capable of continuing the ionization process. This method is a type of impact ionization and is predominant in solid target materials at lower laser intensities and longer pulse durations.

2.2 Single electron dynamics

The entire picture of high-intensity laser-matter interaction is complex and nonlinear because of the relativistic motion of the electrons in the plasma. Due to the high intensities present, the oscillatory velocity of the electrons approaches nearly the speed of light, introducing many relativistic effects such as nonlinear frequency shifting, self-focusing, and relativistic-induced transparency, to name a few. However, one can gain incredibly useful insights by examining the dynamics of a single electron in the laser field.

Once the electron is liberated from its parent atom, it is immediately subjected to the electromagnetic fields of the laser and the plasma. Its equation of motion is then governed by the Lorentz force,

$$\frac{\partial \mathbf{p}}{\partial t} + \mathbf{u} \cdot \nabla \mathbf{p} = -e \left(\mathbf{E} + \mathbf{u} \times \mathbf{B} \right) \tag{2.6}$$

where $\mathbf{E}$ and $\mathbf{B}$ are the electric and magnetic fields, respectively, $\mathbf{u}$ is the electron velocity, $\mathbf{p} \equiv \gamma m_0 \mathbf{u}$ is the relativistic electron momentum, and $\gamma \equiv \sqrt{1 - u^2/c^2}$. By introducing the laser vector potential $\mathbf{A}$ and the plasma electrostatic potential ϕ,

$$\mathbf{B} = \nabla \times \mathbf{A} \tag{2.7}$$

$$\mathbf{E} = -\frac{1}{c} \frac{\partial \mathbf{A}}{\partial t} - \nabla \phi \tag{2.8}$$

Eq. 2.6 can be rewritten as,

$$\frac{\partial \mathbf{p}}{\partial t} + \frac{\mathbf{p} \cdot \nabla \mathbf{p}}{m_0 \sqrt{1 + \frac{p^2}{m_0^2 c^2}}} = e \left(\frac{\partial \mathbf{A}}{\partial t} + \nabla \phi - \frac{\mathbf{p} \times \nabla \times \mathbf{A}}{m_0 \sqrt{1 + \frac{p^2}{m_0^2 c^2}}} \right) \tag{2.9}$$

where m_0 is the electron rest mass. At this point, it is useful to separate the momentum vector in Eq. 2.9 into transverse and longitudinal components which can be thought of as the radiating and non-radiating components of the fields, respectively.

Taking the curl of Eq. 2.9 to obtain the transverse component (for a linearly polarized beam), we obtain,

$$a_0 \equiv \frac{|\mathbf{p}_T|}{m_0 c} = \frac{e|\mathbf{E}_0|}{c\omega m_0} = \sqrt{\frac{I\ [\mathrm{W/cm^2}]\lambda^2\ [\mu\mathrm{m}]}{1.37\times 10^{18}}} \tag{2.10}$$

where a_0 is the normalized oscillatory momentum of the electron in the transverse field, ω is the angular frequency of the laser field, $\mathbf{E}_0$ is the amplitude of the laser electric field, I is the laser intensity and λ is the laser wavelength. The last equality in Eq. 2.10 is obtained via the expression for the average power per unit area transported by an electromagnetic wave, i.e., $I = c\epsilon_0 E_0^2/2$. Inspection shows that when the normalized intensity is greater than 10^{18} Wμm^2/cm^2 (i.e., $a_0 > 1$), the electron motion becomes relativistic. This intensity is easily achieved during high-intensity laser interactions using current technologies and is indeed the criteria for the nonlinear regime of laser propagation through an underdense plasma.

If we take the divergence of Eq. 2.9 to obtain the longitudinal component, we have,

$$\frac{\partial \mathbf{p}_L}{\partial t} = e\nabla\phi - m_0 c^2 \nabla\sqrt{1 + \frac{p^2}{m_0^2 c^2}} \tag{2.11}$$

where $e\nabla\phi$ is the electrostatic force. The second term on the right-hand side of Eq. 2.11 is commonly referred to as the ponderomotive force. This can be recast into a more useful form,

$$\mathbf{F}_P = -\nabla[< \gamma - 1 > m_0 c^2] = \frac{-e^2}{4m_0\omega^2}\nabla|\mathbf{E}|^2 \tag{2.12}$$

where $<>$ denotes an average over the laser period and the last equality is valid in the linear limit. The ponderomotive force arises due to the spatial gradient of a high frequency electric field (such a spatial gradient would exist naturally for a Gaussian focus). Physically, an electron will initially be pushed away from a region of high electric field. Since there is a spatial gradient, the electron ends up in a region of lower field strength and its oscillation causes it to drift away from the focus. Because of the ponderomotive force, the laser pulse expels electrons in a direction away from the strongest electric field and acts like a snowplow as it propagates through the plasma. In addition, this force depends on the particle's mass and charge but not the sign of the charge. Thus, it also affects the ion motion. However, since ions are more massive than electrons, much higher intensities are required to drive ions to relativistic velocities ($I \sim 10^{24}$ W/cm^2).

2.3 Laser-plasma interactions

The progress made in short-pulse laser-plasma interactions owes its rapid advancement to the significant research first conducted in the field of long-pulse laser-plasma interactions. Although long-pulse experiments mainly investigate issues pertaining to inertial confinement fusion (ICF), the results from those experiments provided an understanding of important issues relevant to short-pulse laser-plasma interactions. For laser interactions with underdense plasmas, the primary interaction physics are given in Fig. 2.3 as function of the peak intensity and the normalized laser intensity, $I\lambda^2 \sim a_0$.

The evolution of the laser pulse as it propagates through an underdense plasma is primarily governed by the local plasma density and the pulse parameters such as the pulse duration and shape. For a pulse with a Gaussian radial profile, electrons will acquire a larger quiver momentum at the center of the pulse than at the edges. The transverse oscillating current in the plasma, $J \sim n_e v_0(r,t)$, then has a spatial dependence since the electron quiver velocity, $v_0(r,t)$, depends on the radial profile of the pulse electric field. This spatial dependence of the current gives rise to various nonlinear propagation effects such as self-modulation, filamentation, self-focusing, and frequency shifting.

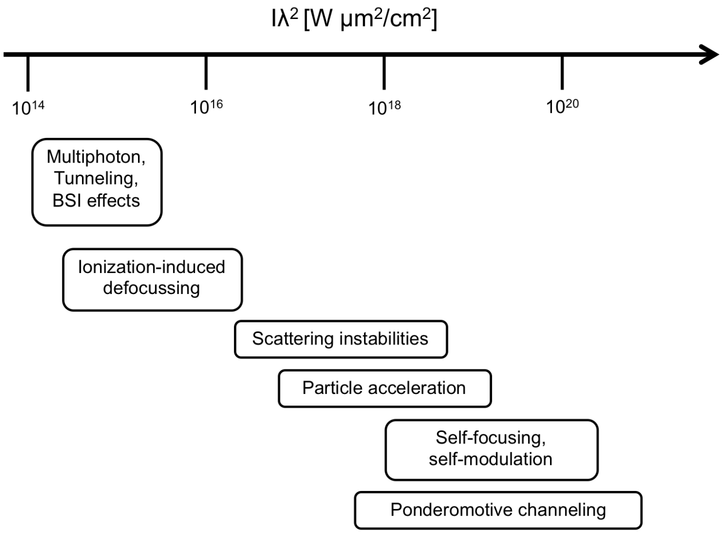

Figure 2.3: Various phenomena in underdense plasmas as a function of the intensity threshold at which they occur. At higher intensities, the majority of the physics depend on the factor $I\lambda^2$, which means that the threshold intensity can depend upon the laser wavelength as well.

This section starts by reviewing linear and nonlinear plasma waves, followed by wavebreaking and wakefield generation, and concluding with some of the nonlinear phenomena and instabilities relevant to this thesis.

2.3.1 Plasma waves in the linear and nonlinear regimes

Plasma wakefields (otherwise known as plasma oscillations) are physically driven by the space charge wave in the plasma and by the ponderomotive force of the laser. In the linear regime ($a_0 \ll 1$), wakefield generation can be described by,

$$(\partial^2/\partial t^2 + \omega_p^2)\delta n/n_0 = c^2\nabla^2 a^2/2 \tag{2.13}$$

$$(\partial^2/\partial t^2 + \omega_p^2)\phi = \omega_p^2 a^2/2 \tag{2.14}$$

where $\delta n/n_0 = (n - n_0)/n_0$ is the normalized density perturbation associated with the electrostatic wake ϕ. For $|\delta n/n_0| << 1$, the density perturbation and wake electric field is,

$$\delta n/n_0 = (c^2/\omega_p) \int_0^t \sin[\omega_p(t-t')\nabla^2 a^2(\mathbf{r},t')/2]\ dt' \tag{2.15}$$

$$\mathbf{E}/E_0 = -c \int_0^t \sin[\omega_p(t-t')\nabla a^2(\mathbf{r},t')/2]\ dt' \tag{2.16}$$

where $E_0 = m_e c\omega_p/e$ is the cold nonrelativistic wave breaking field. For a wave propagating in the x-direction, we change to a coordinate frame that is moving with the group velocity of the laser pulse and make the substitutions $\xi = x - ct, \tau = t$ to obtain

$$\phi(\xi) == \frac{k_p}{4} \int_\xi^\infty |a(\xi')|^2 \sin[k_p(\xi - \xi')]\ d\xi' \tag{2.17}$$

For a "$\sin^2$"-pulse with amplitude given by,

$$\begin{align} a^2(\xi) &= a_0^2 \sin^2\left(\frac{\pi\xi}{\xi_L}\right), 0 \le \xi \le \xi_L \tag{2.18}\\ &= 0, \text{elsewhere} \tag{2.19}\end{align}$$

the longitudinal wakefield behind the laser pulse is then,

$$\begin{align} E_z &= -\frac{\partial\phi}{\partial\xi} \tag{2.20}\\ &= \frac{2\pi^2\Phi_L k_p}{4\pi^2 - k_p^2\xi_L^2}[\sin k_p(\xi-\xi_L) - \sin k_p\xi] \tag{2.21}\\ E_z^{max}(\xi) &= \frac{\pi^2\Phi_L}{\lambda_p}\cos k_p\xi \tag{2.22}\end{align}$$

where $\Phi_L(\xi) = -a(\xi)^2/4$ is the normalized ponderomotive potential of the pulse averaged over the laser period $2\pi/\omega_0$ (assuming a slowly varying envelope approximation) and the last equality is obtained using l'Hôspital's rule. Thus, we see that the longitudinal electric field has a maximum for $k_p\xi_L = 2\pi$, i.e., for pulse lengths $\xi_L = \lambda_p$. In other words, the most efficient wakefield is driven when the pulse length is on the order of the plasma wavelength, $\lambda_p = 2\pi c/\omega_p$. This corresponds to LWFA in the "resonant" regime, which will covered in a later section.

In the case of a Gaussian beam profile $a = a_0 \exp(-r^2/2\sigma^2)$, there are also transverse fields E_r and B_θ. In particular, the radial electric field is given by,

$$E_r^{max}(\xi, r) = -\frac{\partial \phi}{\partial r} \tag{2.23}$$

$$= -\frac{\Phi_L \pi r}{\sigma^2} \sin k_p \xi \tag{2.24}$$

It is interesting to note that the radial and longitudinal fields in a linear wake are exactly 90° out of phase. This general feature of wakefields implies that there is a region of the wake during which an electron will experience simultaneous axial accelerating and radial focusing forces. Thus, in the linear regime, the plasma wave has a simple sinusoidal oscillation with a characteristic plasma frequency, ω_p, and a wave phase velocity, v_p, determined by the group velocity of the driver pulse.

In the nonlinear regime ($a_0 > 1$), the situation becomes more complicated. Analytic solutions in the 1D regime show that the electric field is no longer sinusoidal. Instead it exhibits a characteristic "sawtooth" profile associated with wave steepening and the density oscillations become highly peaked. In addition, as the plasma wave amplitude increases nonlinearly, the plasma wave steepens and its period lengthens due to the increased inertia of the electrons as their velocity becomes relativistic. This lengthening has an important effect in nonlinear 3D plasma waves. For a wave that is driven more strongly on axis than off axis (e.g., using a Gaussian pulse), the wave amplitude is a maximum on axis and, as a consequence, the plasma wavelength is larger on axis. Since the plasma wavelength varies as a function of radius, the wave fronts of the plasma wave becomes curved. As discussed in the next section, this curvature can lead to transverse wavebreaking which can aid in injection of electrons into the plasma wave.

2.3.2 Wavebreaking

In general, one would like the electric field amplitude of the wave to be the maximum possible in order to take advantage of a finite length of plasma in an accelerator. The wavebreaking limit is defined as the maximum amplitude of an electrostatic standing wave allowed within the fluid model. Physically, wavebreaking occurs when one group of electrons in a plasma wave crosses with another group. When this happens, the wave loses its coherence, i.e., it *breaks*. The original theory behind wavebreaking in the cold, nonrelativistic regime was first described by Akhiezer and Polovin [25]. The maximum electric field that can be sustained in this limit is,

$$E_{max} = \frac{m_e \omega_p v_p}{e} \tag{2.25}$$

In the relativistic case, the wavebreaking field is given by [26],

$$E_{WB} = \sqrt{2}(\gamma_p - 1)^{1/2} E_{max} \tag{2.26}$$

and one sees that it is possible for the amplitude of a nonlinear wave to exceed E_{max}. In reality, the electron distribution in the plasma has a finite thermal spread of energies and thermal effects (e.g., pressure) serve to dampen the wave amplitude such that the electron sheets do not cross. The wavebreaking limit is then given by [27],

$$(E_{WB}/E_{max})^2 \simeq 2\gamma_\perp(\gamma_p - 1) - \beta_p^2 \gamma_p \gamma_\perp (8\delta_{th}/3 - 2\delta_{th}^2) \tag{2.27}$$

where $\delta_{th} \equiv (3\beta_{th}^2 \gamma_p^2 / \gamma_\perp^2 \beta_p^2)^{1/4}$.

As mentioned in the previous section, the phase front curvature of the wake can lead to transverse wavebreaking [28]. In this instance, the curvature of the phase front increases with distance from the propagation axis until the radius of curvature is comparable to the electron displacement and wavebreaking occurs. This can aid in the injection of electrons from the sides of the wave due to a local decrease in the wave's phase velocity.

2.3.3 Nonlinear phenomena and instabilities

Short-pulse interactions bring their own variety of nonlinear phenomena and instabilities. These features primarily involve the electron motion due to the short interaction time (∼fs) and long-timescale features such as hydrodynamic instabilities and parametric instabilities involving ions are mostly irrelevant. Examples of short-pulse phenomena and instabilities include stimulated Raman scattering (SRS), relativistic self-focusing, ionization-induced defocusing, and self-phase modulation (SPM). These phenomena arise because the plasma's refractive index (and hence, the wave phase velocity and laser group velocity) depend on the laser amplitude, local electron density, and laser frequency as given by [20],

$$\eta = \left[1 - \frac{1}{2}\frac{\omega_p^2}{\omega_0^2}\left(1 - \frac{< a^2 >}{2} + \frac{\delta n}{n} - 2\frac{\delta\omega_0}{\omega_0}\right)\right] \tag{2.28}$$

The amplitude term, $< a^2 >$, is responsible for relativistic self-focusing and SRS. For a typical Gaussian pulse, relativistic self-focusing occurs due to the index of refraction being peaked on axis, i.e. $d\eta/dr < 0$, and acting as a positive, or focusing, lens. The phase front of the laser pulse travels more slowly at the center than at the edges, giving rise to a curvature in the phase front that causes the rays to bend inward and focus. Relativistic self-focusing has a power threshold given by [29],

$$P_{cr} \simeq 17\left(\frac{\omega_0}{\omega_p}\right)^2 [\mathrm{GW}] \tag{2.29}$$

For a given laser power $P \geq P_{cr}$, the natural diffraction of the laser pulse will be balanced by self-focusing effects. In reality, self-focusing depends on the plasma response as well and it has been shown that self-focusing is only effective for long pulses, $L > \lambda_p$, because the index of refraction is modified on the plasma frequency time scale and not the laser's [30]. However, long pulses can be subject to self-modulation and hosing instabilities. On the other hand, experiments have shown that optical guiding is still possible for short-pulse lasers by using a preformed parabolic plasma density channel, ponderomotive self-channeling, or plasma wave guiding in addition to relativistic self-focusing [31–34]. Stimulated Raman scattering can also occur due to amplitude variations in the laser pulse. In SRS, a large amplitude light wave is scattered into an electron plasma wave and a scattered light wave, i.e., the Stokes $(\omega_0 - \omega_e, \mathbf{k}_0 - \mathbf{k}_e)$ wave. Raman scattering can be used to infer the plasma density by measuring the spectrum of the backscattered radiation and can aid in the trapping of electrons, serving as a basis for an LWFA [35–38]. However, SRS is also detrimental to pulse propagation since the instability effectively takes energy away from the pulse.

The density perturbation term is responsible for ponderomotive self-channeling, self-modulation of long laser pulses, and ionization-induced defocusing. In ponderomotive self-channeling, the radial ponderomotive force of the laser pulse expels electrons from its path and creates a density channel. This can enhance the effects of relativistic self-focusing [33, 39]. The self-modulation of a long laser pulse occurs as a result of the plasma wave producing periodic focusing and defocusing regions. Under the appropriate conditions, a single long pulse can break up into a series of short pulses, each having a width on the order of the plasma wavelength [40, 41]. As discussed in the next section, the self-modulation instability can actually be used to drive relativistic plasma waves in the self-modulated laser wakefield acceleration (SM-LWFA) regime where the instability serves to enhance the wakefield amplitude and acceleration of electrons.

In ionization-induced defocusing, the radial profile of the local electron density acts like a negative, or defocusing, lens. For high gas pressures, the laser beam can be deflected well before reaching its optimal focus and maximum intensity [42]. A simple estimate for the point at which defocusing dominates can be obtained by considering the total deflection of the beam in a underdense plasma [8],

$$\theta_I \sim \frac{1}{\sigma_L} \int \frac{n_e(0)}{n_c} dz \tag{2.30}$$

where σ_L is the laser spot size and $n_c \equiv \epsilon_0 m_e \omega_L^2 / e^2$ is the critical density at which the plasma becomes opaque and reflects the laser pulse. Eq. 2.30 shows that the beam is deflected away from regions of higher density. The diffraction-limited beam divergence satisfies the relation [43],

$$\theta_D = \frac{\sigma_L}{Z_R} \tag{2.31}$$

where θ_D is the beam divergence and $Z_R \equiv 2\pi\sigma_L^2/\lambda$ is the Rayleigh range of the beam. If we consider the deflection and beam divergence over the same propagation distance, then the point at which ionization-induced defocusing dominates is given by,

$$\frac{n_e(I_L)}{n_c} > \frac{\lambda}{\pi Z_R} \tag{2.32}$$

where defocusing also depends on the laser intensity since the intensity governs the ionization rate. In effect, if the ionization process is incomplete once the laser pulse reaches this density value, then the plasma density will remain on this order and cease to increase.

The frequency shift term is responsible for photon acceleration (i.e., frequency shifting of the laser pulse or SPM). In photon acceleration, the frequency of the laser pulse changes due to longitudinal variations in the phase velocity of the plasma wave. The frequency shift is given by [20],

$$\frac{1}{\omega}\frac{\partial\omega}{\partial\tau} = -\frac{\eta^{-2}}{c}\frac{\partial\eta}{\partial\psi} \tag{2.33}$$

where $\psi \equiv t - x/c$ and $\tau = t$ are coordinates in the wave frame. Depending on the local density at the front of the laser pulse, the local phase velocity of the pulse will be different in the front compared to the back of the pulse. This can lead to either frequency upshifting or downshifting, which can be used to enhance either particle trapping or particle acceleration [32, 44, 45].

2.4 Laser-driven plasma-based accelerators

In the late 1970's, Tajima and Dawson realized that laser fields can be used to accelerate electrons in an underdense plasma [38]. This led to a renewed interest in plasma-based accelerators. Prior to plasma-based acceleration schemes, studies investigated the feasibility of acceleration in vacuum and gases [46–48]. It soon became clear that the acceleration of electrons in these media were constrained by certain fundamental limitations. Namely, the acceleration length being limited by pulse diffraction, the electron slippage with respect to the accelerating field of the laser, ionization effects, and the laser wavelength which limits the region of useful interaction [47, 49]. Plasmas offer a way to overcome many of the limitations that exists in vacuum and gases. For example, ionization effects can be overcome by preionizing the plasma, diffraction is balanced by relativistic self-focusing and channeling, and electron acceleration, which occurs over the plasma wavelength instead of the laser wavelength, is due to the axial field of the plasma wave instead of the laser field directly. The phase velocity of the plasma wave is equal to the group velocity of the laser pulse and is less than c and so, electron slippage is not as big an issue either.

The main types of laser-plasma accelerators used today are the LWFA and Plasma Wakefield Acceleration or Accelerator (PWFA) [50, 51]. The primary distinctions between the two types are the driver source, energy loss mechanism, and phase velocity of the wakefield. In LWFA, the laser pulse generates and sustains the plasma wakefields while an external electron beam is responsible for wakefield generation in PWFA. The external electron beam can be first generated in an LWFA and then subsequently used to drive a PWFA and continue to trap and accelerate additional background electrons. In terms of energy loss, the predominant mechanism in LWFA is due to frequency redshift, or photon deceleration, occurring at the leading edge of the pulse. In a PWFA, the electron beam loses energy to the plasma through interaction with the induced electrostatic field [52]. Additionally, in the PWFA regime, the phase velocity of the wake is the velocity of the driving electron beam ($\sim c$) and thus, independent of the plasma density. This has the benefit delaying the electron dephasing until the accelerated bunch catches up to the driving bunch whereas in LWFA, the accelerated bunch dephases when it catches up to the laser pulse whose group velocity depends on the plasma density.

2.4.1 Laser wakefield acceleration

In LWFA, the ponderomotive force of the laser pulse expels all electrons from its path as it propagates through the plasma. In the wake of the pulse, an ion cavity is formed, devoid of electrons. The electrons form a thin sheath around this cavity and undergoes plasma oscillations as the pulse passes. If the pulse length is on the order of the plasma wavelength, the ponderomotive force is then capable of exciting large-amplitude plasma waves behind the laser pulse that can trap and accelerate these electrons to relativistic energies. The exact value of the pulse length that maximizes the wakefield amplitude depends on the shape of the axial pulse profile.

2.4.1.1 Regimes of laser wakefield acceleration

The different operating regimes of LWFA can be distinguished by comparing the pulse length, L_{laser}, to the plasma wavelength, λ_p as described in Table 2.1. The most efficient wakefield is generated in the so-called "bubble" regime using short pulse lasers (i.e., high intensities). In this regime, the ponderomotive force of the laser pulse fully expels all electrons in its path and creates an ion cavity behind it. This cavity has a spherical shape, hence the term "bubble" [53, 54]. Due to the complete cavitation of electrons, the wake has an axial field that is essentially constant as a function of the bubble radius and varies linearly as a function of the distance behind the driver pulse and a focusing radial field that varies linearly as a function of the radius. In the "forced" regime [55], the front of the pulse experiences local pump depletion while the back of the pulse propagates in the density depression of the wakefield cavity. As a result, the back of the pulse propagates faster than the front and creates an optical shock, compressing the pulse. The creation of a sharp leading edge then drives the plasma wave beyond the wavebreaking limit. For longer pulses at low intensities, wakefields can be excited in the self-modulated regime [40, 41]. In this regime, the instability of the laser pulse with the plasma frequency leads to a breakup of the long pulse into a train of shorter pulses each having a length on the order of λ_p. Along with the pulse breakup and the formation of the pulse train, a large amplitude plasma wave is generated and the wakefield is resonantly excited by the train of shorter pulses as opposed to a single pulse as in LWFA.

"Bubble" Regime	"Forced" Regime	Self-modulated Regime
$L_{\text{laser}}/(\lambda_p/2) \leq 1$	$L_{\text{laser}}/\lambda_p \approx 1$	$L_{\text{laser}}/\lambda_p > 1$

Table 2.1: The different regimes of LWFA are defined by the ratio of the laser pulse length to the plasma wavelength. The most efficient wakefield is generated in the so-called "bubble" regime where the pulse length is shorter than half the plasma wavelength and the normalized vector potential $a_0 > 1$. This leads to the maximum possible linear focusing and accelerating fields in the plasma wave.

2.4.2 Electron injection mechanisms

The exact details of electron injection in the nonlinear regime are still up for debate. For example, Ref. [56] suggests that the temporal evolution of the bubble is primarily responsible for self-injection and Refs. [57, 58] provides evidence for a minimum density threshold for injection for a given laser power. What is evident in all these studies is that the majority of electrons are not injected into the cavity behind the laser pulse. Instead they continue their characteristic oscillations without ever extracting significant energy from the plasma wave.

On the other hand, a small population of electrons will have the appropriate initial conditions that enables them to quickly gain sufficient longitudinal momentum within one crossing at the rear sheath of the cavity. During this transit period, the electron velocity must reach nearly the wake phase velocity in order for trapping to occur. Thus, an approximate condition for trapping is that $v_z(r = 0) = v_g$, where v_z is the electron velocity in the longitudinal direction and v_g is the group velocity of the laser. As the background density increases, v_g decreases, allowing injection to occur across a wider set of initial conditions. The threshold can also be reduced for larger plasma wave amplitudes. The amount of charge that can be injected into the wakefield is ultimately limited by either ionization-induced defocusing or the onset of beam loading. Beam loading refers to the process by which the space charge produced by an accelerated bunch of electrons significantly reduces the accelerating fields of the plasma wave [59]. This limits the amount of accelerated charge but can serve to produce a quasimonoenergetic bunch of electrons under the right conditions [60, 61].

Several different injection methods exist. The main ones relevant to this thesis are self-injection (as described above), ionization injection, and density-downramp injection. In ionization injection, electrons are created near the peak of the laser pulse within the wakefield bubble via direct field ionization. These electrons experience additional energy gain due to the accelerating field of the plasma wave within the bubble and are more easily trapped compared with self-injection [62, 63]. In density-downramp injection, the spatially-varying density profile leads to a time-varying plasma wave phase velocity, which allows trapping to occur for electrons with velocity greater than the wave phase velocity [64–68].

2.4.3 Electron acceleration

Once the electrons are injected into the wakefield cavity, they can then be subjected to the longitudinal accelerating and radial focusing forces of the plasma wave. A simplified model of electron acceleration is given by considering an electron accelerated along the z axis by a linear electrostatic plasma wave of the form $E_z = E_{max}\sin[\omega_p(z/v_p - t)]$. The electron will continue to be accelerated until it outruns the accelerating part of the wave and begins to be decelerated. The length over which acceleration occurs is known as the dephasing length, L_{dephase}, and is defined as the distance an electron travels before its slips by one-half of the plasma wave period. For an electron injected into the wake with $v_z < v_p$, it will initially fall backwards with respect to the plasma wave. If the electron manages to gain sufficient longitudinal momentum before reaching the rear of the wakefield cavity, it will undergo acceleration. Otherwise, the electron will continue to slip backward through the plasma wave. The acceleration distance is also subjected to the rate of laser energy depletion occurring at the front of the laser pulse as it propagates through and ionizes the medium. This energy is transferred to generating and sustaining the wakefields [69]. The distance over which the laser pulse will be completed depleted is referred to as the depletion length, $L_{\text{depletion}}$.

2.4.4 Laser wakefield scalings

In designing an initial LWFA experiment, there are several parameters to consider. Typically, the goal is to efficiently produce either high-quality electrons or high-quality X-rays. The two situations are not necessarily linked since high-quality X-rays can be produced from low-quality electron beams. In the context of LWFA, "high-quality" usually refers to electron beams that have a monoenergetic energy spread, high charge ($\sim$ nC), high energy ($\sim$ GeV), and low beam divergence ($\sim$mrad). To this end, there are three important scalings to examine as a first approximation in experimental design. The first two scalings, the dephasing and depletion lengths, were discussed in the previous section. The third scaling involves the Rayleigh length of the focusing optic, $Z_R \equiv \pi w_0^2/\lambda_L$, where w_0 is the spot size of the laser pulse and λ_L is the laser wavelength. It can be shown that $L_{\text{dephase}} \propto \sqrt{a_0} n_e^{-3/2}$ and $L_{\text{depletion}} \propto \tau_L n_e^{-1}$ [70], where τ_L is the laser pulse duration. Since we generally want to operate in the bubble regime, this translates into the requirement that $L_{\text{laser}} \leq \lambda_p/2 \propto n_e^{-1/2}$ and, as the density decreases, the Rayleigh length of the laser increases much more slowly compared to the other two lengths. Thus, in order to generate GeV-energy electron beams in a single-stage LWFA, one must find a way to extend the interaction distance beyond the confocal length of the focusing optic or somehow guide the laser pulse along its propagation through the plasma.

These scalings, along with the average accelerating electric field and the maximum electron energy gain, in the nonlinear, bubble regime are shown in Fig. 2.4 for laser powers in the range $50 - 100$ [TW], electron densities $3 - 10 \times 10^{18}$ cm^{-3}, a 34 fs pulse duration, and a diffraction-limited spot size using an $f/20$ focusing optic for an 800 nm laser wavelength. For a fixed pulse duration, the depletion length depends only on the electron density. The other parameters depend on a combination of the electron density and laser power and hence, are shown as contour plots. From Figs. 2.4 (a) and (b), we see that the dephasing and depletion lengths increases for lower

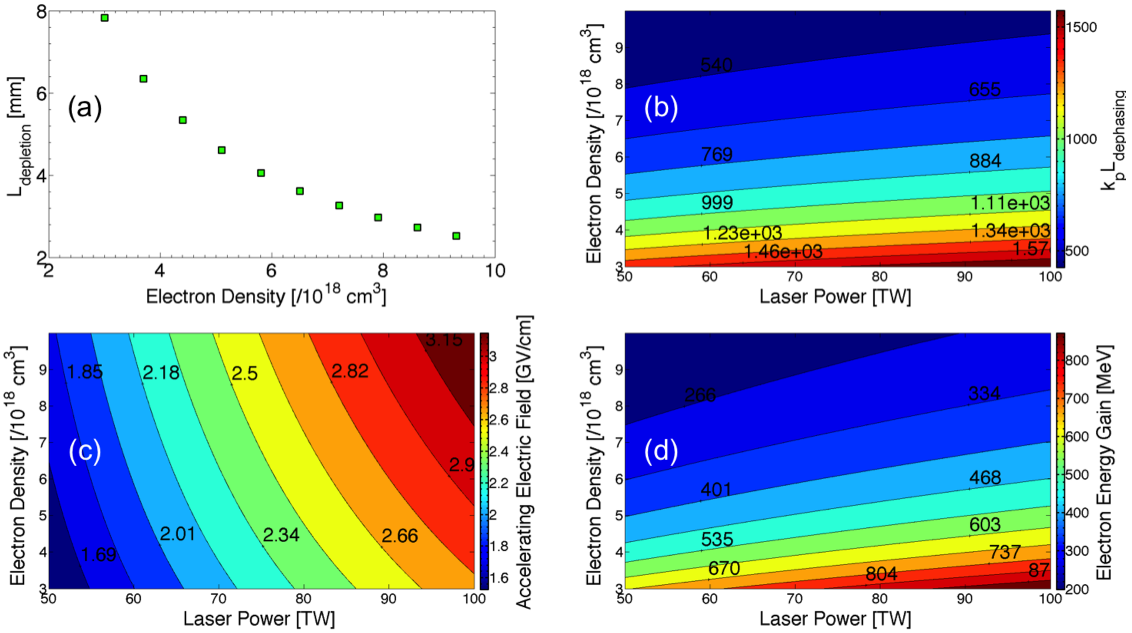

Figure 2.4: Various LWFA scalings in the bubble regime for an 800 nm laser wavelength. (a) Electron dephasing length vs. density. Contour plots of the (b) normalized depletion length, (c) average accelerating electric field of the plasma wave, and (d) maximum electron energy gain as a function of the electron density and laser power. Scalings are taken from Ref. [70].

densities. From Fig. 2.4 (d), the maximum energy gain can be achieved using either lower plasma densities for a given laser power or higher laser powers for a given plasma density. The average accelerating electric field generated in the plasma wave is shown in Fig. 2.4 (c) and is on the order of several GV/cm. In general, the most efficient wakefield in the bubble regime is driven at a density just above the injection threshold and to do so, high laser powers are required.

2.5 Radiation generation from laser-plasma interactions

The main source of radiation emission considered here stems from the acceleration and wiggling of electrons in the wakefield cavity due to the longitudinal and transverse focusing fields, respectively. These oscillations result in the emission of high-energy X-ray radiation whose properties are linked with those of the electrons.

Experimental measurements of the radiation have shown pulse durations on the order of femtoseconds, source size on the order of microns, and peak brightness comparable to third-generation accelerator devices (10^{22} ph/s/mm^2/mrad^2/0.1% bandwidth) [12, 71–76].

The equation for the Liénard-Wiechert field from classical electromagnetism [77] describes how charged particles emit radiation and what governs the characteristic properties of the radiation,

$$\frac{d^2I}{d\omega d\Omega} = \frac{e^2}{16\pi^3\epsilon_0 c} \times \left| \int_{-\infty}^{+\infty} e^{i\omega[t-\vec{n}\cdot\vec{r}(t)/c]} \frac{\vec{n} \times [(\vec{n}-\vec{\beta}) \times \dot{\vec{\beta}}]}{(1-\vec{\beta}\cdot\vec{n})^2} dt \right|^2 \tag{2.34}$$

This equation gives the energy radiated by a charged particle within a spectral band $d\omega$ centered on the the frequency ω and within a solid angle $d\Omega$ centered on the observation direction $\vec{n}$. $\vec{r}(t)$ is the position of the electron at time t, $\vec{\beta}$ is the electron velocity normalized to c, and $\dot{\vec{\beta}}$ is the normalized electron acceleration. The assumption is made that the observer is far away enough from the electron so that $\vec{n}$ is constant along the electron trajectory. Equation 2.34 offers many important insights into the radiation emission from an accelerated particle. First, when $\dot{\vec{\beta}} = 0$, no radiation is emitted—this is a classical result from electromagnetism which states that acceleration is responsible for radiation emission from charged particles. Second, the term in the denominator inside the integral shows that emission is maximized when $\vec{\beta}\cdot\vec{n} \approx 1$. This condition is met when $\vec{\beta} \simeq 1$ and $\vec{\beta} \,||\, \vec{n}$. In physical terms, a relativistic electron will radiate much more compared with a nonrelativistic electron and its radiation will be directed primarily in the direction of its velocity vector. Third, the term in the numerator inside the integral, along with the relations $\dot{\vec{\beta}}_{||} \propto \vec{F}_{||}/\gamma^3$ and $\dot{\vec{\beta}}_{\perp} \propto \vec{F}_{\perp}/\gamma$, indicates that a transverse force is more efficient at producing radiation than a longitudinal force. Lastly, the phase term in the integral can be locally approximated as $e^{i\omega(1-\beta)t}$. The integration will only be nonzero when the integrand (excluding the exponential) varies at approximately the same frequency as the phase term which oscillates at $\omega_\phi = \omega(1-\beta) \sim \omega_{e^-}$, where ω_{e^-} is the oscillating frequency of the electron. As a result of the Doppler upshift, the electron will actually oscillate at the higher frequency $\omega = \omega_{e^-}/(1-\beta) \simeq 2\gamma^2\omega_{e^-}$. In summary, Eq. 2.34 shows that X-ray radiation, whose frequency is on the order $\omega_X \sim 10^{18}s^{-1}$, can be produced by wiggling a relativistic, directional electron beam at the much lower frequency, $\omega_{e^-} \sim \omega_X/(2\gamma^2)$.

In general, there are two regimes of radiation that are distinguished by the dimensionless strength parameter, $K \equiv \gamma\psi$, which represents the maximal angle of the electron trajectory with respect to its propagation axis, ψ, and the opening angle of the radiation cone, $\Delta\theta \sim 1/\gamma$. As shown in Fig. 2.5 (b), $K \ll 1$ corresponds to the "undulator" regime where the electron radiates in essentially the same direction at all times as it propagates. When $K \gg 1$, the radiation emission is spatially decoupled and corresponds to the "wiggler" regime. The spectrum, divergence, radiated energy, and number of emitted photons produced are different depending on the operating regime.

The fundamental radiation wavelength is given by [19],

$$\lambda \simeq \frac{\lambda_u}{2\gamma^2}\left(1 + \frac{K^2}{2} + \gamma^2\theta^2\right) \tag{2.35}$$

with a corresponding fundamental frequency of $\omega = 2\pi c/\lambda$ and its harmonics. In the undulator regime, the radiation spectrum consists of a single peak at the fundamental frequency ω which depends on the angle of observation. In the wiggler regime, the spectrum consists of a series of harmonics up to the critical frequency, $\omega_c = (3/2)\gamma^3(c\rho)$ [77]. One can view the parameter K as the number of decoupled sections of the trajectory for which the radiation is emitted towards an observer. In the wiggler regime, there are a large number of such sections and the radiation is emitted in bursts in each direction. This leads to the observation of a broad

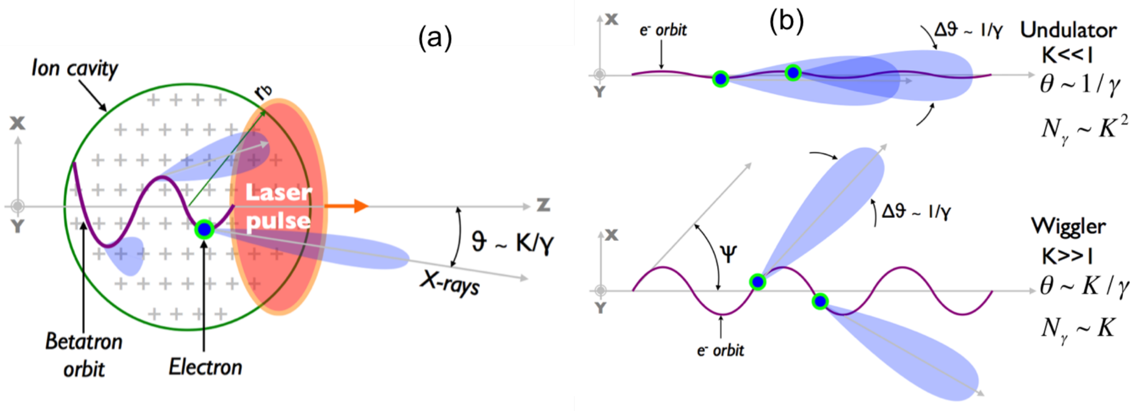

Figure 2.5: (a) In LWFA, the electron is generally injected into the wakefield with a nonzero offset and subsequently subjected to focusing fields. Due to the acceleration and oscillation of the electron, radiation is perferentially emitted in the forward direction and confined to a narrow cone. (b) Schematic of the undulator and wiggler regimes of radiation emission. Radiation emission in the undulator regime occurs in the same direction along the electron's trajectory. In the wiggler regime, radiation is emitted in different directions at each portion of the trajectory. Figures used with permission from Ref. [19].

spectrum of harmonics of the fundamental frequency up to ω_c. In addition, since the wavelength depends on the angle θ, the integration of the radiation broadens each harmonic, leading to a continuous spectrum due to overlapping harmonics.

In a laser-plasma accelerator, radiation emission in the wiggler regime is referred to as "betatron" radiation. The radial field inside the ion cavity drives the transverse oscillations of the electrons at the characteristic betatron frequency, $\omega_\beta \simeq \omega_p/\sqrt{2\gamma}$ [19]. The electron trajectory, betatron amplitude, and betatron frequency are also time-dependent [78, 79]. In practical units, the critical energy (with mean photon energy $< \hbar\omega >= 0.3\hbar\omega_c$) and the number of photons emitted per oscillation per electron are given by,

$$\hbar\omega_c\ [\mathrm{eV}] = 5.24 \times 10^{-21}\gamma^2 n_e\ [\mathrm{cm}^{-3}] r_\beta\ [\mu\mathrm{m}] \tag{2.36}$$

$$N_\gamma = 3.31 \times 10^{-2} K \tag{2.37}$$

where r_β is the amplitude of the betatron oscillation inside the wakefield cavity.

For an electron bunch that is being accelerated, the main contribution to the radiation energy comes from the part of the trajectory where its energy is maximal and occurs around the dephasing length. This is evident upon inspection of Eqs. 2.36 and 2.37. The number of photons emitted in one period has a weak dependence on γ through $K \propto \gamma^{1/4}$ but the radiated energy is proportional to γ^2. For the HERCULES laser system, typical parameters are: $K = 6$, $n_e = 5 \times 10^{18}$ cm^{-3}, and $\gamma = 600$ for a $\simeq 300$ MeV electron beam. This gives a critical energy of $\hbar\omega_c = 9.4$ keV.

The radiation emission can be complicated if: 1) the ion cavity is not completely devoid of electrons, 2) the pulse duration is on the order of the plasma wavelength, and 3) electrons inside the cavity interact with the laser pulse. In reality, the first condition is automatically true due to trapping of electrons. In addition, electrons can interact resonantly with the laser pulse to increase their oscillation amplitude and therefore, the radiation emission, and longer pulse lengths allows this interaction to occur more easily.

2.6 Basics of ultrashort pulses

When an ultra-short pulse propagates through a dielectric medium, both its temporal duration and shape can change due to phase modulations of the carrier wave. A brief discussion on ultra-short pulse propagation, dispersion, and related phenomena is presented here to serve as a background for some of the experimental results presented in this thesis.

A 1D plane wave propagating in free space in the z-direction can be described by the equation,

$$\frac{\partial^2 E(z,t)}{\partial z^2} - \frac{n^2}{c^2}\frac{\partial^2 E(z,t)}{\partial t^2} = 0 \tag{2.38}$$

where n is the index of refraction of the medium. Most high-intensity laser pulses can be approximated as Gaussian pulses and so the pulse can be represented by $E(t) = \varepsilon(t)e^{i\omega_0 t}$, where ω_0 is the carrier frequency and $\varepsilon(t)$ is the complex envelope function. In a linear system, each frequency component of the pulse propagates through the system independently and its propagation can be described by a linear transfer function, $E_{\text{out}}(\omega) = H(\omega)E_{\text{in}}(\omega)$.

To examine the phase modulation of the carrier wave, we can describe the transfer function as $H(\omega) = e^{i\phi(\omega)}$, where $\phi(\omega) = \phi_0 + \phi'(\omega_0)(\omega - \omega_0) + \phi''(\omega_0)(\omega - \omega_0)^2/2 + ...$ in a Taylor expansion around the carrier frequency. The overall phase ϕ_0 is inconsequential in most cases involving multi-cycle pulses. The ϕ' term imparts a linear spectral phase shift on the pulse and gives rise to the group velocity dispersion of the pulse envelope. The quadratic spectral phase term in the expansion results in a linear frequency chirp, i.e., the instantaneous frequency changes linearly in time. Since the index of refraction decreases with wavelength for most common materials in the visible region of the spectrum, an optical pulse propagating through a dielectric medium will experience a positive frequency chirp where lower frequencies lead in time. It is also possible for a pulse to acquire a negative chirp where higher frequencies lead in time. In both cases, a quadratic spectral phase also expands the pulse duration symmetrically as it propagates due to group velocity dispersion (GVD) of the pulse. The amount of pulse broadening is given by,

$$\tau_p = \tau_{p0}\sqrt{1 + 4\phi''^2/\tau_{p0}^2} \tag{2.39}$$

for an input pulse duration τ_{p0}. The time-bandwidth product gives the pulse duration for a given frequency bandwidth. For Gaussian pulses, the time-bandwidth is approximately,

$$\tau_p \cdot \Delta f_p \approx 0.44\sqrt{1 + 4\phi''^2/\tau_{p0}^2} \tag{2.40}$$

Thus, the minimum pulse duration can only be achieved for a transformed-limited pulse, i.e. $\phi'' = 0$. Higher-order terms in the Taylor expansion produce increasing orders of chirp (e.g., quadratic chirp, cubic chirp, etc.). In general, even phase terms result in symmetric distortions of the pulse while odd phase terms result in asymmetric distortions, with pulse broadening occurring regardless of the phase order.

In order to produce and maintain ultra-short pulses, a method of imparting negative GVD without optical absorption is required. For high-intensity laser systems, negative GVD is typically achieved by sending the pulse through a pair of diffraction gratings in a double-pass configuration [80]. The positive GVD (and pulse broadening) due to propagation in a normally dispersive media can then be compensated accordingly. It can also be shown that third-order dispersion, ϕ''', is always positive for a grating pair. Thus, grating pairs can be used to negate positive frequency chirps but the output pulse will not approach the transform limit due to the non-zero cubic phase error.

In general, it is useful to design a grating system that allows for tunable control of the frequency chirp. This can be accomplished in a Martinez configuration [81, 82]. The HERCULES laser system employs two pairs of gold-coated holographic gratings that is capable of in-situ, continuous adjustment of the frequency chirp of the final amplified pulse. This setup provides an ideal environment for studying the effects of pulse duration, shape, and frequency chirp on the electron injection and acceleration processes as well as the subsequent radiation emission.

Since ultra-short pulses often have very high peak powers, pulse propagation occurs in a nonlinear system. The nonlinearity, known as the optical Kerr effect, arises from distortions of the charge distributions in a material in response to the incident electric field of the pulse. The index of refraction for a medium may be written as,

$$n = n_0 + n_2 I \tag{2.41}$$

where n_2 is the nonlinear index. The nonlinear index is responsible for both SPM and self-focusing, which were explained in section 2.3.3. A third effect is self-steepening of the laser pulse, which occurs even in the absence of GVD, if the pulse is sufficiently intense. The group velocity then becomes intensity-dependent and higher intensities lead to lower group velocities. Thus, as a pulse propagates, the peak of the pulse travels slower than its wings and the trailing edge of the pulse steepens as a result. All three effects (SPM, self-focusing, and self-steepening) can also interact with another and result in either pulse compression, pulse stretching, or an asymmetric frequency spectrum depending on the dominant effect.

CHAPTER III

Methods

3.1 Introduction

All experiments performed in this thesis were conducted using the HERCULES laser system at the Center for Ultrafast Optical Science (CUOS) at the University of Michigan [83]. This chapter describes the laser system, targets, and diagnostics for the experiments. In addition, PIC simulations were conducted to gain a deeper understanding into the results from some of the experiments and an overview of the PIC method is given.

3.2 HERCULES laser system

The HERCULES laser system was a Titanium-doped Sapphire (Ti:Sapphire) based, CPA system that operated at a peak power of 300 TW and a peak repetition rate of 0.1 Hz [84]. A schematic of the HERCULES laser is shown in Fig. 3.1. The gain media lases at a central wavelength of 800 nm while the pump lasers operate at 532 nm. The overall system can be divided in multiple stages, with each stage acting as a separate amplification node pumped by frequency doubled neodymium doped lasers. Starting with the front end section, the seed pulse is generated using a Kerr-lens mode-locked oscillator lasing at 800 nm that outputs a train of ∼nJ, 12 fs pulses at 75 MHz. These pulses are then sent to a Dazzler pulse shaper and a pulse picker consisting of a Pockels cell and a set of polarizers, which reduces the pulse rate to 10 Hz. Afterwards, the pulses are amplified to $\sim \mu$J energy in a 2-pass pre-amplifier stage.

For further amplification, the pulses are then stretched using a folded Martinez pulse stretcher to 500 ps before being injected into the regenerative amplifier. Here, the chirped pulses are amplified to 30 mJ before being ejected. For the experiments conducted for this thesis, the nanosecond contrast (given as the ratio of the laser intensity nanoseconds prior to the arrival of the main pulse to the main pulse itself) is approximately 10^{-8} [85]. Each subsequent stage then amplifies the pulses accordingly from ~ 1 to ~ 3 to ~ 17 J at the end of the final amplification stage. These amplifiers corresponds to the "10 TW", "30 TW", and "100+" TW power modes of HERCULES, respectively. Each stage is protected from back reflections by a combination of spatial filters, Faraday isolators, and Pockels cells. The amplified chirped pulses are then expanded from 50 to 150 mm diameter before being recompressed in a Treacy compressor which consists of two pairs of gold-coated holographic gratings (420×210 mm^2 and 220×165 mm^2, 1200 lines/mm) from Jobin Yvon. The final output of the compressor produces a horizontally-polarized pulse with a maximum energy of 9 J and a minimum pulse duration of 30 fs, providing a peak power of 300 TW. In practice, the peak power is ~ 150 TW due to isolation systems that are implemented throughout the laser chain in order to prevent backscattered radiation from damaging the system optics.

The longer pulse duration at the end of the amplification chain is due to gain narrowing and higher-order dispersion. Although the system was initially designed to compensate up to fifth-order dispersion, many changes have been made to the system since its inception. Gain narrowing (i.e., reduction of the available pulse bandwidth) in the amplification stages occurs due to inefficient pump power extraction at the low-

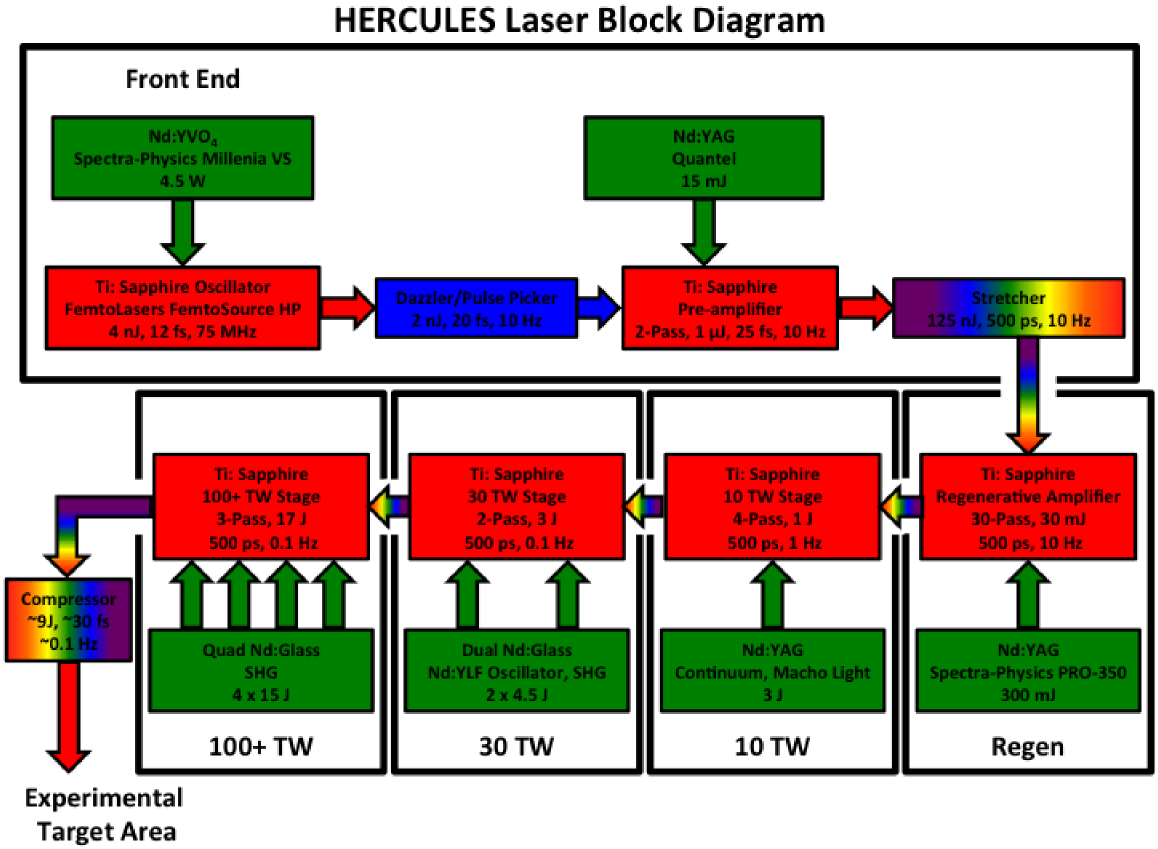

Figure 3.1: Schematic of HERCULES laser system. Amplification stages for 800 nm are represented by red blocks and pump lasers for 532 nm are represented by green blocks. For each block, the output parameters of the pulse is given as well as the colloquial name for the stage.

intensity leading and trailing edges of the pulse. Pump depletion causes the longer wavelengths of the chirped pulse to receive maximum amplification and leads to red-shifting of the central frequency component and a reduction in the overall bandwidth. In addition, HERCULES produces pulses with a Gaussian frequency profile. Thus, the highest power portion of the chirped pulse is around the central wavelength (800 nm) and this portion is selectively amplified. The post-compressor bandwidth is typically $\sim$ 30 nm. After compression, the beam is downsized to 100 mm diameter before arriving at the experimental chamber.

3.3 Laser diagnostics

Due to the sensitivity of LWFA experiments to the laser power, contrast, and pointing, the focal spot profile, and the pulse duration and shape, several laser diagnostics are employed to measure these parameters. With the exception of the laser power, contrast, and pointing measurements, the other parameters are typically characterized using the 10 Hz, lower-energy regenerative amplifier pulses instead of a single-shot at full power due to either complexity in the diagnostic setups or damage to the diagnostics at full power. This section describes the primary methods used to characterize and optimize the various laser parameters as well as the general procedure for target chamber alignment.

3.3.1 Laser power

The overall process of LWFA is highly sensitive to the peak laser power. The available power determines the injection threshold for accelerating electrons in the wakefield as well as their maximum energy gain and the energy of the emitted radiation. In general, higher powers relax the operating constraints for wakefield experiments. The laser power for a given shot can be calculated by simultaneously measuring the laser spectral bandwidth (which provides the minimum pulse duration possible due to the time-bandwidth constraint) and energy. The bandwidth of a full power shot is measured using a Thorlabs CCS175 fiber spectrometer by taking a leak-through from a dielectric mirror before the compressor chamber. The laser pulse energy can be measured at each amplification stage by summing the near-field image of the beam through a leak-through mirror right before the compressor chamber by focusing the leak-through light onto a Thorlabs DET10 photodiode that is read out by an oscilloscope. The images from each amplifier stage are useful in detecting damage in the amplifier optics (observed in the form of a growing diffraction pattern in the beam profile) and can be used to isolate which amplifier is responsible for a reduction in laser power. However, these images can be subject to significant shot-noise and thus, can be inconsistent from shot-to-shot. The photodiode measurement provides an extremely linear and consistent measurement of the laser power on a shot-to-shot basis. Both methods are cross-calibrated with an integrating sphere prior to the start of an experiment.

3.3.2 Laser contrast

In any realistic high-intensity laser system, the amplified pulse contains several temporal features other than the peak of the pulse. These features generally represent either amplified spontaneous emission (ASE), short-pulse pre-pulses, or post-pulses. Amplified spontaneous emission and short-pulse pre-pulses can significantly alter the laser-matter interaction process. For laser-solid interactions, they can change the plasma density scalelength, which in turn affects the laser energy absorption and electron and ion energy spectra [86]. For laser-gas interactions, they can affect the ionization level and the gas target density profile prior to the arrival of the main pulse and cause premature plasma formation during pump-probe type experiments.

Over ∼ns timescales prior to the arrival of the peak of the pulse, residual ASE can form from light leaked through the Pockels cells in the amplifier stages. The ASE contrast ratio, defined as the intensity of the pulse peak to the ASE pedestal, was measured on HERCULES to be 10^8 without any pulse cleaning techniques such as the cross-polarized wave (XPW) technique [85]. For this thesis, typical peak intensities were on the order of 10^{19} W/cm^2 and the ASE level is low enough not to cause significant changes in the gas target profile prior to the arrival of the main pulse [see Fig. 2.2]. Pre-pulses occur on the ∼ps timescale and are primarily a result of imperfect pulse compression and short-pulse pre-pulses. Imperfect compression arises from the inability of the compressor gratings to correct for phase terms higher than fourth order. Short-pulse pre-pulses mainly arise from improper alignment or un-

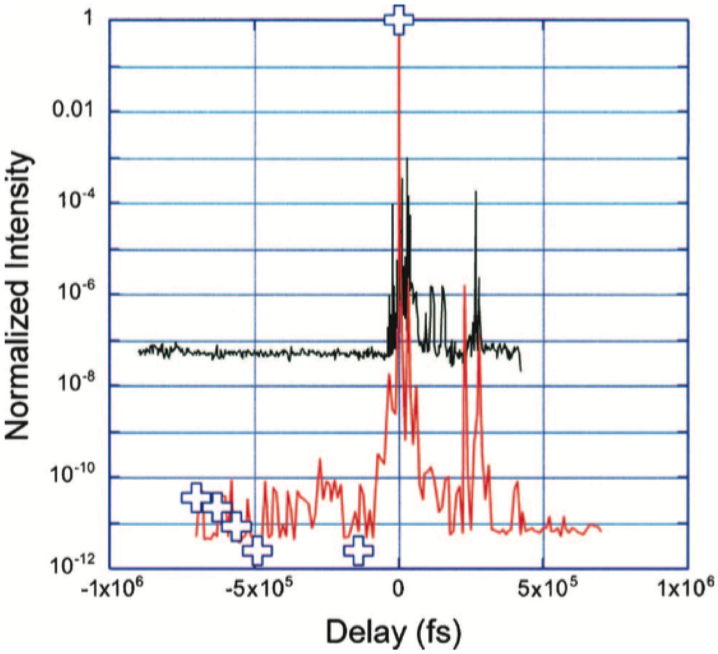

Figure 3.2: Measurements of the pulse profile using a third-order autocorrelator with XPW (red) and without (black). Figure used with permission from Ref. [85].

coated/unwedged optics in the laser system. Double back-reflections from these optics can also result in post-pulses which can overlap with the main pulse (when chirped) and shift energy spectrally to form a pre-pulse after amplification and compression [87]. Figure 3.2 shows the measured laser contrast for the HERCULES system with and without XPW using a third-order autocorrelator. The use of autocorrelation to measure the pulse duration for this thesis is discussed in Section 3.3.5.

3.3.3 Laser pointing

Proper alignment of the laser beam into the chamber is critical to ensure that the focused pulse is incident on the gas target in the proper orientation. Beam alignment can affect the electron beam pointing and profile as well. Laser pointing can be influenced by a variety of factors. For example, mechanical vibrations from optical tables, air turbulence from air-conditioning units in the laser room, and slight drifts in the upstream laser alignment over several hours can affect the beam pointing. In addition, temperature and humidity can also adversely affect the stability of the laser system. The alignment of the laser beam into the target chamber begins with a set of periscope mirrors after the compressor chamber. These mirrors are remotely controlled to steer the beam to be parallel to the alignment axis of the chamber and serves as the first alignment point in the system. To characterize the beam pointing into the experimental chamber, a far-field pointing diagnostic is used that consists of a 10X microscope objective and a focusing lens with an f-number of ~ 20. This diagnostic, referred to as the POINTING diagnostic, is installed after the leak-through of the first dielectric mirror in the chamber. The POINTING diagnostic ensures that the beam enters the chamber parallel to the surface of the optical table and also serves to track the shot-to-shot fluctuations in the pointing and shape of the focused beam during full power shots.

3.3.4 Focal spot

The second point of alignment in the chamber is the focal spot monitor diagnostic which allows the beam focus intensity profile to be characterized before a full power shot. For the $f/20$ paraboloid used in the gas target chamber, a 10X microscope objective is used to image the laser focus onto an 8-bit Watec charge coupled device (CCD) camera. The focal spot diagnostic is also mounted onto a translation stage in the direction of pulse propagation in order to measure the focus intensity profile across the confocal length of the paraboloid. A typical image of the focal spot and its intensity lineout is shown in Fig. 3.3. At best focus, the spot measures approximately $26 \times 48\ \mu\text{m}$ at full width at half maximum (FWHM) in intensity. There is increased energy in the wings of the pulse in the vertical direction due to a combination of astigmatism and coma. Corrections can be performed upstream in the laser system by rotating a lens placed in free space. However, it is typically not possible to completely eliminate the wings without the use of adaptive optics such as a deformable mirror.

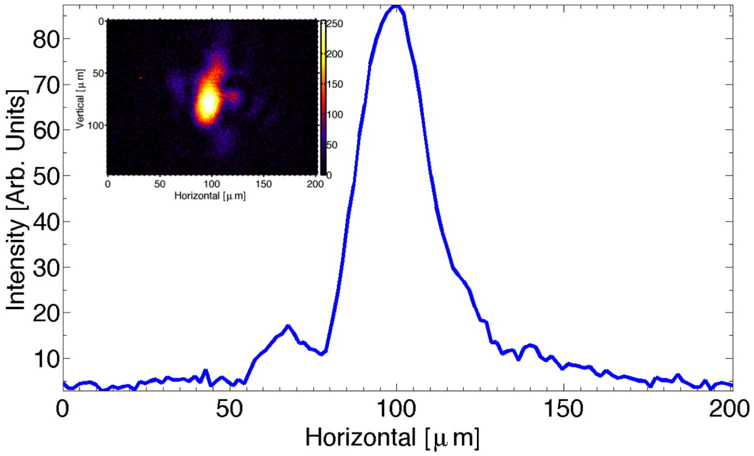

Figure 3.3: Intensity profile lineout of the focal spot from an $f/20$ paraboloid with a 26 μm intensity FWHM in the horizontal direction. Inset shows a false color image of the focal spot and its surrounding structure. Note the increased energy in the wings along the vertical direction due to a combination of astigmatism and coma.

For LWFA, the energy within the FWHM of the beam is critical in driving the wakefield and accelerating electrons; energy in the wings of the pulse is essentially wasted and does not contribute to the wakefield generation process [44].

3.3.5 Pulse duration and pulse shape

Short pulses are also critical in wakefield experiments in order to ensure that the wakefield is being driven in the bubble regime. Measuring the pulse duration of ultrashort pulses have historically been a challenging task since one needs to use an event that is shorter than the pulse itself. This rules out most forms of electronic measurements such as a photo-diodes and photo-multipliers since the response time of these devices is usually on the order of nanoseconds at best. Thus, the pulse duration for HERCULES was measured using either second-order autocorrelation [88] or the technique of frequency resolved optical gating (FROG) based on second harmonic generation (SHG) or SHG-FROG [89]. Pulse shape (i.e., pulse intensity and phase) measurements were conducted using a SHG-FROG device (SwampOptics).

The second-order autocorrelator (or intensity autocorrelator) relies on the χ^2 nonlinearity present in crystals to measure the pulse energy vs. delay. The setup uses a beamsplitter to send a copy of the pulse into a path that contains a delay stage used for the scan. Varying the delay overlaps the two replicas of the pulse and the autocorrelation measurement is only nonzero when the pulses overlap. The second harmonic light generated in the crystal from the overlap can then be imaged using a CCD camera. A lineout of the signal on the camera provides the pulse duration after a temporal-spatial calibration. This calibration can be done by simply inserting a glass slide of known refractive index and thickness into one arm of the autocorrelator. The glass causes a known temporal delay and measurement of the signal shift on the camera relates the delay to the spatial dimension. Second-order autocorrelation is relatively simple to setup; however, the technique provides a trace that is symmetric in time and hence, information on the direction of time of a pulse and its phase is lost. Nevertheless, for pulses that are known to be approximately Gaussian shaped, second-order autocorrelation can provide a reasonable estimate for the pulse duration. A schematic of an intensity autocorrelator in shown in Fig. 3.4 (a).

For a complete characterization that includes the time-dependent intensity and phase profiles of the pulse, SHG-FROG is used. At its core, SHG-FROG is simply a spectrally resolved intensity autocorrelation. As shown in Fig. 3.4 (b), the technique involves gating the pulse with a variably delayed version of itself using a nonlinear optical medium in the time domain and then spectrally resolving the gated pulse versus the delay in the frequency domain. That is, the technique temporally resolves the slow components of the pulse and spectrally resolves the fast components. It is also distinct from an intensity autocorrelation in that SHG-FROG does not require an assumed pulse shape in order to retrieve the pulse duration. The resulting spectrogram signal can be analyzed using an iterative, two-dimensional phase-retrieval program that can calculate the pulse intensity and phase profiles. The SHG-FROG trace still has an ambiguity with respect to the direction of time. However, this ambiguity can

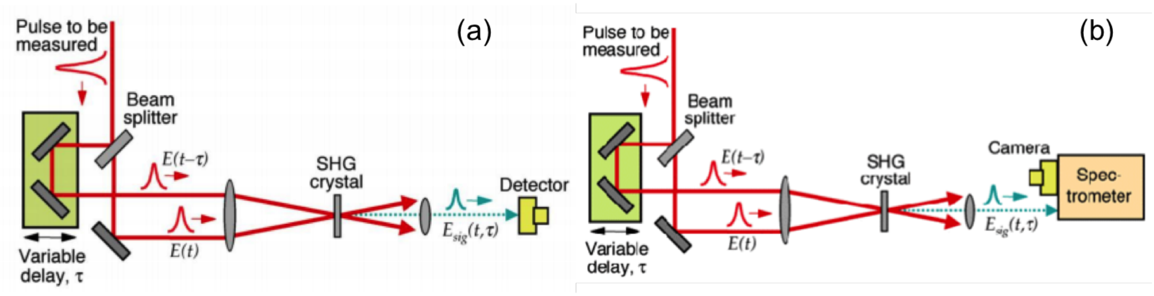

Figure 3.4: (a) Schematic of a second-order autocorrelator setup, relying on the principal of SHG in a crystal. The generated signal is then imaged on a CCD device where a spatial-temporal calibration provides the pulse duration. (b) Schematic of a SHG-FROG setup. The complete pulse intensity and phase profiles can be obtained by using a combination of a nonlinear crystal and a spectrometer. Figures from Ref. [90].

be determined by either introducing a glass slide to induce a known frequency chirp or knowing *a priori* the direction of time as a function of the compressor grating separation. For the HERCULES laser system, decreasing the separation between the compressor grating pairs corresponds to imparting a positive frequency chirp on the pulse and increasing the grating separation corresponds to imparting a negative frequency chirp.

The pulse profile can be readily adjusted in-situ for the HERCULES system by changing the relative separation of the compressor grating pairs. A trace from the second-order autocorrelator and a plot of the average pulse duration as a function of the relative compressor grating separation are shown in Fig. 3.5. The corresponding images from the SHG-FROG technique are shown in Fig. 3.6. The directions corresponding to positive and negative frequency chirps are shown as well. Both techniques produce a pulse duration curve that is generally parabolic in shape with a flat bottom region on both sides of optimal compression (denoted by the "0" label on the horizontal axis). The slightly higher pulse duration from the intensity autocorrelation is due to a $\sqrt{2}$ factor to account for the assumed Gaussian-shaped pulse. It is worth noting that the non-symmetric shape of the pulse duration profile indicates the existence of higher-order dispersion, most likely fifth order. Measurements of the

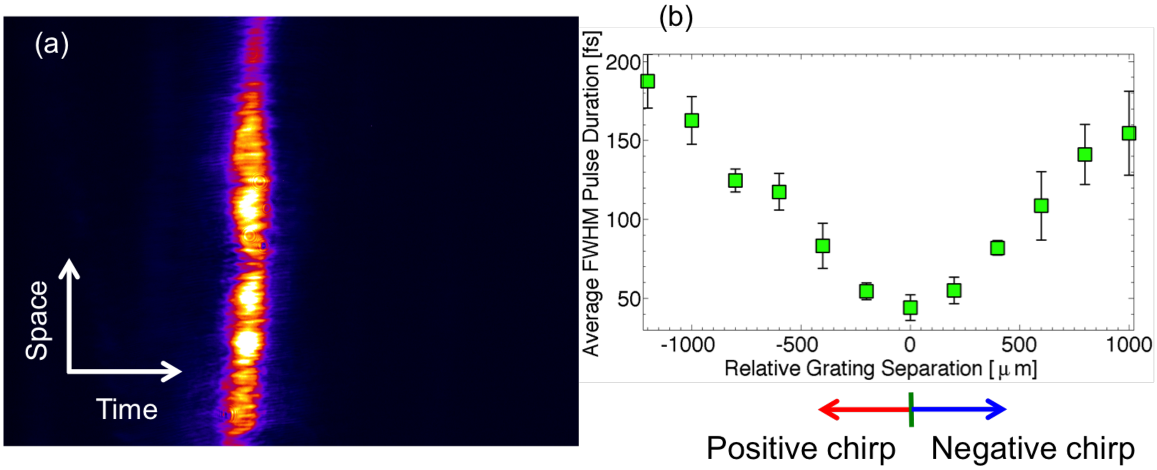

Figure 3.5: (a) False color image of the signal from SHG generation in a nonlinear crystal. Integrating the signal in the spatial direction provides a lineout of the pulse intensity profile (assuming a Gaussian-shaped pulse). (b) Average FWHM pulse duration as a function of the relative compressor separation from a second-order autocorrelation conducted in vacuum showing a minimum pulse duration of 44 fs. Frequency chirp directions are denoted by arrows.

pulse shape are discussed in detail in Chapter IV.

3.4 Gas cells

Laser wakefield experiments have historically been conducted using either gas jets or capillaries as the target of choice [91, 92]. Gas jets typically use a conical nozzle to optimize the supersonic expansion of the gas into the vacuum. They offer a simple and relatively reliable method of delivering a uniform background density profile and thus, were used as the first gas targets for LWFA experiments on HERCULES. Gas-filled capillaries serve as a plasma waveguide and can be used to accelerate electrons to GeV energies over long distances at relatively low power. Both targets have their particular disadvantages however. For example, injection and acceleration of electrons are typically more unstable using gas jets and care must be taken to ensure that the plastic capillary is not destroyed before the arrival of the main pulse.

As LWFA experiments progressed on HERCULES, 3D printed gas cells were even-

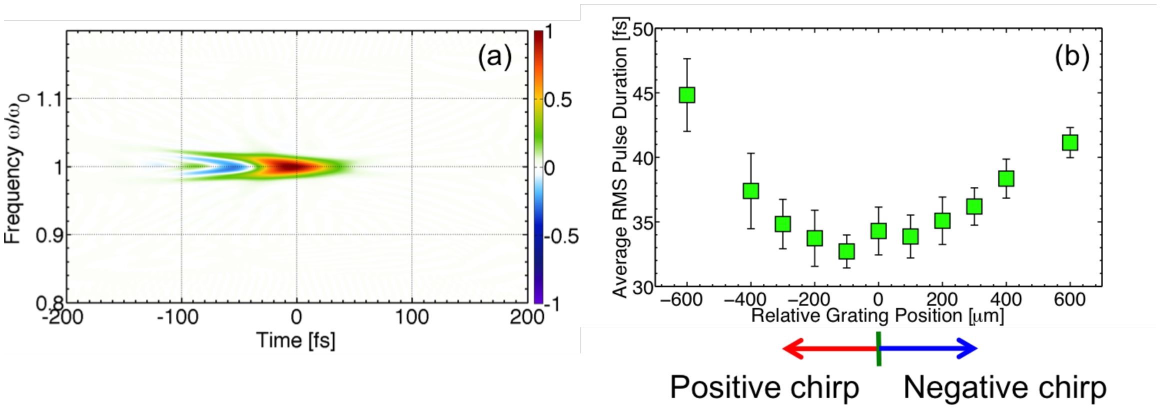

Figure 3.6: (a) Wigner distribution (frequency vs. time) obtained from SHG-FROG device. (b) Average RMS pulse duration as a function of the relative compressor separation from SHG-FROG conducted in air showing a minimum pulse duration of $\sim$ 34 fs. Arrows denote the frequency chirp directions.

tually used as the de facto target type. Gas cells help to create a uniform plasma volume in a stable environment and enable direct control of the plasma density by simply adjusting the backing pressure of the gas lines. In fact, the measured density is linearly proportional to backing pressure and is repeatable as shown in Fig. 3.7 (c). Because these cells are printed in-house, different varieties can be rapidly prototyped and used in experiments at low cost. Figures 3.7 (a) and (b) show images of two different gas cells. The two-stage variant is used to separate the injection and acceleration process of LWFA and allows different gases to be used for each stage. In effect, the first stage produces a high-charge quasimonoenergetic electron beam and the majority of the energy gain is achieved in the second stage.

It has been experimentally demonstrated on HERCULES that the use of these two-stage cells can lead to an overall improvement in the electron beam properties compared with the use of gas jets [93]. The top row of Fig. 3.8 shows several images of the electron beam energy spectrum generated using different gas targets and laser powers, ranging from a 10 mm gas jet at 100 TW to a two-stage gas cell at 110 TW. The supersonic gas jet nozzles produced average quality electron beams in terms of charge, energy spread, and divergence. With the use of gas cells, the charge and

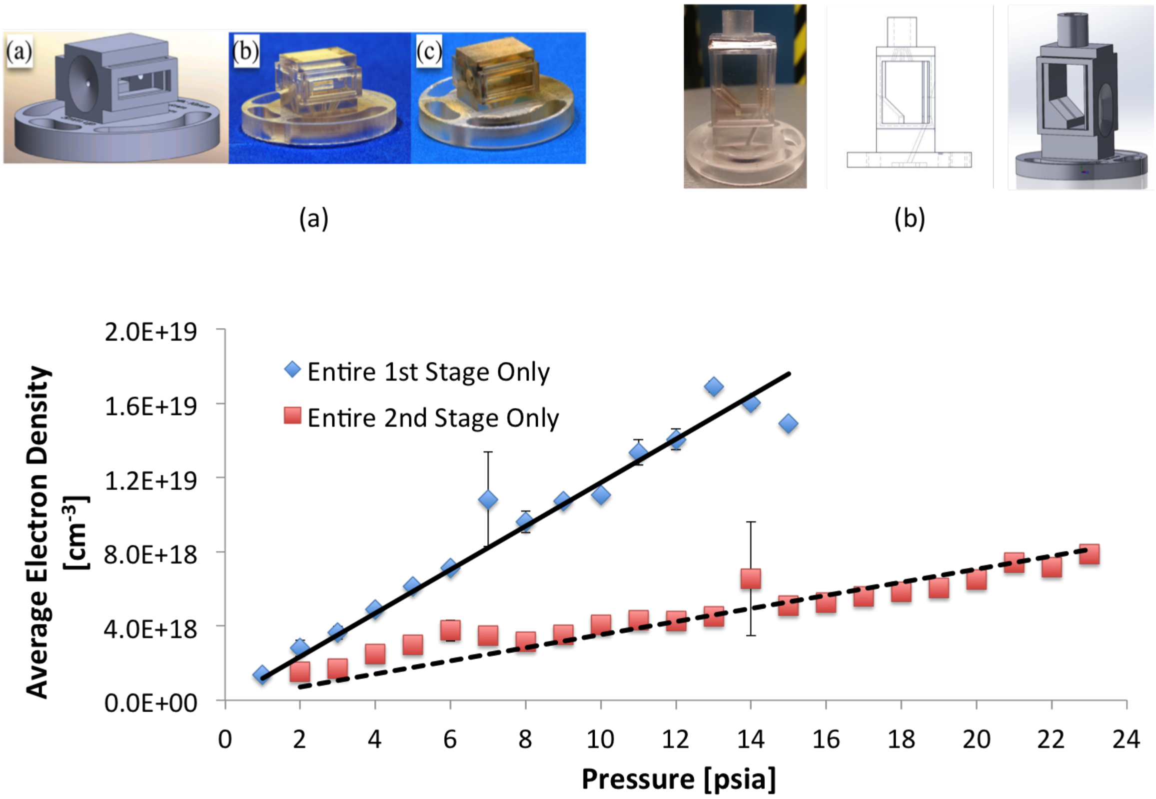

(a) (b)

(c)

Figure 3.7: (a) Images of a single stage gas cell. Laser pulse enters the cell from the left in all images. (b) Images of a two-stage gas cell. For this variant, the acceleration length can be adjusted between $5-10$ mm by adjusting the height of the cell, which then extends the interaction region due to the 45° ramp in the second stage. Laser pulse enters the two-stage cell from the right in all images. (c) Electron density versus backing pressure for each stage of the two-stage gas cell. Each data point consists of three measurements. Discussions on obtaining the density is given in Section 3.5.1 Error bars denote the standard deviation of the mean.

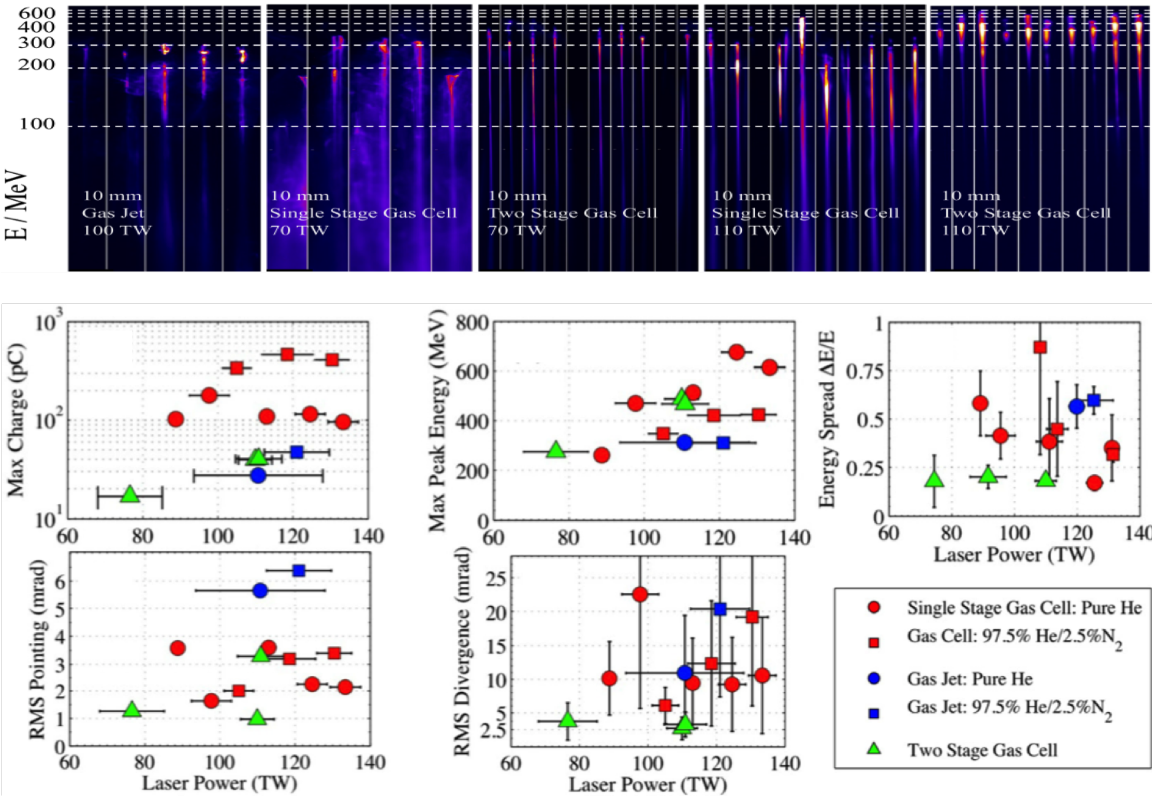

Figure 3.8: Top row: Electron beam energy spectra generated using various gas targets. Improvements in overall beam quality are observed using the two-stage gas cell over the gas jet. Bottom row: Electron beam properties as a function of laser power for the various target types. Figures from [93] with the permission of AIP Publishing.

energy spread improved noticeably, especially with the two-stage cells. The various beam parameters are plotted as a function of laser power for the different target types in bottom row of Fig. 3.8. Furthermore, longitudinal density gradients naturally exist in gas cells due to gas flow out of its entrance and exit apertures. These gradients can be useful in the self-focusing process and aid in the trapping of electrons [94].

3.5 Interaction diagnostics

Interaction diagnostics serve to quantify various aspects of the LWFA process. In general, diagnostics are required to characterize the properties of the electron beam, plasma, and emitted radiation. A summary of the optical and X-ray CCD cameras used in this thesis is given in Table 3.1.

3.5.1 Interferometry

Plasma interferometry can be used to obtain information on the electron density inside the gas cell. A 2 μm thick nitrocellulose pellicle (National Photocolor) with anti-reflection coating on one side is used to pick off a 4% Fresnel reflection of the main beam after it enters the main target chamber. The reflected beam passes through the gas cell transverse to the direction of propagation of the main pulse, before entering a shearing Michelson interferometer. A delay stage is used to adjust the timing between the main and probe pulses so that the probe pulse traverses through the plasma ~ps after the main pulse. The use of microscope glass slides in place of the printed plastic walls allowed the probe beam to access the gas cell. In the two-stage gas cell, there is a 0.5 mm divider between the stages so that density measurements could not be obtained in this region due to the printed plastic wall obstructing the view.

In the shearing Michelson setup, one arm of the probe beam is flipped and vertically offset using a prism such that the plasma region interferes with a reference region with no plasma. For the single-stage gas cell, the vacuum region above the cell is used. For the two-stage gas cell, the top half of the cell can be used for reference since the laser propagation axis is well below this height. The plasma creates a phase difference that manifests itself as a fringe shift in the interference pattern recorded by the CCD camera. The cumulative phase shift for light traveling a path l in a medium is given by [95],

$$\Delta\phi = \frac{2\pi}{\lambda} \int (\eta - 1)\ dl \tag{3.1}$$

where $\Delta\phi$ is the cumulative phase shift, λ is the radiation wavelength, and $\eta = \sqrt{1 - n_e/n_c}$ is the refractive index of the plasma. Thus, the plasma density can be retrieved from the phase shift resulting from the interference fringes. An Abel inversion algorithm using the Fourier-transform method to extract the two-dimensional phase difference map $\Delta\phi(x, y)$ was implemented in MATLAB. In 2D, the phase shift is related to the plasma density by [96],

$$\Delta\phi(x, r) = \frac{2\pi}{\lambda} \left(\sqrt{1 - \frac{n_e(x, r)}{n_c}} - 1 \right) \, dl \approx -\frac{\pi}{\lambda} \frac{n_e(x, r)}{n_c} \, dl \tag{3.2}$$

To account for a small non-axisymmetry in the plasma channel, the Abel inversion is computed numerically using a modified version of the method in Ref. [97]. The plasma densities quoted in this thesis refers to the peak on-axis electron density and are calculated either by interpolating/extrapolating measured data points or from direct reconstruction of the phase map using the interferogram image. Typical shot-to-shot variations of the measured densities are on the order of ±10%. Since the laser intensity is well above the ionization threshold for the gas types used, the variations in the densities are primarily attributed to an uneven distribution of gas within the gas cells and the flow of gas exiting the cells and between the stages of the two-stage cell variant. An image of a typical interferogram with plasma-induced fringe shifts is shown in Fig. 3.9 (a) for a two-stage gas cell. Figure 3.9 (b) shows the resulting 2D electron density map with the peak density occurring on-axis. In Fig. 3.9 (b), noise can arise due to numerically evaluating the Abel inversion which involves differentiation. As a result the peak on-axis density value is obtained by averaging over the length of the density map instead.

3.5.2 Radiation detectors

Electrons wiggling inside the wakefield cavity generate high-energy betatron X-rays. These electrons can also generate bremsstrahlung radiation by interacting with various materials in the surrounding environment after exiting the plasma. Line emission radiation can be also generated. This section describes methods that are

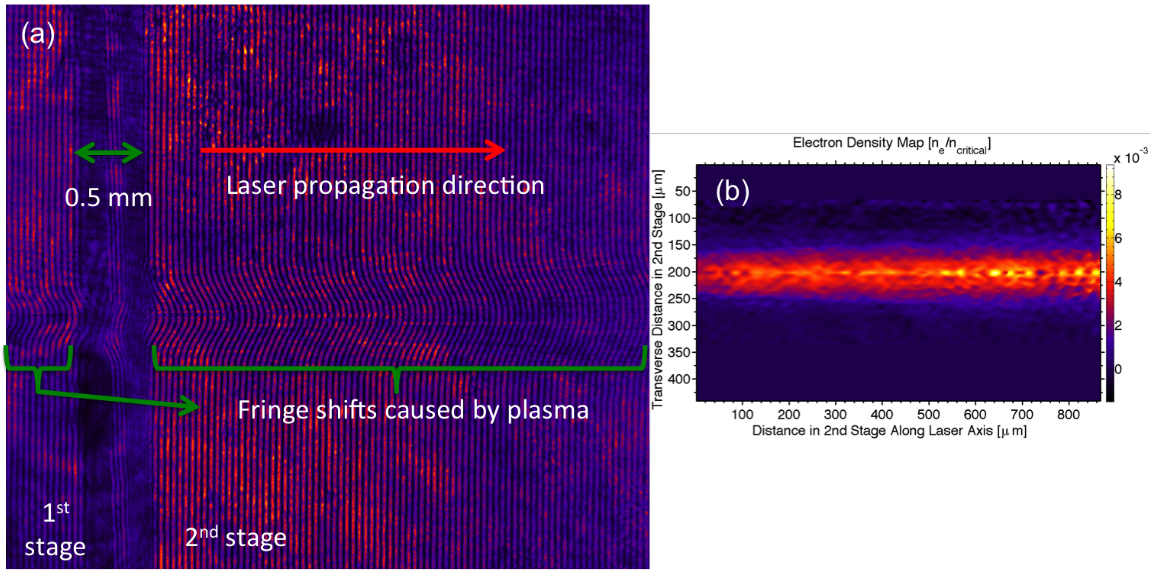

Figure 3.9: (a) Interferogram with characteristic fringe shifts due to the presence of plasma inside the gas cell. (b) 2D electron density map showing that the peak density occurrs on-axis.

used to either directly characterize the radiation, conversion of the radiation into a wavelength that is suitable for imaging using optical CCD cameras, or some other means for indirect detection.

3.5.2.1 Scintillators

A scintillator is a fluorescent material that absorbs the energy of an incoming particle or photon and re-emits the absorbed energy in the form of light that is less energetic. The emitted photon can then detected by using a CCD camera.

Both the electron beam energy spectrum and spatial profile distribution can be measured using a Kodak LANEX scintillator screen. LANEX is composed of a thin layer of Gd_2O_2S doped with La_2O_2S and scintillates light isotropically peaked around 545 nm. The ESPEC diagnostic consists of a 0.8 T dipole magnet used to spectrally disperse the electron beam onto a LANEX screen that is imaged at $\approx 45°$ using a CoolSnap CCD camera (see Section 3.5.2.3 for camera details). The magnet and LANEX screen are placed inside the main target chamber while the camera is situated outside and images the screen through a glass port of the chamber. A BG39 glass filter is used to block stray laser light from entering the camera and ambient light is blocked by enclosing the camera in a light-tight housing. The front of the ESPEC LANEX is shielded by a ≈ 0.5 mm thick piece of brass to prevent laser light and low-energy electrons and X-rays from creating noise. The electron spatial profile (EPROFILE) diagnostic consists of a LANEX screen placed at an appropriate distance on-axis, typically ~ 1.25 m downstream from the main interaction area in a jointly-connected vacuum chamber, and imaged using a CoolSnap CCD camera. This screen is usually shielded from the laser light and low-level noise using a sheet of 15 μm thick Al foil. When the spatial profile of the electron beam is being measured, the magnet is removed from the path of the electrons in order to minimize interference from the magnetic fields. However, the fringe fields of the magnet can still have a minor effect on the electron spatial distribution. It is also possible to measure the spatial profile before the magnet, in which case fringe field effects are not an issue. Cross-calibration using image plates (see Section 3.5.2.2) are performed in order to relate the signal on the LANEX to a physical value of the electron charge (2.9×10^{-6} pC/count). Mapping the electron beam position on the ESPEC LANEX to its energy and divergence can be done analytically by considering the relativistic trajectory of electrons exiting from the center of the magnet. Figure 3.10 shows example images of the electron beam on the ESPEC and EPROFILE diagnostics as well as an energy calibration for the ESPEC diagnostic.

Plastic scintillators (Eljen Technologies, EJ-200) were also placed at three locations around the gas target experimental area, each behind varying amounts of lead shielding. These scintillators were coupled to photo-multiplier tubes (PMT) so that the amplified signal could be read out on an oscilloscope. The relative X-ray signal from the different scintillators is strongly correlated with the generation and acceleration of the electron beam and serves as a first-look diagnostic during the electron

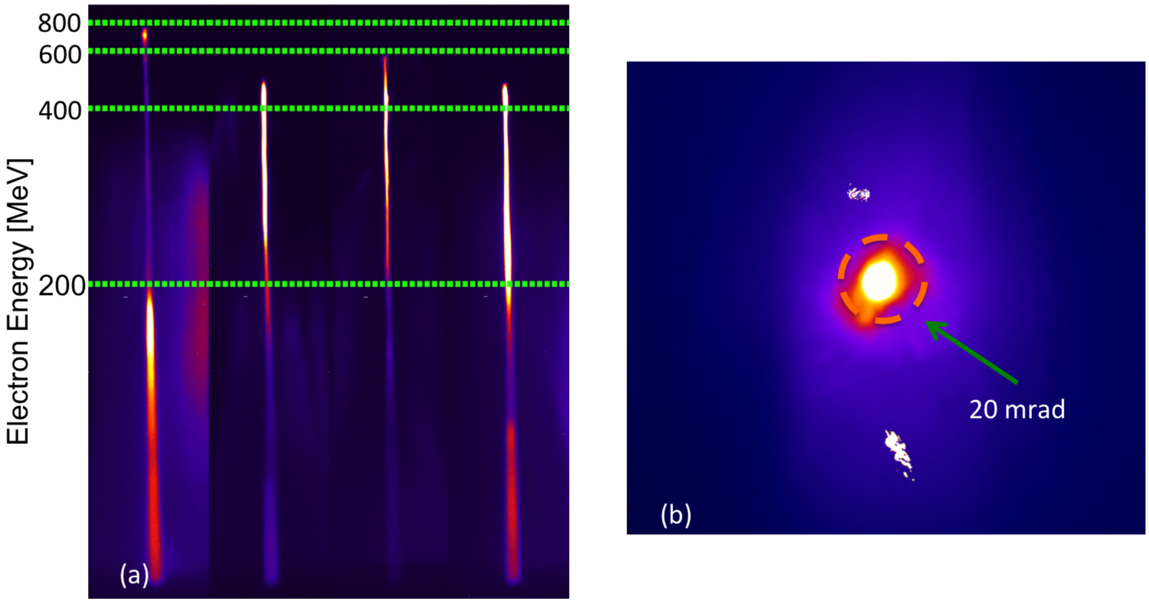

Figure 3.10: Representative images of the electron beam (a) energy spectra and (b) spatial distribution. White marks in (b) are burned pixels on the CCD camera.

beam optimization process for each experimental shot run.

3.5.2.2 Image plates

An image plate is a flexible image sensor that consists of a layer of very small crystals (grain size ~ 5 μm) of photo-stimulable phosphor with a doping concentration, BaFBr:Eu^{2+} (see Fig. 3.11 (a)) on a plastic substrate. The phosphors trap and store radiation energy in a metastable state until it is excited further into a nonstable state, usually by a helium-neon laser beam. When the ions relax from this state, photons are emitted and subsequently measured. The number of excited ions is directly proportional to the energy deposited and image plates tend to have a very linear response over a wide energy range, making them very useful for a variety of applications in radiation detection [98–101]. The energy is released as luminescence and thus, image plates operate on the principle of photo-stimulated luminescence (PSL).

There are three main types of image plates used in this thesis: MS (More Sensitivity), SR (Super Resolution), and TR (Tritium Detection). The MS type (used for the ESPEC and EPROFILE diagnostics) has a 100 μm resolution and a high enough sensitivity for the LANEX cross-calibration. The SR and TR varieties offer higher resolution (50 μm) but less sensitivity due to a thinner phosphor layer [102]. The TR type is especially useful for detection of ions and keV-level photons since they lack a protective layer; however, care must be taken when handling these in order to avoid degrading the phosphor material.

The image plates were read out using a Fujifilm-BAS 1800-II reader. The raw signal must be converted into units of PSL before analysis can be performed. The relationship between the raw signal and PSL is plotted in Fig. 3.11 (b) and is given by [99],

$$PSL = \left(\frac{R}{100}\right)^2 \times \left(\frac{4000}{S}\right) \times 10^{L[P/(2^B-1)-1/2]} \tag{3.3}$$

where typical values for the image plate reader resolution, sensitivity, latitude, and dynamic range are given by $R = 100$ μm, $S = 4000$, $L = 5$, and $B = 16$ bits, respectively and L is the raw signal count. The signal from the image plate can also decay naturally over time due to thermal effects. Thus, it is of utmost importance to analyze the signal immediately after exposure. Although this is not always possible during experiments, adjustments for the signal level due to time degradation have been well characterized for various types of image plates [103] (see Fig. 3.11 (c)) and corrections can be made during post analysis. Overexposure can be resolved by either allowing the signal to fade naturally over time, reducing the signal level via successive readouts, or using a neutral density filter on top of the image plate during readout to reduce both the laser light incident on the image plate and the de-excited light signal from the image plate.

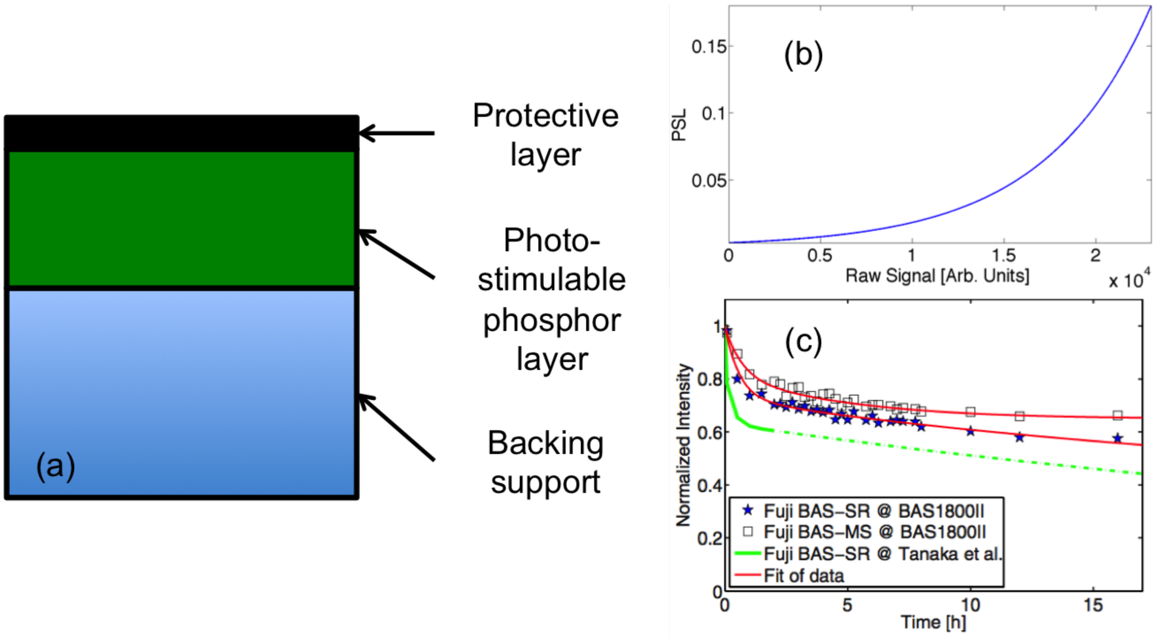

Figure 3.11: (a) Composite structure of an image plate. (b) Relationship between PSL and signal on image plate. (c) Degradation of signal on image plate over time. Figure from Ref. [103] with the permission of AIP Publishing.

3.5.2.3 Optical and X-ray CCDs

A key difference between optical and X-ray CCD cameras is the amount of signal generated by the incident photon on the sensor chip. X-ray photons have significantly more energy than optical photons and as such, they create a much larger signal in each pixel of the sensor. Back-illuminated (BR) sensors typically have thin substrates, resulting in higher absorption efficiency. Deep depletion (DD) sensors have thicker substrates that allow for the absorption of high-energy photons. Table 3.1 provides the specifications for the different cameras used in this thesis. The quantum efficiency (QE) curve for the Andor cameras are shown in Fig. 3.12 (a). The Photometrics CoolSNAP cf camera was used to image the ESPEC and EPROFILE LANEX screens as well as the plasma channel for the interferometer diagnostic and the laser pointing for the POINTING diagnostic. The Andor cameras were used to measure the TRPE and betatron spectrum, and for various imaging applications (not included in this thesis). The betatron spectra were reconstructed using the method of single photon counting [104, 105] (see Appendix A). An energy calibration for the ikon-M SO camera was conducted in vacuum using an Fe-55 source situated 12 cm from the unfiltered CCD chip. To ensure adequate statistics were achieved, the calibration was averaged over a hundred exposures with a 200 ms exposure time for each. The source is expected to emit line radiation at 5.899 (6.49) keV with a corresponding intensity of 16.2% (1.89%) for the K_{α_1} (K_{β_1}) emission [106]. As shown in Fig. 3.12 (b), the energy calibration matches reasonably well with the expected energy and intensity values. The FWHM of the K_α (K_β) peaks was measured to be 147.6 (158.1) eV. At the date of calibration (20150130), the source activity was calculated to be 1.319 MBq. The camera settings were set to a shift speed of 5.775 μs, a normal vertical clock voltage amplitude, a readout rate of 2.5 MHz at 16-bit, and a preamplifier gain of 1X.

Manufacturer	*Photometrics*	*Andor*	*Andor*
Camera	CoolSNAP cf	ikon-M SO	Classic SX
Peak Q.E.	36%	95%	95%
Active Pixels	1392 × 1040	1024 × 1024	1024 × 255
Pixel Size	$4.65 \times 4.65\ \mu m^2$	$13 \times 13\ \mu m^2$	$26 \times 26\ \mu m^2$
CCD Format	N/A	BR, DD	BR
Dynamic Range	12-bit	16-bit	16-bit
Readout Noise	±4 counts	± 2.9 e$^-$	± 4 e$^-$
Operating Temp.	Room temp.	−40° C	−40° C
Connector Type	PCI Frame Grabber	USB	USB

Table 3.1: Specifications of optical and X-ray CCD cameras used in experiments. The Q.E. is a measure of the photon-to-electron conversion efficiency in the sensor for a given photon energy/wavelength. BR: Back-illuminated, DD: Deep depletion.

3.6 Computational modeling

Computational modeling can be useful to gain a deeper understanding into the complex and nonlinear interactions that take place during high-intensity laser-matter interactions and are often necessary when analytical frameworks either do not exist

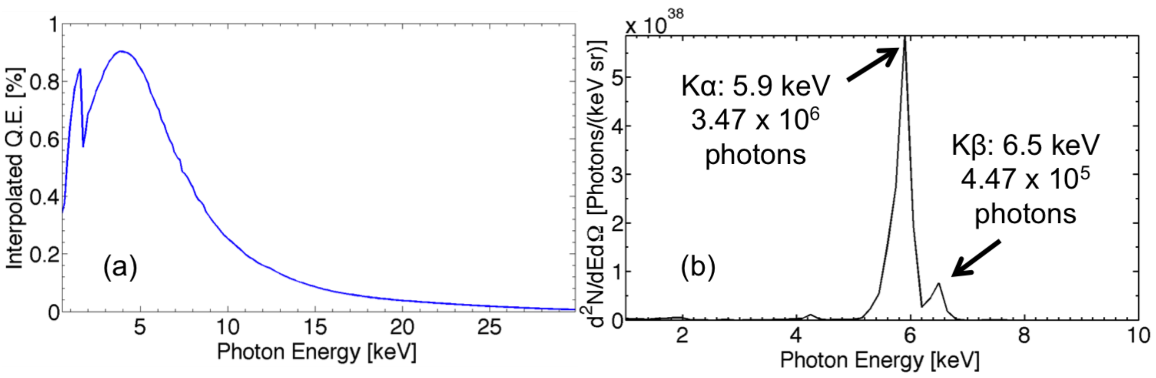

Figure 3.12: (a) Quantum efficiency curve for the Andor cameras recreated with a plot digitizer using values provided by Andor. (b) Energy calibration for the ikon-M SO camera using an Fe-55 source. The characteristic line emissions and their intensities agree reasonably well their expected values [106]. The FWHM energy resolution of the K_α and K_β peaks are 147.6 and 158.1 eV, respectively.

or are insufficient. In addition, computer simulations allow us to conduct parameter scans that would be impractical to do in a laboratory setting due to resource constraints. In this thesis, PIC simulations were conducted to investigate the conditions under which a two-component electron beam can be generated (Chapter V) and to verify the physics behind the radiation emission increase resulting from the electron hosing instability (Chapter VI).

3.6.1 Particle-in-Cell simulations

The PIC method is a widely used technique for modeling the physical processes that occur during high-intensity laser interactions [107] and is especially suited for systems with many degrees of freedom. In the PIC method, individual particles are grouped together to form macro-particles with identical charge-to-mass ratios so that the equations of motion and macroscopic fields are still the same. Issues with microscopic interactions are essentially mitigated by the finite particle approximation or, equivalently, by mapping the fields to finite grid sizes. The method tracks the motion of a collection of these macro-particles on the grids and subjects them to a set of self-consistent electromagnetic fields. In general, the laser wavelength, Debye length, and the Courant-Friedrichs-Lewy condition ($\Delta x \geq c\Delta t$) must be properly resolved in order to avoid unphysical spatial, thermal, and temporal instabilities, respectively. Most PIC implementations follow the steps below:

1. Update particles: Each macro-particle's phase space (i.e., position and momentum) vector is updated according to the relevant equations of motion.
2. Distribute particles: The current and charge densities resulting from the updated phase space vector is calculated using a weighted distribution.
3. Solve fields: Solve Maxwell's equations using the updated current and charge densities. External fields such as the laser pulse and the self-fields from the charged particles are included as well.
4. Update fields: Update the electromagnetic fields on the weighted grid and return to step 1.

For this thesis, PIC simulations were conducted using the OSIRIS 2.0 framework developed at UCLA [108] and run on the Nyx cluster at the University of Michigan. OSIRIS is a fully explicit, parallelized, and relativistic 3D code that is used to simulate conditions present in plasma based accelerators, fast ignition, and relativistic shocks. These simulations are often expensive to run due to the number of processors used and length of time required per simulation. Thus, LWFA simulations are conducted using a moving box reference frame that co-propagates with the laser pulse. This allows efficient simulations of the pulse evolution and the surrounding plasma over long propagation distances. In these simulations, the ions are considered stationary during the interaction and only the electron dynamics are relevant. The laser pulse can either interact with a pre-ionized background density at the beginning of the simulation or particles can be injected from a background gas based on the ionization method. The plasma profile and laser pulse parameters can be readily adjusted to fit the experimental conditions.

CHAPTER IV

Electrons and X-rays Produced Using Chirped Pulses in the Laser Wakefield Regime

4.1 Introduction

Plasma-based laser accelerators are known for generating both high-quality electron and X-ray beams. As the pulse propagates, the feedback from the collective plasma motion on the laser pulse leads to the evolution of the pulse envelope and phase, which in turn affects the electron beam phase space structure. For example, pulse self-steepening at the leading edge lowers the group velocity of the bubble and limits energy gain by reducing the dephasing length. This can also cause elongation of the bubble and continuous injection, resulting in a non-monoenergetic energy spread [109]. The properties of the emitted radiation are directly coupled to that of the electron beam and optimization of the electron injection process can lead to favorable X-ray characteristics such as smaller source sizes or increased flux.

The injection process is sensitive to the laser pulse duration, frequency chirp, and shape. Depending on the ratio of the pulse duration to the relativistic plasma wavelength, the evolution of the wakefield occurs in either the LWFA, forced-LWFA, or SM-LWFA regime (cf. Table: 2.1). In both the forced and SM-LWFA regimes, it is also possible for the laser field to directly accelerate the electrons [110]. With regard to frequency chirping and pulse shape, theoretical and experimental studies have shown that a positively chirped pulse, with a fast-rising leading edge, can increase self-trapping of electrons by increasing the wakefield amplitude generated by the chirped pulse. The higher amplitude wakefield helps to decrease the minimum momentum required for trapping electrons [32, 44, 111–116]. On the other hand, simulations have shown that incoherently stacking negatively chirped pulses of different wavelengths can be used to create electron beams with energies higher than that obtained using optimally compressed pulses. The negatively chirped pulse compensates for the red-shifting occurring at the front of the bubble and slows pulse self-steepening. This results in a decrease in the pump depletion occurring at the leading edge of the drive pulse and effectively increases the length over which the electron can be accelerated [45]. However, this technique requires a pulse bandwidth, $\Delta\omega$, on the order of the carrier frequency, ω_0, and is not feasible for most CPA systems.

In these previous studies, the energy of the electron beam and the resulting X-ray emission were not experimentally characterized as a function of the drive pulse parameters. Furthermore, with the exception of Ref. [116] where the experiment was conducted in the SM-LWFA regime, a parameter scan for the various pulse parameters across different electron densities was not conducted. In Ref. [116], it was observed that the background density played an important role in the increase in injected charge due to an asymmetric pulse shape. In this Chapter, we investigate the effect of chirped, asymmetric laser pulses on the electron injection process and the associated radiation emission in the LWFA regime. The integrated electron charge and peak energy, along with the TRPE (i.e., X-ray flux), is characterized as a function of the electron density and drive pulse characteristics (i.e., pulse duration, shape, and frequency chirp). In addition, we also compare the X-ray spectra resulting from the betatron oscillations of the electrons inside the wakefield cavity for two different gas types as a function of the pulse characteristics. These studies are important

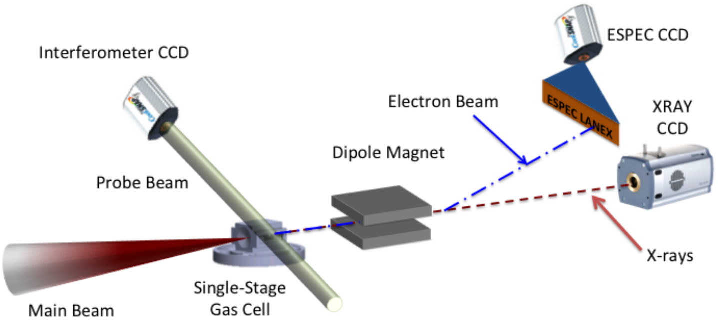

Figure 4.1: Schematic of the experimental setup. The main beam is focused using an $f/20$ off-axis paraboloid onto a single-stage gas cell filled with either a mixed gas (97.5% He and 2.5% N_2) or pure He. Electrons exiting the cell were deflected by a dipole magnet and imaged using the ESPEC diagnostic. The radiant energy was measured 2.5 m downstream using an Andor CCD camera.

for understanding the effects of pulse parameters in the LWFA process for a typical high-intensity laser system.

4.2 Experimental setup and pulse shape measurements

For these experiments, the main beam was focused using an $f/20$ off-axis paraboloid to a vacuum beam waist $w_0 = 26$ μm (at $1/e^2$ of peak intensity). The energy spectra of the electron beams were measured using the ESPEC diagnostic and the X-ray flux was measured using the Andor iKon-M BR-DD camera, placed 2.5 m downstream from the interaction region. The X-ray camera was shielded from the laser light using a 50 μm Be window. Figure 4.1 shows the setup.

Measurements of the time-dependent intensity and phase of the laser pulse were conducted using a SHG-FROG device with the milli-Joule level regenerative amplifier beam. This allowed the pulse shape to be uniquely determined by using a multiparametric fitting algorithm [117]. Slight asymmetries in the experimentally measured FROG traces can occur along the time axis due to a combination of spatial chirp and pulse front tilt. In order to analyze a larger portion of the measurements, the traces were symmetrized using an average of the left and right portions of the trace. The compressor grating separation was varied to obtain the shortest root mean square (RMS) pulse duration with minimal frequency chirp. This grating position is referred to as the "compressor zero". The duration, shape, and frequency chirp of the pulse was then simultaneously varied by changing the separation of the compressor gratings. Decreasing (increasing) the separation of the compressor gratings imparted a positive (negative) frequency chirp as well as stretching the pulse. In addition, the leading edge slope changed from 0.02 to 0.027 to 0.013 intensity/fs for positively chirped, optimally compressed, and negatively chirped pulses, respectively. As the pulse was stretched, its energy remained constant. Figure 4.2 shows typical intensity profiles for chirped and optimally compressed pulses and the pulse duration as a function of the relative grating separation from compressor zero.

4.3 Experimental results

4.3.1 Experimental parameters

The experiments were carried out in two separate portions. For the first portion, the laser beam delivered an average energy of 1.8 J on target in a 34 fs pulse (peak intensity 2.0×10^{19} W/cm^2). A 3D-printed 5 mm single-stage gas cell was used as the target [93] and was filled with a gas mixture (97.5% He and 2.5% N_2) [62, 63]. In the second portion, a 25/75% (reflection/transmission) 800 nm beamsplitter was present in the chamber, which effectively reduced the average energy on target to 1.4 J. A 3 mm single-stage gas cell was used, with the cell filled with either the 2.5% N_2 mixture or pure He depending on the parameter being scanned. For the first experiment, the electron densities were scanned from below injection threshold to

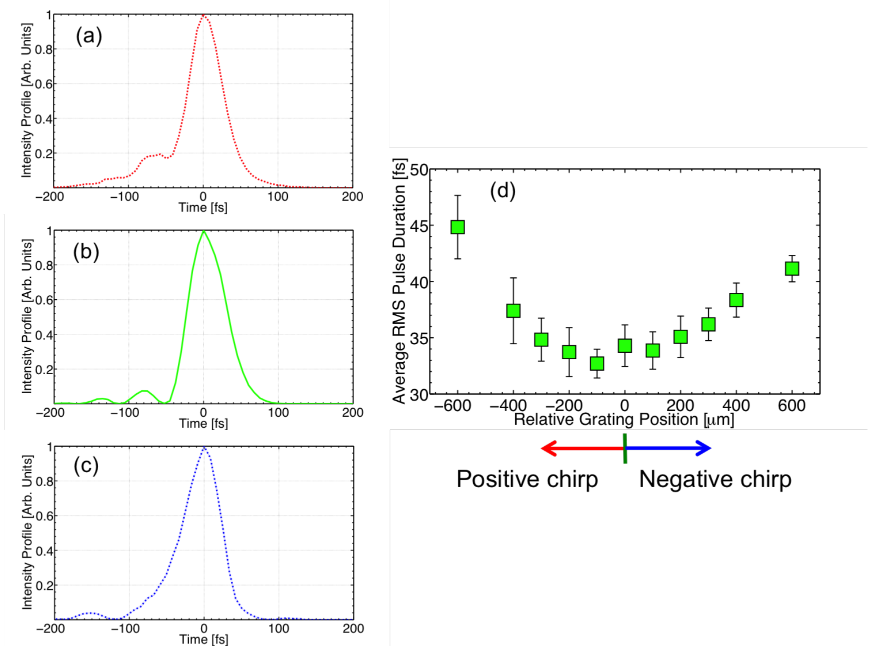

Figure 4.2: Typical time-dependent intensity profile of the laser pulse for (a) positive chirps, (b) optimal compressor setting, and (c) negative chirps. Negative times corresponds to the leading edge of the pulse. (d) Average RMS pulse duration as a function of the relative grating position.

significantly above threshold. Figure 4.3 shows typical electron spectra (generated using the mixed gas) corresponding to four of the density steps scanned. At the lower densities, quasimonoenergetic electron beams with low charge (< 100 pC) and divergence (< 20 mrad full-angle) were generated. As the density increased, the wakefield cavity becomes increasingly loaded with electrons and large divergence and energy spread beams are formed. Data from the first experiment are shown in Figs. 4.4 (a) - 4.4 (c), while Figs. 4.4 (d) and 4.5 show data from the second experiment.

4.3.2 Electron charge and energy and X-ray flux

In Fig. 4.4 (a), the integrated electron charge on the ESPEC LANEX is plotted as a function of the relative grating separation for several different electron densities. The threshold density for electron injection for this data set was found to be 8.2×10^{18} cm^{-3}. This was verified by noting that a less than 5% decrease in the density resulted

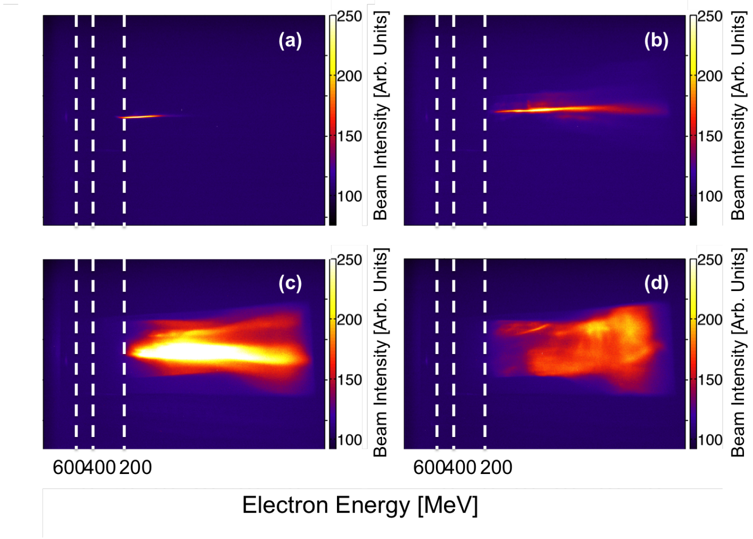

Figure 4.3: Representative images of electron spectra from the ESPEC diagnostic for electron densities (a) 7.9 (b) 8.2 (c) 11 and (d) 13×10^{18} cm^{-3}. Quasimonoenergetic beams were generated at the lower densities while higher densities produced large-divergence beams with a larger energy spread.

in a significant reduction in the electron beam charge and reproducibility at the shortest pulse duration and is reflected in Fig. 4.4 (a). The integrated electron charge was calculated by summing the total number of counts on the ESPEC LANEX which were then converted to charge via a cross-calibration technique using a FUJI BAS-MS image plate. The corresponding radiant energy produced by the betatron oscillations of the electrons from Fig. 4.4 (a) was calculated by directly summing the counts on the Andor CCD chip and is shown in Fig. 4.4 (b). The relationship between the radiant energy and the electron charge is plotted in Fig. 4.4 (c) and peak electron energies (defined as the energy containing the highest charge on the ESPEC LANEX) as a function of the relative grating separation are shown in Fig. 4.4 (d) for both gas types.

4.3.3 Betatron spectra

Figure 4.5 shows the X-ray spectra for both gas types as a function of the relative grating separation. Each spectrum is averaged over five to ten shots using the method

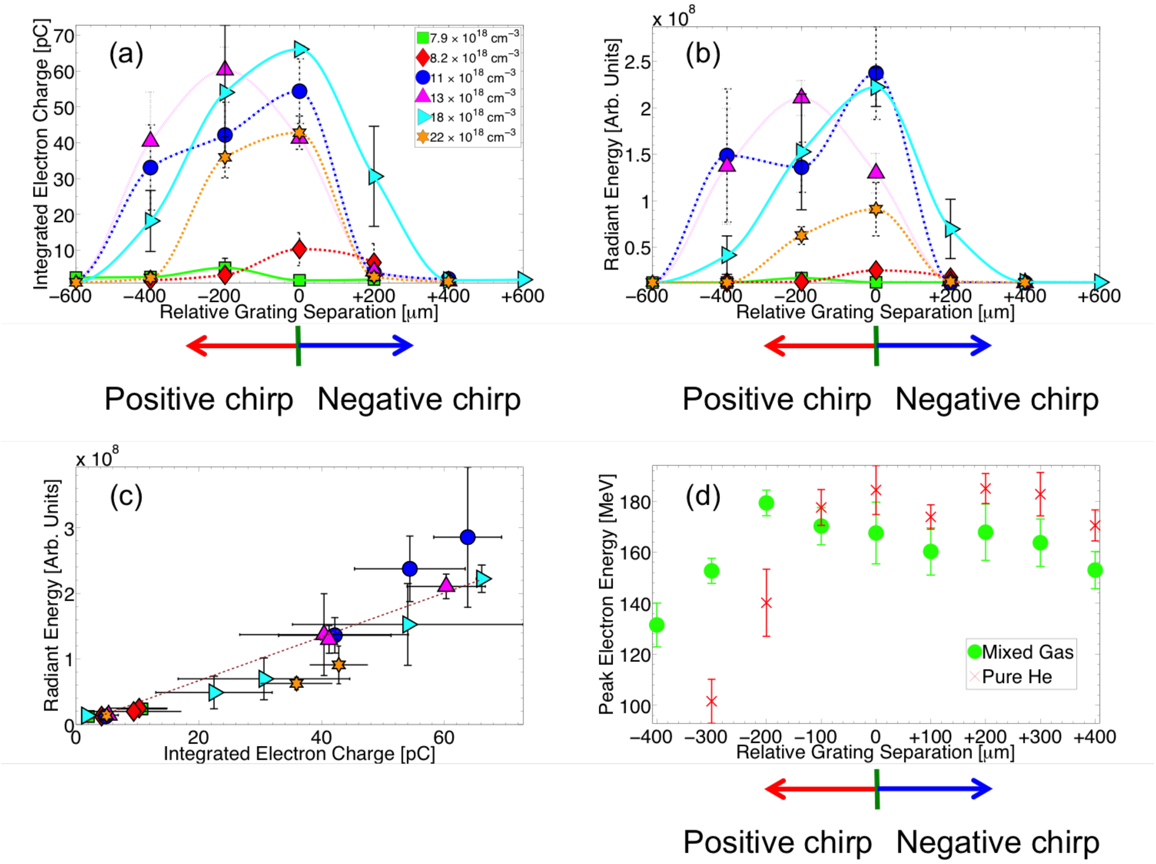

Figure 4.4: (a) Measurements of the integrated electron charge as a function of the relative grating separation for various electron densities (legend in inset). For similar separations, positive chirps produced more charge compared with negative chirps. (b) The corresponding effect on the radiant energy followed a similar trend. In both (a) and (b), the curved lines serve as a visual aid in connecting the data at each density step. (c) The radiant energy scaled linearly with the electron charge and was independent of the drive pulse parameters (dashed line denotes a linear fit to the data). (d) Peak electron energy as a function of compressor grating separation for the mixed gas (green circle) and pure He (red x). Error bars denote the standard error of the mean.

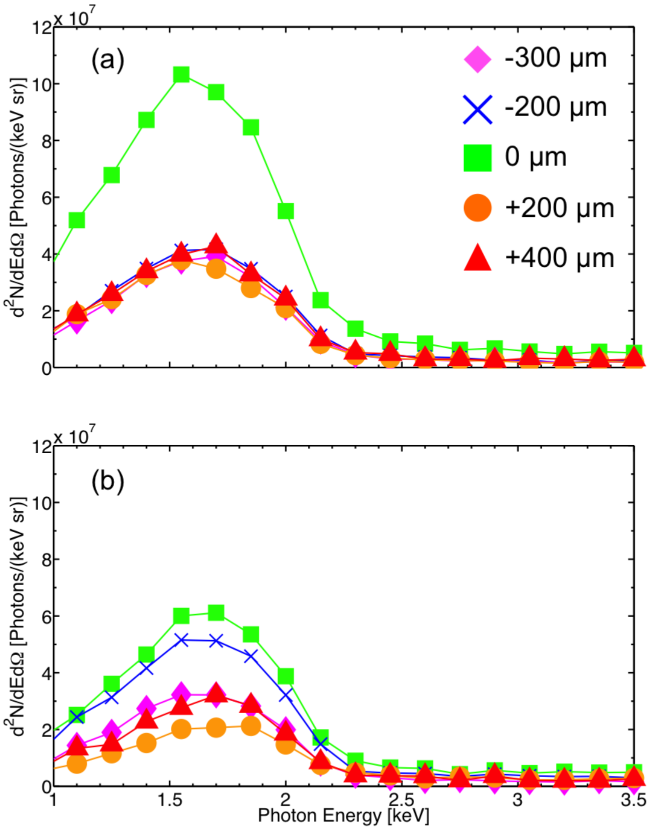

Figure 4.5: (a) X-ray spectra for the 2.5% N_2 mixed gas at different relative grating positions. The greatest number of photons was produced at the compressor zero setting (i.e., the shortest pulse duration with minimal frequency chirp). (b) X-ray spectra for pure He. A similar trend was observed for pure He as that for the mixed gas but with a larger spread in the photon flux around the peak energy.

of single photon counting (see Appendix A). Electron densities were nominally set to 6.5×10^{18} cm^{-3} so that the integrated number of hits on the camera remained within the single photon counting regime. In order to maintain injection at the larger grating separations (i.e., longer pulse durations), the density was increased up to a maximum of 10×10^{18} cm^{-3}. For the parameter range scanned, the probability of a double hit occurring based on Poisson statistics ranged between $0.5 - 4.8\%$ on average. The algorithm used to construct the spectra is able to correct for predicted double hits for probabilities less than 15%.

4.4 Discussion

Due to the different pulse durations and densities scanned, the operating regime of the wakefield spanned from the bubble regime of LWFA (at the shortest pulse duration and lowest density where $L_{laser} \approx 10\ \mu$m and $\lambda_p \approx 26\ \mu$m) to nearly the forced-LWFA regime (at the longest pulse duration and highest density where $L_{laser} \approx 14\ \mu$m and $\lambda_p \approx 18\ \mu$m). In these regimes, positively chirped pulses with fast-rising leading edges increased the injected charge and decreased the peak electron energy, and vice versa for negatively chirped pulses. The leading edge of the pulse undergoes localized pump depletion and a steep intensity gradient forms at the leading edge. The localized depletion, combined with self-compression, causes asymmetries in the electron charge and energy between the differently chirped pulses. The laser group velocity (taking into account localized pump depletion) is given by, $v_g = v_g^1 - v_{depletion}$, where $v_g^1 \equiv c[1 - \omega_p^2/(2\omega^2]^{1/2}$ is the linear group velocity and $v_{depletion} = c\omega_p^2/\omega_0^2$ is the velocity at which leading edge of the pulse depletes away [69]. Thus, a positively chirped pulse (where lower frequencies lead in time) etches faster and as a result, propagates at a lower group velocity. Since the phase velocity of the wake behind the laser pulse propagates at approximately the laser group velocity, the wake phase velocity is lower for positively chirped pulses. The lower phase velocity then lowers the threshold for electron trapping.

In the regime of SM-LWFA, the Raman forward scattering (RFS) instability is responsible for the asymmetry in the electron charge and energy [18]. For short laser pulses, the Raman instability is predominantly seeded by the ponderomotively excited plasma waves [118]. Although both the frequency chirp and pulse shape asymmetry are capable of generating larger plasma waves that feed the instability, studies have shown that the enhancement is primarily due to the asymmetric pulse shape [32, 115, 116]. The reason for this is that the propagation distance required for the linear chirp to affect the RFS growth is typically much greater than the growth length for the RFS instability, i.e., $k_p L_{GVD} \gg w_p/\gamma_{RFS} = [8(n_c/n_e]^{1/2}/a_0$, where γ_{RFS} is the RFS growth rate, $L_{GVD} \simeq c\lambda_p/\Delta v_g$ is the propagation distance required for a linear chirp to significantly affect the RFS growth and $\Delta v_g \simeq -c(n_e/n_c)(\Delta\lambda/\lambda)$ is the change in the group velocity due to the frequency chirp [115]. Using a typical HERCULES bandwidth of $\Delta\omega/\omega_0 \sim 0.04$ and the densities and powers relevant to this experiment, $k_p L_{GVD} \sim 10^4 \gg w_p/\gamma_{RFS} \sim 10^1$, and thus, the frequency chirp contribution is negligible.

In general, strong asymmetries in both the electron charge and peak energy (and hence, the radiant energy) with respect to the relative grating position can be seen in Fig. 4.4 for all electron densities. Analyses of the pulse shape showed that positively chirped pulses exhibited a fast-rising leading edge compared with negatively chirped pulses. The fast-rising leading edge thus serves to enhance trapping of electrons as previously observed in the LWFA regime. For example, an increase in charge was observed in Ref. [32] where $L_{\text{laser}}/\lambda_p \approx 1$ and Ref. [44] showed an increase for $L_{\text{laser}}/\lambda_p \approx 1.8$ when a fast-rising positively chirped pulse was used as opposed to the optimally compressed pulse. On the other hand, negatively chirped pulses with slow-rising leading edges increase the wake phase velocity and consequently, the threshold for trapping.

In contrast to previous studies, the shortest pulse duration (at compressor zero) still produced the highest number of accelerated electrons in the wakefield. From Figs. 4.2 (a) and (b), we see that the slope of the leading edge of the pulse is comparable for positively chirped and optimally compressed pulses. As a result, the shorter pulse duration at compressor zero drives the more efficient wakefield and produces the highest injected charge due to the higher intensity. For example, a grating change of ± 200 μm from compressor zero changes the pulse duration by approximately 3 fs with a corresponding decrease in the peak intensity of approximately 10%.

In Ref. [116], an enhancement in the electron charge was observed for pulses with positive chirps at two different electron densities. These experiments were conducted in the SM-LWFA regime where $L_{\text{laser}}/\lambda_p \approx 6$. In particular, the charge increase was more significant at the lower electron density. This was attributed to an enhancement in the forward Raman scattering instability at lower densities in the SM-LWFA regime. In Ref. [113], simulations showed an enhancement in the injected charge/energy in the LWFA regime when comparing between chirped pulses only. In our experiment, we scanned densities from below the injection threshold to significantly above threshold. A substantial enhancement in the charge was only observed at an electron density of 13×10^{18} cm^{-3}. Densities on either side this value shifted the optimal grating position for electron injection back to the compressor zero setting. At best, this enhancement was on par with the charge produced at other densities at the compressor zero setting.

Measurements of the peak electron energy showed that negatively chirped pulses produced beams with higher peak energies than their counterparts on the positively chirped side. This trend was observed for both gas types as well. In addition, the peak energies obtained using negatively chirped pulses are comparable to those obtained at the compressor zero setting. This demonstrates the compromise that must be considered when optimizing the electron beam by changing the properties of the drive pulse. That is, positively chirped pulses with fast-rising leading edges generally inject more electrons into the bubble but at lower peak energies compared with negatively chirped pulses with a slow-rising leading edge.

Inspection of Figs. 4.4 (a) and (b) also show that the ratio between the radiant energy and electron charge is relatively constant and does not depend on the pulse characteristics. This is made even more evident in Fig. 4.4 (c) which shows the relationship between the integrated electron charge and the emitted X-rays to be fairly linear over a threefold change in the electron density. The dashed lined in Fig. 4.4 (c) is the best fit to the experimental data of the form $R = a \times Q$, where R is the radiant energy, Q is the integrated electron charge [pC], $a = 9.8$. In Fig. 4.4 (c), no distinction has been made with regard to the pulse duration, pulse shape, or sign of the frequency chirp.

As shown in Fig. 4.5, the shape of the X-ray spectra remains the same and the peak energy does not change appreciably ($\approx 10\%$ shift) with compressor separation (i.e., with changing pulse characteristics). For both gas types, the primary effect of changing the pulse characteristics is a difference in the total number of photons in the spectra and, in particular, the number of photons around the peak energy. This is to be expected since the betatron emission depends on both the number of oscillating electrons in the beam (i.e., overall charge) and the peak energy of the beam. Thus, even though positively chirped pulses produced more accelerated electrons, the peak energies of those electrons were significantly lower and vice versa. The highest photon flux then occurs for optimally compressed pulses since they produced both the highest charge and highest energy electrons. Furthermore, the variation in the photon flux can be attributed primarily to changes in the pulse duration and shape rather than the sign of the frequency chirp since both positively and negatively chirped pulses experienced a decrease in the photon flux. As mentioned above, the electron density was also increased slightly in order to sustain injection at the longer pulse durations. However, the densities were changed by the same amount for both gas types at each compressor setting. Thus, differences in the spectra for the two gases cannot be a result of the density change alone since one would expect the total number of photons to increase with electron density regardless of the pulse parameters [cf. Fig. 4.4 (c)].

For the mixed gas spectra, the standard error of the mean for the number of photons at the peak energy is 18% at the compressor zero and an average of 41% for the other settings. For the pure He spectra, the error is 30% at the compressor zero and an average of 51% for the other settings. Even with the relatively large error in the flux at the non-optimal grating separations, the shortest pulse duration still produced the highest photon flux for both gas types. The flux is also generally higher for the mixed gas as a result of the higher average electron charge created in the ionization injection process. Ionization injection also produced a smaller variation in the synchrotron spectra compared with self injection. The smaller spread in the X-ray spectra for the mixed gas can be explained by considering the differences in the injection process between the pure He and mixed gas. The majority of electrons in the mixed gas (resulting from nitrogen) are freed near the peak of the laser pulse. Thus, pulses with asymmetric rise/fall times are less likely to significantly affect the ionization injection process for the mixed gas. For the pure He case, changes in the pulse characteristics can enhance laser self-focusing and self-steepening, both of which plays a larger role in the self-injection process.

4.5 Conclusion

Our experiments showed that altering the laser pulse properties in a typical Ti:Sapphire CPA system can affect the electron injection process which in turn directly affects the emitted radiation. Positively chirped pulses with a fast-rising leading edge led to an increase in the electron charge compared with negatively chirped pulses with a slow-rising leading edge but produced electron beams with lower peak energies. The trend in the X-ray flux matched that of the integrated electron charge. The emitted radiation also scaled linearly with the electron charge over a threefold change in the electron density, independent of the laser pulse characteristics. X-ray spectra showed that the 2.5% mixed gas produced more photons than the pure He and had a smaller spread in photon number in the spectra due to the ionization injection process.

Simulations that showed an increase in the electron charge/energy using chirped pulses required pulse bandwidths on the order of the carrier frequency in order to significantly change the pulse length [45, 113]. The bandwidth of the HERCULES system was insufficient to produce a significant change in the pulse shape for positively and negatively chirped pulses. Hence, optimal pulse characteristics generally produced the highest number and peak energy of injected electrons and photons due to the higher intensities. It is conceivable that a CPA system combined with an optical parametric amplifier (OPA), known as an optical parametric chirped pulse amplification (OP-CPA) system, can be used to provide sufficient bandwidth and impart a significant asymmetry to the pulse shape [119]. In addition, pulse shaping can also be accomplished by using spatially patterned masks (phase and amplitude masks), spatial light modulators (liquid crystal arrays, acousto-optic modulators, deformable mirrors), and holographic masks [120].

CHAPTER V

High Flux Femtosecond X-ray Emission from Controlled Generation of Annular Electron Beams

5.1 Introduction

In the bubble regime, 3D plasma waves propagate at near-luminous speed and evolve synchronously with the optical driver, readily trapping background electrons. The self-injection process (which defines the electron beam phase space structure) can thus be controlled by modifying the drive pulse parameters, such as chirping the frequency [32, 113], shaping the pulse temporal profile [121], or changing the focusing geometry [94, 122, 123]. This process can also be accomplished by tailoring the plasma density profile. In particular, self-injection can be localized to a region in space by introducing density gradients along the laser pulse propagation path [94, 124]. These gradients affect the evolution of the wave buckets and can be used to minimize the electron beam energy spread [65, 125–127].

In this Chapter, we demonstrate a unique example of electron beam phase space control that relies on both density profile modification (i.e., introduction of a density downramp and tailoring the electron density in both stages of a two-stage gas cell) as well as manipulation of the drive pulse parameters (i.e., varying pulse length while simultaneously introducing a positive frequency chirp). As a result, we observe electron beams composed of two components: a collimated axial beam with a continuous energy spectrum and a quasimonoenergetic annular beam carrying up to 20% of the total charge. The experiments also reveal almost an order of magnitude increase in the total radiant energy of the emitted X-rays per unit electron charge when the annular feature is present. This opens a route to increasing the brightness and flux of compact X-ray sources relative to other plasma-based schemes [12, 19, 71, 79]. A possible explanation for the creation of these annular beams has been put forth in Ref. [128] using simulations conducted with a uniform density profile consisting of an initially neutral mixture of 98%/2% He/N_2 gas. The formation of the annulus is attributed to self-injection into the second bucket of the wake, decay of the second bucket in the course of drive pulse depletion, and partial capture of released electrons by toroidal focusing pockets around the first bucket. This explanation, however, does not provide a plausible explanation for the significant increase in the emitted radiation since the annulus is not subjected to the same accelerating and focusing fields inside the wakefield cavity. Discussions regarding other possible scenarios for generating these two-component beams and the radiation increase are provided in Section 5.4.

5.2 Experimental setup and procedures

Figure 5.1 shows the experimental setup. The laser beam, delivering up to 3.0 J on target, was focused using an $f/20$ off-axis paraboloid to a vacuum beam waist $w_0 = 26$ μm (at $1/e^2$ of peak intensity). Second-order autocorrelation yielded a 34 fs duration of the fully compressed pulse (FWHM in intensity). Decreasing the separation of the compressor gratings stretched the pulse, while simultaneously imparting a positive frequency chirp. On-target peak intensities were thus on the order of 10^{19} W/cm^2. A 3D-printed two-stage gas cell was used as the target. The cell is nominally composed of a 1 mm higher-density injection stage, a 0.5 mm divider slit for stage separation,

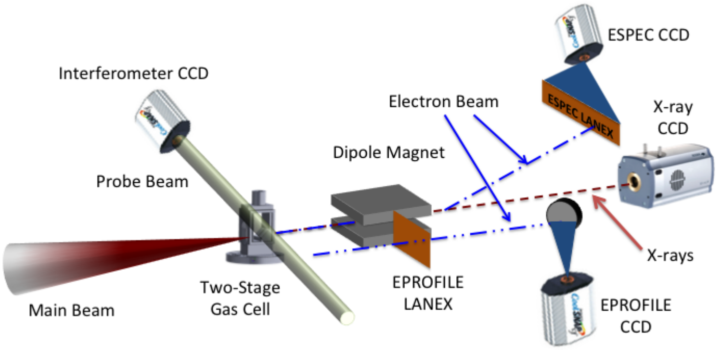

Figure 5.1: Schematic of the experimental setup. The main beam is focused using an $f/20$ off-axis paraboloid onto a two-stage gas cell. Electrons exiting the cell were either deflected by a dipole magnet and imaged using the ESPEC diagnostic or undeflected and imaged on-axis at 12 cm from the cell exit using the EPROFILE diagnostic (magnet removed in this case). The dash-double-dot line shows the trajectory of the undeflected electrons.

and an adjustable $5-10$ mm low-density acceleration stage.

The experiments were conducted with the first stage filled with either pure helium or a gas mixture (97.5% He and 2.5% N_2). The majority of shots were made with the mixed gas in the first stage. Observations, however, showed no evidence that the chemical composition of the first stage gas was essential in generating the annular beams. The second stage was always filled with pure helium. The energy spectra of both the axial and annular electron beams were measured using the ESPEC diagnostic. The spatial profile of the electrons was measured using an EPROFILE system consisting of a different LANEX screen positioned 12 cm from the exit of the gas cell and shielded from the laser light with 100 μm of Cu foil. X-ray measurements were conducted using an Andor iKon-M BR-DD camera placed 2.5 m downstream from the interaction region and shielded from the laser light using two layers of 1.8 μm Al and a 6 μm aluminized Mylar foil. A 2 μm thick nitrocellulose pellicle reflected

4% of the main beam and was used to probe the gas cell in the transverse direction before entering a shearing Michelson interferometer, thus allowing electron density measurements to be taken. The use of microscope glass slides in place of the printed plastic walls allowed the probe beam to access each stage of the gas cell. Density measurements could not be obtained in the region between the two stages due to the printed plastic wall obstructing the view.

5.3 Experimental results and discussion

5.3.1 Annular beam generation

The annular beams were generated for densities in both stages ranging from 2 to 8×10^{18} cm^{-3}, laser energy between 2.4 to 3.0 J, acceleration stage length ranging from 5 to 9.5 mm, and pulse duration between 34 and 135 fs. Optimal combinations of these parameters yielded the annular beams on approximately 40% of shots. When the annular beams were present, the ratio of the electron density in the 1$^{\text{st}}$ stage relative to the 2$^{\text{nd}}$ stage was always greater than unity (1.4 on average). Thus, the presence of a density downramp between the stages was critical in forming the annular feature. The density value in each stage also affected the appearance of the annular beams. Instabilities in creating the annular beams are most likely due to changes in the plasma density in each stage of the gas cell ($\sim$ 10% shot-to-shot variation) and shot-to-shot fluctuations in the laser beam parameters.

In the series of shots corresponding to Figs. 5.2 and 5.3, the average electron density in the injection (acceleration) stage was approximately 6 to 7.5×10^{18} cm^{-3} (4 to 5×10^{18} cm^{-3}). Figures 5.2 (a) - (c) show the full angle divergence of the undeflected beams for three different lengths of the acceleration stage. Divergence of the axial beam remained nearly constant at approximately 20 mrad as the acceleration stage length increased by 4 mm. At the same time, the divergence of the annular

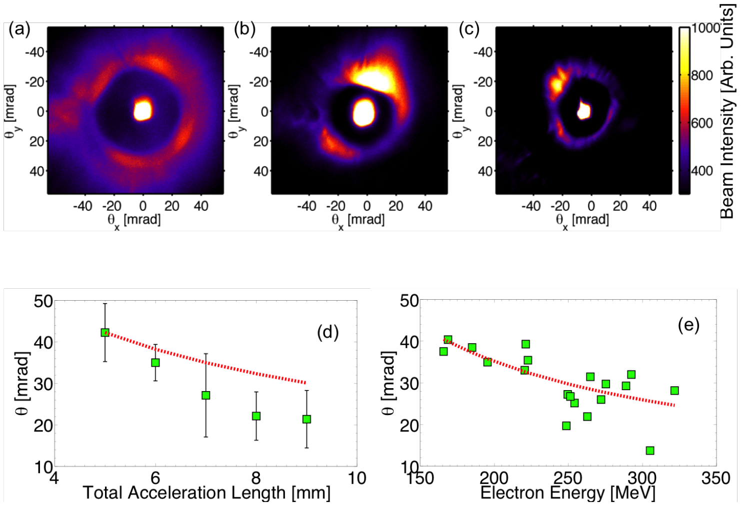

Figure 5.2: Top row: images of the undeflected two-component beams taken at 12 cm from the cell exit. The length of the acceleration stage is (a) 6 mm, (b) 7 mm, and (c) 8 mm. Panels (d) and (e) indicate that the angle of conical emission decreased as either the acceleration length or the energy of the annular beam beam increased. The dashed lines show the momenta scalings described in Ref. [79]. Error bars in (d) denote the standard deviation.

beam decreased by a factor of two [cf. Fig. 5.2 (d)]. In Fig. 5.2 (e), the divergence of the annular beam is observed to decrease as its energy (calculated in the center plane of the annulus along the dispersion direction) increased.

The pulse duration corresponding to Figs. 5.2 (d) and (e) was fixed at 34 fs with an average laser energy of 2.7 J. This gives an estimated dephasing (pump depletion) length of approximately 3.2 (4.4) mm [70]. Thus, both components of the beam have propagated past the dephasing and depletion lengths. In consequence, both components of the beam initially gain energy in a laser-driven wakefield during the first half of the plasma. In the rear half of the plasma, the axial beam can drive a beam-driven wake and is responsible for accelerating the annular component. This necessarily delays dephasing of the annular beam and accelerates the annular beam through the entire plasma [129]. In this case, Figs. 5.2 (d) and 5.2 (e) can be explained by considering the motion of an electron in phase space inside the wakefield bubble. After being trapped at the rear of the bubble, an electron undergoes transverse oscillations that resemble simple harmonic motion with a slowly varying frequency if its acceleration time is long compared with its oscillation period. Since this frequency is slowly varying, there exists an adiabatic invariance that is the conservation of the area enclosed in phase space [78]. By using the Wentzel–Kramers–Brillouin approximation to solve for the equations of motion, one can then deduce that $p_\perp$, the transverse momentum, is proportional to $\gamma^{1/4}$. The electron will also have a longitudinal momentum, $p_{||} \propto \gamma$ [79]. The ratio of the transverse to longitudinal momenta is then proportional to $\gamma^{-3/4}$. Thus, as the electrons are accelerated to higher energies, their angular spread will necessarily decrease. This scaling, shown by the dashed line in Figs. 5.2 (d) and 5.2 (e), corroborates the experimental data. The annular beam also maintains its narrow energy spread after propagating over distances up to three times the dephasing length while the axial beam has a very broad energy distribution since it propagates past its dephasing length. These observations show that the acceleration of the annular beam occurs in the PWFA regime.

5.3.2 Pulse shape effects

Figures 5.3 (a) - (c) demonstrate the effect of the laser pulse parameters on the mean energy and energy spread of the annuli (defined as an average thickness of the annular shell along the dispersion direction). It should be mentioned that stretching the pulse imparts a frequency chirp and can change the pulse shape as well. Measurements of the pulse shape, conducted using a SHG-FROG device, showed that the leading edge for positively chirped pulses is steeper compared with negatively chirped pulses but comparable to that of an optimally compressed pulse. In all presented cases, the chirp is positive.

Several important conclusions can be drawn from these figures. Figure 5.3 (a) shows electron beams dispersed by the dipole magnet. The annular distribution is preserved after passing through the magnet, indicating the monoenergetic nature of

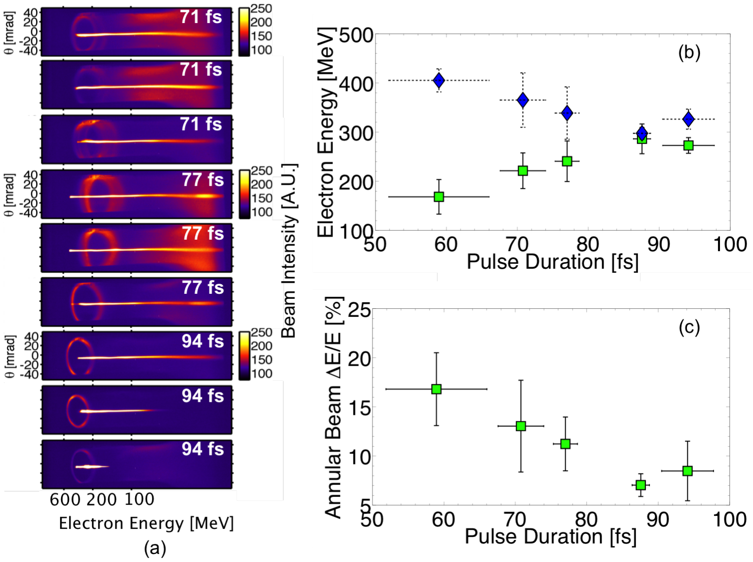

Figure 5.3: (a) ESPEC images show the trend toward production of the most distinct, highest-energy annular beams as the pulse duration increased as well as their monoenergetic nature. (b) Increasing the pulse duration (while simultaneously imparting a positive frequency chirp) boosted the energy of the annular beams (square markers) while decreasing the maximum energy of the axial beam (diamond markers). (c) The energy spread of the annular beams decreased as the pulse duration increased, reaching a minimum of approximately 7%.

these electrons. Furthermore, the energy of the annular beam remains below the maximum energy of the axial beam. Images in Fig. 5.3 (a) also indicate that stretching the pulse trends toward production of the most distinct and highest-energy rings, with a significant drop in the axial signal and annular beam signals. Data shown in Figs. 5.3 (b) and 5.3 (c) support this trend, indicating an increase in the mean energy of the annuli [square markers in Fig. 5.3 (b)]. In effect, as the pulse length increases, the energy of the annular component shifts toward the high-energy end of the axial-beam spectrum, while the energy spread of the annuli reduces [cf. Fig. 5.3 (c)]. When the pulse is stretched from 71 to 94 fs, there is a corresponding percent difference of approximately 28% in the laser power (peak intensity decrease from 1.3 to 0.96×10^{19} W/cm^2). For the lowest density case, the critical power for self-focusing is 7.4 TW and for a pulse duration of 71 (94) fs, $P/P_{cr} = 4.6$ (3.5). Reference [58] showed that injection of electrons in the LWFA regime starts to occur for $P/P_{cr} \gtrsim 3$.

This explains the lower signal in both components of the electron beam produced using the longer pulse duration.

In order for the energy spread of the annular beam to decrease, the injection time (or similarly, the injection cross section) must decrease. It has been shown that the electron injection cross section is inversely proportional to the logarithm of the bubble radius, which is itself proportional to both the ponderomotive force and the radius and number density of the injected beam [78]. Before injection occurs, the bubble radius is proportional to the ponderomotive of the laser. After injection, the force from the beam lengthens the bubble and causes the bubble to expand. The signal reduction in the axial beam (which is injected first) as a function of the pulse duration would result in a smaller bubble size, which should then lead to a subsequent increase in the energy spread of the annular electrons. However, since the injection cross section has a logarithmic dependence on the bubble radius, this effect is rather small.

It is more likely that the pulse duration (or more generally, the pulse shape), along with the density downramp, causes the reduction in both the number and energy spread of the annular electrons. As the laser pulse propagates through the downramp, the decrease in the local density at the front of the pulse increases the plasma wavelength. This increase can result in the trapping of electrons into the cavity provided the expansion rate is fast enough or, equivalently, the expansion region is localized in space. If the cavity then undergoes contraction (e.g., as a result of an increase in the local density as shown in Fig. 5.5 (c) for the two-stage gas cell), the injection can be terminated and both the number and energy spread of the trapped electrons can be limited during this period [56].

In addition, the decrease in energy spread can also be due to the interaction between the annular and axial electron beams. At the shorter pulse durations, more charge is loaded into the axial beam prior to the injection of the annular electrons.

Once the annular electrons are injected, they interact with a stronger space charge force from the axial beam. Thus, even if the injection of the annular electrons is localized in space, the stronger force from the axial beam can cause the energy spread of the oscillating annular electrons to increase throughout their propagation. Thus, both the pulse length and the density downramp can influence the nature of the annular electrons. Beam loading can also limit injection and produce monoenergetic beams. However, since the injected charge decreases for both components of the beam, it is unlikely that the wakefield cavity experiences beam loading.

Although the longest pulse (94 fs) produced the most distinct rings, the rings were observed most consistently at a somewhat shorter (77 fs) pulse duration. Finally, the annular feature was always observed with an axial beam after the latter has propagated past the dephasing length. Attempts at generating the annular beam using longer, positively chirped, pulses were unsuccessful due to an inability to generate the axial beam.

5.3.3 Enhanced betatron emission

The effect of the annular beams on the X-ray flux was quantified by examining the ratio between the integrated counts on the X-ray camera and the integrated electron charge on the ESPEC LANEX. A direct comparison was then made between ESPEC images with and without the annular feature using the corresponding X-ray images. The measurements were taken during the same shot run with a laser energy of 2.4 ± 0.12 J and all other parameters held fixed (except for the pulse duration). As shown in Fig. 5.4 (a), the radiant energy per unit electron charge is higher when the annular beam is present in conjunction with the axial beam (square markers), in contrast to the cases of the axial beam alone (diamond markers). In particular, the radiant energy per unit charge increases by almost an order of magnitude for the pulse duration (94 fs) producing the most distinct, monoenergetic annuli. Figure 5.4

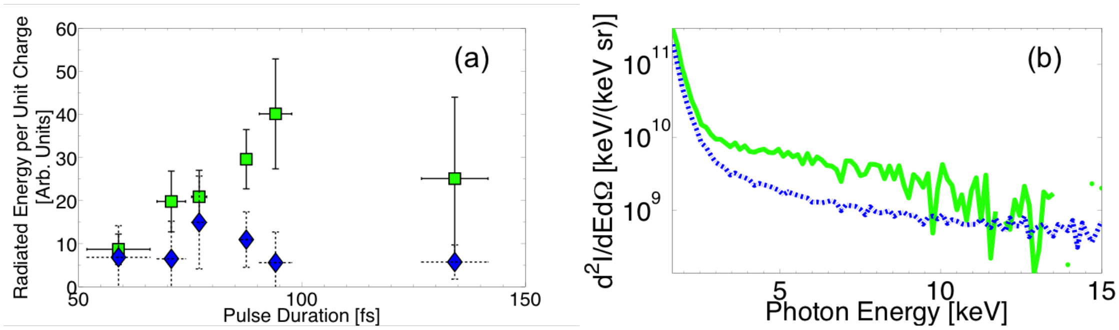

Figure 5.4: (a) Presence of the annuli in conjunction with the axial beam increased the radiant energy per unit charge (square markers) compared with cases of the axial beam alone (diamond markers). At a pulse duration of 94 fs, the most distinct annular beams are responsible for almost an order of magnitude increase in the X-ray yield per unit charge. (b) Single photon spectrum of the axial plus annular (solid) and axial-only (dash dot) beams are shown for the case of a 94 fs pulse duration.

(b) shows the X-ray spectra from both the axial plus annular (solid) and axial-only beams (dash dot) for the case of a 94 fs pulse duration, calculated using the method of single photon counting (see Appendix A). Corrections for predicted double hits based on Poisson statistics were made to the X-ray spectra resulting from the two-component beam due to the significant increase in radiation flux (with the annular beam present, the probability of a double hit ranged from $25 - 35\%$). The axial-only beam spectrum is averaged over a minimum of nine shots, while the axial plus annular beam spectrum is constructed from a single shot.

5.4 Computational modeling

An important aspect of PIC simulations is implementing an accurate density profile. As shown in Figs. 5.5 (a) and (b), the annular beams always appeared in the presence of a density downramp between the first and second stages regardless of the laser power or acceleration length of the gas cell. And, on average, the magnitude of the density drop was around 40% of the first stage value as shown in Fig. 5.5 (c). Thus, a density profile that encompassed these features was used as a starting point for the simulations (Fig. 5.5 (d)). An initial upramp was also introduced into the

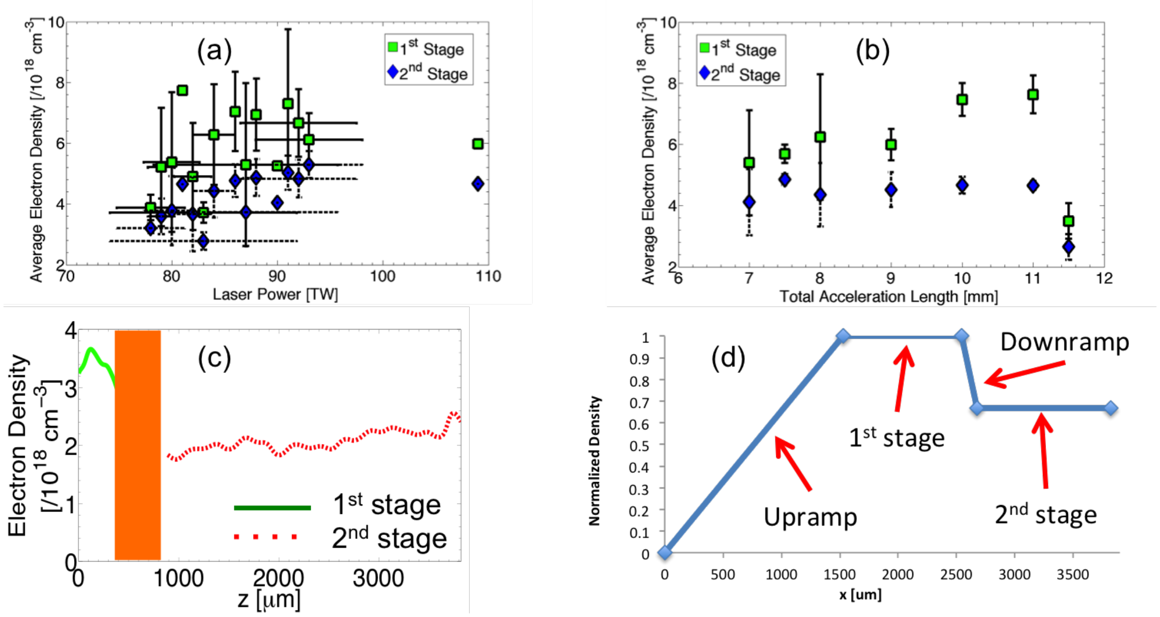

Figure 5.5: (a) Densities in each stage of the two-stage gas cell vs. (a) laser power and (b) acceleration length for instances when the two-component beam was generated. (c) Lineout of the on-axis density inside the gas cell. A slight increase in the density is observed throughout the length of the second stage. The orange box denotes the region between the stages where density measurements could not be made due to the printed plastic walls of the cell obstructing the probe beam. (d) Density profile used for the PIC simulations.

simulation density profile to simulate gas leaking out from the entrance of the cell.

A series of simulations were first conducted in 2D in order to carry out a fast parameter scan involving the: 1) upramp length, 2) overall background density, 3) focal plane, 4) downramp length, and 5) magnitude of the density drop between the stages. In 2D, a distinct group of electrons performing large-amplitude transverse oscillations can be observed in the first bubble of the wakefield. However, artifacts can arise in 2D simulations and thus, 3D simulations are necessary to verify the results. Where practical, the optimal combination of parameters from the 2D trials were used for the 3D simulations. Three-dimensional simulations were conducted by Dr. Chuanfei Dong at the University of Michigan.

5.4.1 Particle-in-Cell simulations and discussion

The experimentally observed increase in the radiant energy in the presence of the annular beam is corroborated by a series of OSIRIS [108] simulations in which a 34 fs linearly polarized Gaussian pulse, with a 0.8 μm carrier wavelength and a waist size $w_0 = 20$ μm ($a_0 = 2.2$, $I \approx 10^{19}$ W/cm^2), is focused at the gas cell entrance. In the simulations, the pure helium plasma begins with a 64 μm-length linear density upramp, followed by the 573 μm plateau (first stage), then a 64 μm linear downramp (transition between the stages), and a 255 μm low-density plateau (second stage). The density in the first stage is 0.175% of critical, while the density in the second stage ranged from 60 to 90% of this value. The set of charge-normalized synchrotron spectra in Fig. 5.6 (a), obtained using recent modifications to the OSIRIS code [71], reveal that the presence of the annular beam can increase the flux for photon energies above 0.5 keV. Since the spectra are normalized with respect to the electron charge, the increase in the flux of higher-energy photons is due to the large-amplitude transverse oscillations of the annular beam inside the wakefield bubble rather than simply an increase in the injected charge. Although this increase is not observed for all downramp profiles, it is not altogether inconsistent with the experimental data. For example, Fig. 5.4 (a) shows that the X-ray enhancement is significant only at longer pulse durations (and positively chirped pulses). At 59 fs, the X-ray yield for the two cases are similar. In addition, Fig. 5.4 (b) shows that the distinction in the spectra becomes more apparent at higher photon energies.

The OSIRIS simulations used a $76 \times 76 \times 86$ μm^3 box (x, y, and z directions) with a longitudinal and transverse grid resolution of 25 and 6.3 cells per laser wavelength. The box clips the beam at $x = y = \pm 1.9 w_0$ and effectively creates a transversely non-Gaussian beam that can change the pattern of nonlinear focusing and seed transient filamentation. The latter sets up transverse density perturbations along the downramp, causing transverse injection of a group of electrons in the shape of an

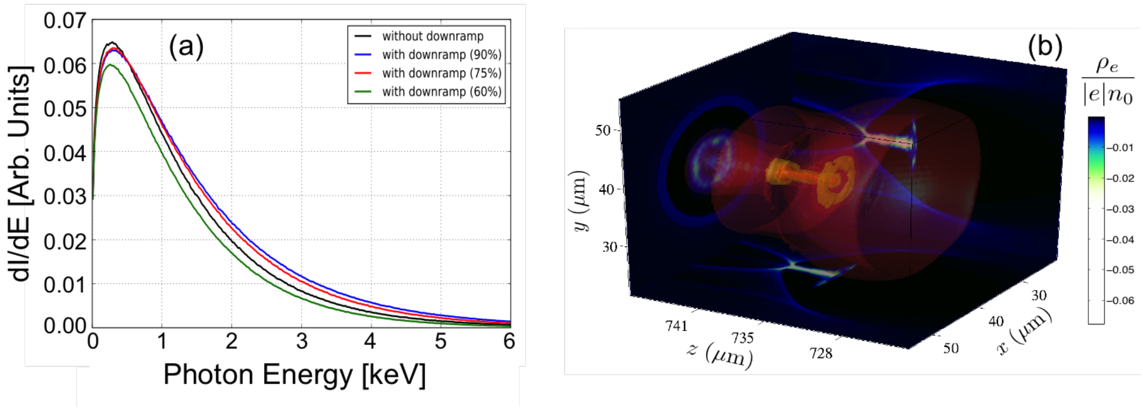

Figure 5.6: (a) Calculated radiation spectra from OSIRIS normalized to electron charge (percentages in the inset indicate the density drop magnitude from the first stage value). All cases involving a downramp produced an annular beam along with an axial beam while the case without a downramp only produced an axial beam. (b) 3D map of charge density in the first bucket of the wakefield after the downramp with both the axial and annular components of the electron beam. Isocontours of the charge density in red, yellow and orange are taken at 0.03, 0.2 and 0.3 of the peak charge density respectively.

annulus; see Fig. 5.6 (b). This injection pattern persists for a range of densities in the second stage. By increasing the box size, and thus returning to a Gaussian beam without filamentation, the annulus is eliminated; this is supported by high-fidelity quasi-cylindrical 3D PIC simulations using CALDER-Circ [130]. CALDER-Circ simulations were conducted by Xavier Davoine at CEA DAM DIF, Bruyères-le-Chaˆtel in France. The mildly non-Gaussian pulse shape is not incompatible with the measured pulse shape and may thus account for the generation of the annuli in a broad parameter range.

Simulations from Ref. [128] show that annulus formation occurs because electrons trapped in the second bubble of the wakefield interacts with a dynamically evolving wake structure. As the wake evolves into the nonlinear blowout regime, the background electrons forms a narrow sheath at the boundaries of the wakefield bubble. For laser-driven wakefields, this boundary is not well defined and it splits. This sheath splitting leads to the formation of a toroidal pocket, located between the first and second bubbles, where electrons can be accelerated and guided off axis.

The field structure inside the pocket is determined by the physical structure of the sheath and the streamlines of electrons that form the boundaries of the pocket. When the electrons in the second bubble catches up with the rear of the first bubble, they are defocused into this region and can stably propagate until they eventually outrun the pocket. It is not immediately clear in Ref. [128] how the annulus electrons can contribute to a significant enhancement in the X-ray flux since they do not undergo transverse oscillations once they are trapped in the toroidal pockets outside of the wakefield bubble. In general, these electrons have to undergo both large-amplitude transverse oscillations and relativistic acceleration in order to produce a significant enhancement in the X-ray flux. The structure of the fields *inside* of the wakefield cavity naturally supports both of these scenarios. Finally, the injection of the electrons into the pocket must terminate at some point in order to produce a monoenergetic annulus. In Ref. [128], a narrow energy spread annulus was produced only when the electrons were propagated to an optimum length. In the experiments conducted here, monoenergetic annuli were produced for acceleration lengths ranging from $5 - 11.5$ mm, using similar plasma densities and laser powers. For a flat density profile such as the one used in the simulations for Ref. [128], there are no obvious mechanisms that can limit the injection of electrons into the second bubble, especially over longer distances. On the other hand, a density downramp is capable of localizing the injection and producing narrow energy spread electrons.

5.5 Conclusion

In conclusion, we demonstrate almost an order of magnitude increase in the radiant energy per unit charge resulting from the localized injection of a group of electrons in the shape of an annulus from a laser wakefield accelerator and subsequent acceleration in a plasma wakefield accelerator. The annular electrons were consistently generated in a two-stage gas cell where a density downramp naturally existed between the stages. These electrons are injected into the wakefield cavity where the effects of the electric fields within the cavity on the annular electrons resulted in almost an order of magnitude enhancement in the X-ray emission. Experimental data indicate that the monoenergetic annular beams are always accompanied by a high-charge collimated axial electron beam, and have energy in the hundreds of MeV. The energy and energy spread of the annular beams were favorably modified using positively chirped, longer duration pulses in combination with the downramp. The monoenergetic nature and phase space distribution of these electrons, along with the associated increase in emitted radiation, can be useful for applications in accelerator science where a high X-ray flux per unit charge is required.

The source size of the betatron emission resulting from the two-component electron beams was not measured. However, the source size is expected to be larger than that resulting from a single axial beam due to the increased oscillations of the annular component. As a result, the peak brightness of the radiation emission is not expected to increase (or decrease) significantly in the presence of typical two-component beams since their contribution to the peak brightness (from the increase in the total radiated photon energy) is dampened by the corresponding increase in the X-ray source size. A net increase in the peak brightness might be still possible for the most monoenergetic and highest energy annular beams (due to their significant contribution to the overall flux) if the oscillations of the annular component is not an order of magnitude higher than the axial component. A measurement of the source size would then yield a direct, quantitative comparison of the peak brightness for the case of a single beam versus the two-component beam.

CHAPTER VI

Enhanced Betatron Emission from Electron Hosing Instability

6.1 Introduction

Instabilities are typically detrimental to the reproducible operation of an accelerator. In the early 1990's, the growth rate of the electron hosing instability was thought to be so rapid that beam transport in an underdense plasma would be problematic at best [131], limiting its use for applications in inertial confinement fusion. This instability leads to spatiotemporally growing oscillations of the beam centroid along its axis of propagation, and can limit the useful acceleration length as well as increasing the beam emittance. The large growth rate from the initial study was due to the assumptions of adiabatic ion-channel formation and beam propagation in an unmagnetized (i.e., nonrelativistic) plasma. Later studies that investigated this instability for beam-driven plasma accelerators showed that the growth rate was not as serious once reduction factors for a non-adiabatic ion-channel formation and magnetized plasmas were taken into account [132, 133].

The electron hosing instability is seeded by the interaction of the electron beam with the laser pulse inside the wakefield cavity when the beam catches up to the pulse and oscillates violently in the laser polarization direction. A similar type of instability can also arise in combination with the electron hosing instability. This type of instability is referred to as ionization hosing [134] and happens when a tilted beam propagates through and ionizes a gas. Due to the beam tilt, the ion cavity is asymmetric with respect to the beam and thus, there is an offset between the cavity and beam axes. This offset then puts an additional force on the beam that can lead to a positive feedback and eventual beam hosing. The ionization hosing instability can also occur for a laser beam propagating through and ionizing an underdense gas [135]. In this case, the dependence of the ionization rate on the laser electric field amplitude [cf. Eq. 2.3] creates transverse modulations of the pulse amplitude, which in turn creates transverse modulations in the electron density. The density modulation can then scatter the laser and reinforce the instability [136, 137].

Although these instabilities are often times unwanted in wakefield experiments, they can be used to increase the radiation emission due to the large-amplitude transverse oscillations of the electron beam resulting from the instabilities. In this Chapter, this novel method for enhancing the X-ray flux is demonstrated experimentally and verified using numerical simulations. This method relies on the electron hosing instability which occurs as the wakefield transitions from the LWFA to the PWFA regime, and requires minimal change to the experimental design and setup. The instability results in high-amplitude transverse oscillations of the electron beam, leading to an increase in the X-ray emission at longer acceleration lengths for fixed electron density. The time-dependent variations in radiation emission are also shown in detail by 3D PIC simulations using a Monte Carlo synchrotron X-ray emission algorithm. Particle-in-cell simulations and analyses of the simulation data were conducted by Dr. Chuanfei Dong at the University of Michigan.

6.2 Experimental setup and procedures

These experiments used a similar setup as that shown in Fig. 4.1. The horizontally polarized laser beam, delivering 1.6 J in a 34 fs pulse (FWHM in intensity), was focused using an $f/20$ off-axis paraboloid to a vacuum beam waist $w_0 = 26$ μm (at $1/e^2$ of peak intensity). On-target peak intensities were thus on the order of 2×10^{19} W/cm^2. A 3D-printed variable-length two-stage gas cell was used as the target. The injection stage was filled with a gas mixture (97.5% He and 2.5% N_2) and the acceleration stage with pure helium. The integrated electron signal and energy spectra were obtained using the ESPEC diagnostic. Although a cross calibration was not done to obtain the electron charge for this experiment, previous measurements have shown that the signal on the LANEX screen is linearly proportional to the charge. Consequently, the signal on the LANEX provides a relative measurement of the charge. The X-ray flux was measured using an Andor iKon-M BR-DD camera that was placed 2.5 m downstream from the interaction region and shielded from the laser light with a 20 μm Be window.

The electron beam signal and energy and the TRPE was measured as a function of the gas cell's acceleration length. The average peak electron density across the entire gas cell was set to 9.5×10^{18} cm^{-3} for all lengths, with a 20% mean variation in the density. The average laser power was $46 \pm 1/3$ TW, giving an estimated dephasing and depletion length of 1 and 1.9 mm, respectively [70].

6.3 Experimental results and discussion

Typical electron beam spectra generated at the different acceleration lengths are shown in Fig. 6.1. Electrons are initially injected and accelerated in the LWFA regime from $1.8 - 2.3$ mm. After propagating past ~ 1.9 mm, the laser pulse undergoes significant pump depletion and the wakefield starts to become beam driven in the

PWFA regime. Throughout the PWFA process (2.8 – 4.8 mm), the peak energy of the initial electron bunch decreases as it loses its energy in order to sustain the wakefield. At the longer lengths (5.3 – 6.8 mm), the acceleration of a secondary group of quasimonoenergetic electrons, due to the PWFA process, is observed. This group is accelerated to higher energies but generally contains less charge than the initial bunch. The maximum electron beam energy is plotted in Fig. 6.2 (a) as a function of length. It is important to point out that Fig. 6.2 (a) shows the maximum energy of the overall electron beam as depicted in Fig. 6.1. In reality, the maximum energy of the electrons injected during the LWFA stage continuously decreases with length while the maximum energy of the electrons injected during the PWFA stage continuously increases. The energy gain of the latter bunch is ultimately limited by energy depletion of the initial bunch.

Since only the acceleration length was changed for this experiment, the increase in X-ray emission must be due to either an increase in the total number of accelerated electrons (i.e., the integrated electron signal) or the onset of the electron hosing instability as discussed in Section 6.1. To disprove the former scenario, the integrated electron signal for electrons with peak energy $E \geq 100$ MeV is plotted as a function of the acceleration length as shown in Fig. 6.2 (b). This cutoff energy was chosen to reflect the fact that the radiation emission is primarily due to the highest energy electrons. From Fig. 6.2 (b), it is observed that the total signal remains approximately the same (within the measured error) for the different acceleration lengths. Thus, any significant increase in the radiation emission cannot simply be attributed to an increase in the number of accelerated electrons in the wakefield. Measurements of the X-ray flux show almost an order of magnitude increase in the TRPE as a function of the acceleration length, albeit with a somewhat constant flux at the longest lengths. The X-ray flux per unit charge also increased with length. These two trends are shown in Figs. 6.3 (a) and (b), respectively.

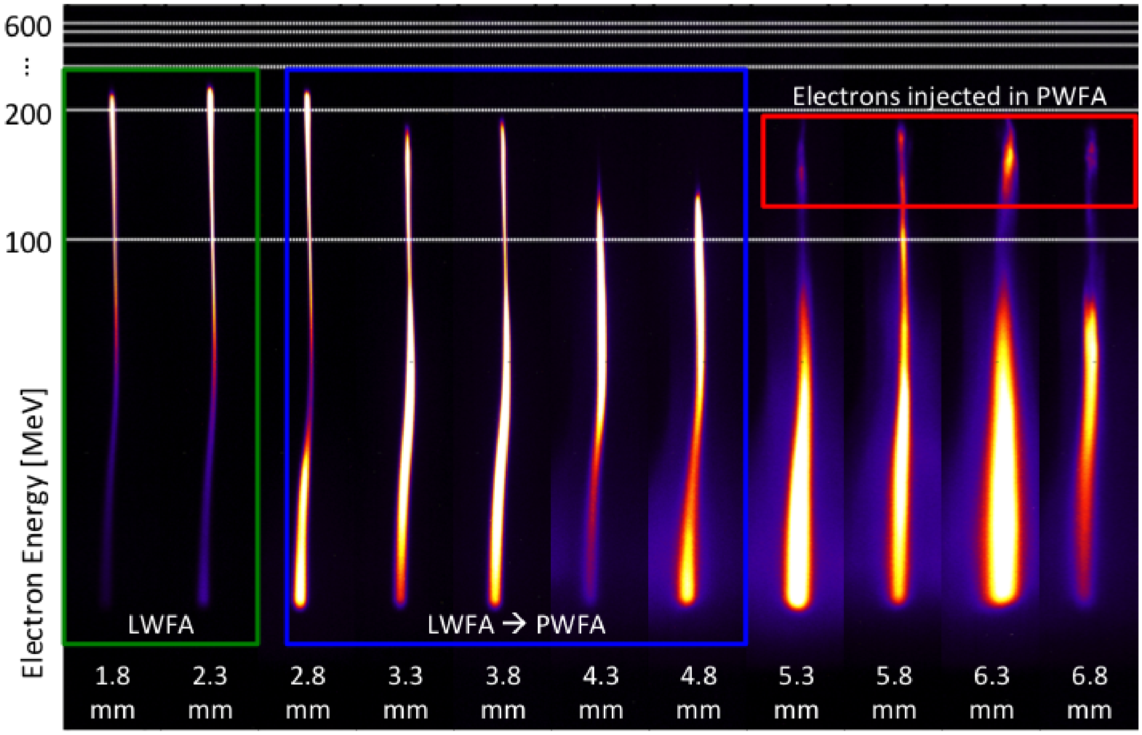

Figure 6.1: Electron beam spectra generated at different acceleration lengths. Electrons are initially injected and accelerated in the LWFA regime (1.8 – 2.3 mm). After propagating past the depletion length (~ 1.9 mm), the wakefield becomes beam driven and the energy of the initial bunch decreases as it drives the wakefield (2.8 – 4.8 mm). In addition, the acceleration of a secondary bunch of electrons is observed at the longer lengths (5.3 – 6.8 mm).

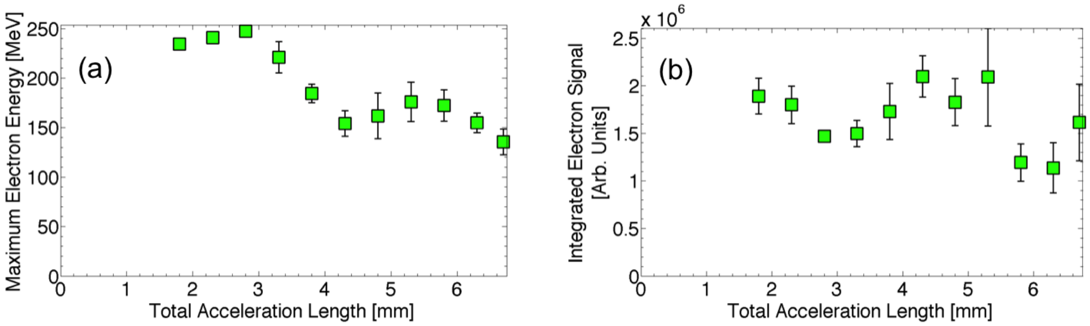

Figure 6.2: (a) The maximum energy of the overall electron beam decreased as a function of the acceleration length. (b) Measurements of the integrated electron signal as a function of the acceleration length for electrons with energy $E \geq 100$ MeV showed that the overall signal remained approximately constant across the different lengths. Error bars denote the standard error of the mean.

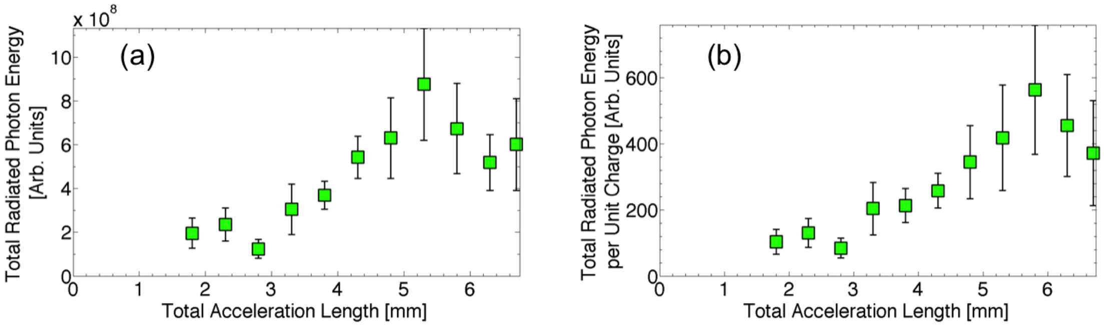

Figure 6.3: Both the (a) TRPE and (b) TRPE per unit charge increased as a function of acceleration length at fixed density.

6.4 Particle-in-Cell simulations and discussion

Particle-in-Cell simulations were conducted to examine the electron acceleration process and better understand the X-ray radiation enhancement. The simulations were conducted with a preionized gas and thus, the ionization hosing instability does not play a significant role. The simulation box was set up in the co-moving frame of the laser, which propagates in the $+z$-direction and is polarized in the y-direction. A 3D charge-density map showing the evolution of the wakefield at different lengths is given in Figs. 6.4 (a) - (c). In Fig. 6.4 (a), the wakefield is in the LWFA regime and electrons are continuously injected into the first bubble. A clear electron beam is formed as seen in the projected images. As this first group of electrons catches up and interacts with the laser pulse front, Fig. 6.4 (b), the electrons undergo increased oscillations in the laser polarization direction. This motion disrupts the spherical shape of the cavity, especially towards the cavity rear. In Fig. 6.4 (c), the 3D charge-density map is excluded to highlight the projected images. In the $y - z$ plane, a noticeable deviation of the electron beam from the cavity axis can be seen. This slight deviation plants the seed for the electron hosing instability. A secondary group of electrons also forms at the rear of the cavity in Fig. 6.4 (c), which is then accelerated by the primary bunch. Between Figs. 6.4 (b) and (c), the wakefield transitions from the LWFA to the PWFA regime.

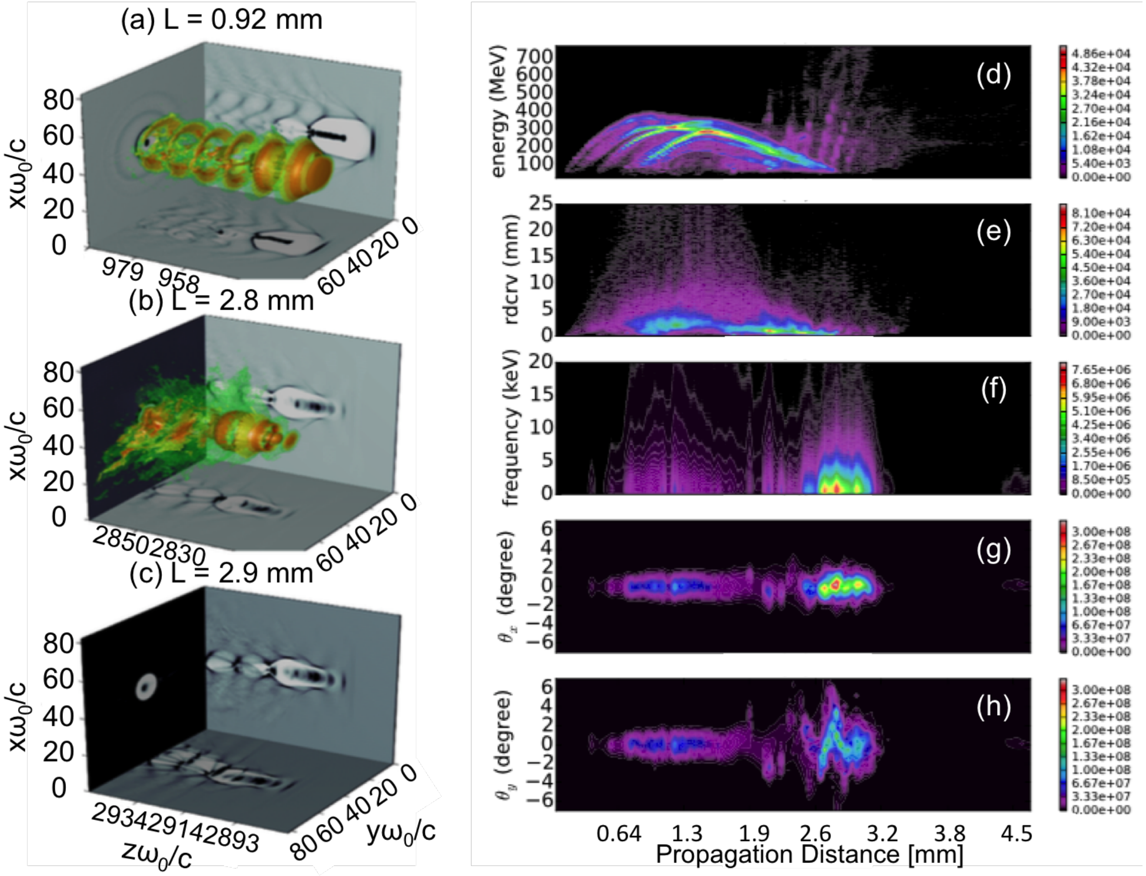

Figure 6.4: (a) - (c) 3D map of charge-density and its projection on the $x - z$ and $y - z$ planes. Number density contour plots as a function of the propagation distance L of the (d) electron energy (for those that contribute to the radiation emission), (e) electron radius of curvature ($rdcrv$), (f) photon frequency (energy), (g) photon emission angle θ_x integrated over θ_y, and (h) photon emission angle θ_y integrated over θ_x. Units are normalized to ω_0, the laser frequency where applicable.

Figures 6.4 (d) - (h) show the time-dependent evolution of the electron energy, electron radius of curvature ($rdcrv$), photon frequency (energy), photon emission angle θ_x integrated over θ_y, and photon emission angle θ_y integrated over θ_x. In Fig. 6.4 (d), a large group of electrons is initially injected and accelerated in the LWFA regime to energies of several hundred MeV. After propagating past the dephasing length (~ 1.3 mm), the electrons start to decelerate. When the electron beam catches up with the laser pulse at $L = 2.8$ mm, the net energy gain of the electrons causes pump depletion and the ponderomotive force of the laser is unable to sustain the wakefield. The wakefield becomes beam driven and is capable of trapping and accelerating a secondary bunch of electrons to almost GeV energies. In Fig. 6.4 (e), the electron radius of curvature is observed to decrease with propagation distance. Initially, the radius of curvature is large and the electrons oscillate with a small amplitude in the undulator regime. As the electrons interact with the laser pulse and the electron hosing instability sets in, the electron oscillations increase with a corresponding decrease in the radius of curvature, signifying radiation emission in the wiggler regime.

In Figs. 6.4 (f) - (h), the TRPE and the integrated angular distributions are plotted as a function of the propagation distance. The TRPE initially increases and decreases in lockstep with the acceleration and deceleration of the electron beam in the LWFA regime. Afterwards, a significant enhancement occurs for the TRPE due to the acceleration of the secondary electron bunch and its interaction with the laser pulse, which leads to the onset of the hosing instability. Figures 6.4 (d) and (f) are consistent with the experimental data shown in Figs. 6.2 (a) and 6.3 (a). Figures 6.4 (g) and (h) show that the angular distributions of the photons is relatively isotropic in the earlier stages of the wakefield evolution and signifies electrons oscillating in the undulator regime. As the simulation progresses, the distribution becomes anisotropic, especially in the θ_y (i.e. laser polarization) direction. The angular deflection in θ_y reaches $\sim \pm 6^\circ$, which is almost three times larger than the deflection in θ_x. The

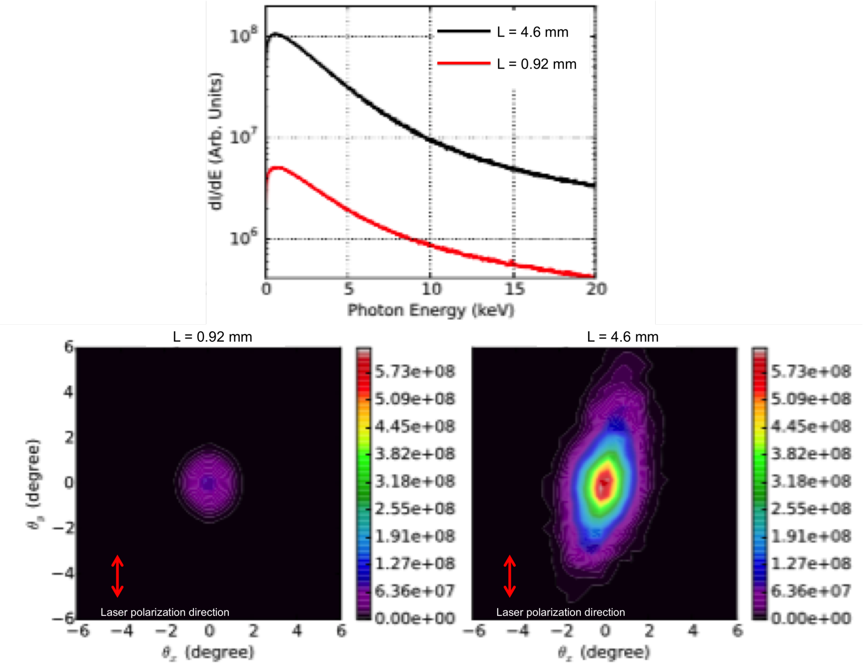

Figure 6.5: Top: Calculated radiation spectra from OSIRIS. Bottom: Angular distribution of radiated photons. The radiation emission for all plots are integrated from $L = 0$ mm to the indicated lengths.

increased angular deflection in the θ_y direction indicates the onset of the electron hosing instability. The corresponding increase in the TRPE and decrease in the electron radius of curvature can be seen in Figs. 6.4 (e) and (f), respectively.

The integrated spectra and angular distributions of the radiated photons are shown in Fig. 6.5. The top row shows the significant increase in the overall photon number after the instability sets in. In the bottom row, the angular profile of the photons evolves from an isotropic distribution (bottom left) to one that is anisotropic in the laser polarization direction (bottom right). Both the anisotropy and high intensity of the photon angular distribution are caused by the electron hosing instability, which causes the electron beam to emit more radiation at each point in its oscillating trajectory.

6.5 Conclusion

In conclusion, an enhancement in the X-ray emission resulting from the electron hosing instability has been demonstrated. Both experimental and 3D PIC simulation results show that the total radiation flux starts to increase shortly after the electron beam catches up with the laser pulse. The interaction of the primary electron beam with the laser pulse leads to the onset of the electron hosing instability and thus significantly enhances the X-ray radiation by almost an order of magnitude. Subsequently, the wakefield driven by the high-energy electron beam can trap and accelerate a secondary group of electrons, during which a transition from an LWFA to a PWFA occurs. Furthermore, this enhancement cannot be attributed to simply an increase in the total number of accelerated charges with length. However, it is possible that the experimentally observed increase in the X-ray flux can be attributed to a combination of the electron and ionization hosing instabilities. The onset of the instability can also be inferred from the simulations by observing the evolution of the emitted photon angular distribution and the electron radius of curvature. The photon angular distribution changes from an approximately isotropic distribution to an anisotropic distribution, where the emitted angle θ_y (in the laser polarized direction) is about three times larger than θ_x, with a corresponding increase in the X-ray source size. At the same time, the electron radius of curvature shows a negative linear correlation with the variation of θ_y due to the transition from the undulator regime to the wiggler regime. The greatly enhanced X-ray radiation can be achieved by taking advantage of a naturally occurring instability in wakefield acceleration and is useful for applications where a high X-ray flux is required with minimal change to experimental design.

CHAPTER VII

Multi-Electron Beam Generation Using Co-Propagating, Parallel Laser Beams

7.1 Introduction

Significant improvements in laser wakefield experiments have been made in the past decade. In 2004, monoenergetic electron beams were generated for the first time [9–11]. Just a couple of years later, several groups demonstrated the generation of GeV-level electron beams using just centimeter length plasmas [138, 139]. The stability and control of the electron injection process have also improved by using various methods such as colliding pulse injection [140], density gradient injection [65], and other mechanisms [93, 141]. These advances demonstrate the feasibility of using plasma-based accelerators for various applications. However, the challenge still remains to increase the total charge of the accelerated electron beam while maintaining the other beam properties. Current experimental results show that the maximum accelerated charge ranges from several tens of pC to $\sim$ 1 nC. For applications in high-energy density physics, beam-driven inertial confinement fusion, and high-flux radiation sources, large charges are beneficial and often, a necessary requirement.

The accelerated charge can be limited by factors such as ionization-induced defocusing, beam loading, and the specific injection method used. In the bubble regime of

LWFA, the number of electrons displaced from a spherical cavity can be approximated as $N = \frac{4}{3}\pi(\lambda_p/2)^3 n_e$, which scales as ${n_e}^{-1/2}$ since the plasma wavelength scales with ${n_e}^{-1/2}$. Thus, more charge can be obtained by lowering the plasma density. However, lowering the density also requires a higher laser power for self-focusing and to trap and accelerate electrons. If the power is readily available, this is the most straightforward way to increase the overall charge. On the other hand, this is often costly to accomplish and impractical after a certain limit.

A unique method of increasing the charge, using a fixed laser energy, is to generate two wakefields that co-propagate simultaneously and independently inject charge into each cavity. In Ref. [142], simulations showed that the total amount and energy of trapped electrons can be increased linearly by using multiparallel laser pulses under certain conditions (discussed later in this Chapter). The increased number of energetic electrons can then lead to an increase in the X-ray emission. Multiple wakefields can be created by using multiple parallel laser beams. There are a number of ways in which these types of beams can be created. For example, the spatial structure of a single beam can naturally evolve from a single spot to a double spot within the Rayleigh length of the focusing optic and create two beams [143]. This method, of course, may not exist for every experimental setup. A more reliable way to generate two beams is to use a coated mirror to change the phase of half of the single beam in the far-field (i.e., before focus) by π radians. This results in two spots at focus of approximately equal energy.

In this Chapter, the charge and energy of electron beams generated using dual focal spots are characterized and compared with those generated using a single focal spot with similar pulse energy and duration. A specially coated mirror is used to create two stable laser spots at focus. The interaction physics are discussed qualitatively from experimental data and quantitatively using simulations conducted by other groups [142, 143].

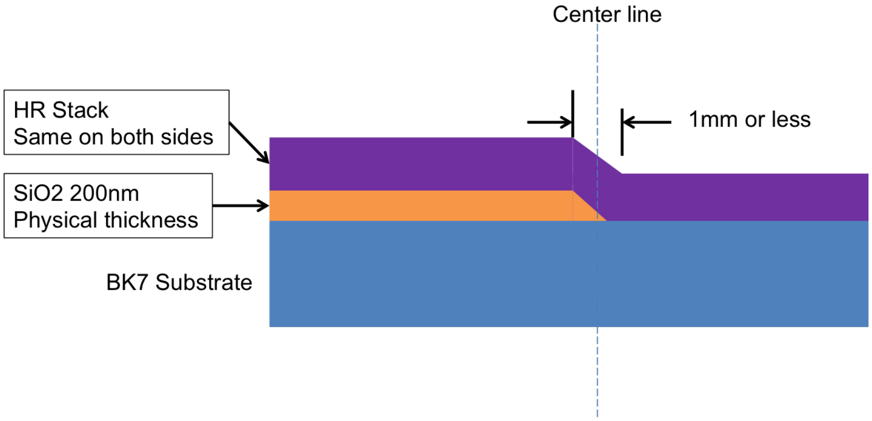

Figure 7.1: Design of π-phase shift mirror. A dielectric (SiO_2) coating, applied to one-half of the mirror, is used to induce a π rad phase shift to half of the beam before the beam is focused. This results in the creation of dual focal spots, as shown in Fig. 7.3, in the vertical direction due to the horizontal orientation of the mirror centerline.

7.2 Experimental setup

The experimental setup mirrors the one shown in Fig. 4.1 except for the placement of a 4-inch π-phase shift mirror inserted at the entrance of the target chamber and an additional 5" silver mirror used to redirect the beam to the usual propagation path. A schematic of the phase shift mirror design is shown in Fig. 7.1. Measurements of the electron beam charge and energy were taken using a 3 mm single stage cell with an average laser power of $43 \pm 4/9$ TW. A 97.5% He and 2.5% N_2 gas mixture was used. The ESPEC diagnostic was used to measure the electron beam energy and charge.

7.2.1 Focal spot characterization

The single and dual focal spots were characterized using an 8-bit Watec CCD camera and an 8-bit Imaging Source Q2 CCD camera. The Watec camera was used to measure the focal spot prior to each experiment and can be operated under vacuum. The Imaging Source camera has a lower noise level and was used to make a more accurate measurement of the focal spot dimensions and energy distribution in

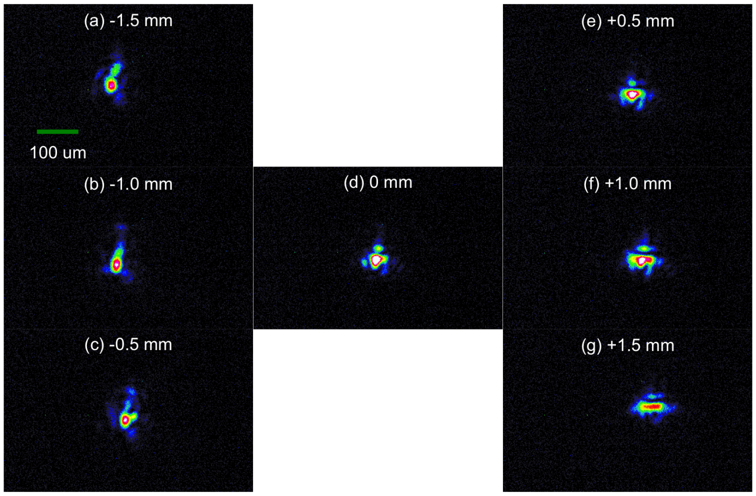

Figure 7.2: Representative images of the energy distribution within a single focal spot throughout the confocal length of the $f/20$ focusing optic. 0 mm denotes the position of best focus. Positive numbers denote positions after focus and vice versa for negative numbers.

air. Figures 7.2 and 7.3 show typical images (obtained from the Watec camera) of the energy distribution for a single and double focal spots, respectively, at various distances within the confocal length of the $f/20$ paraboloid (±1.5 mm). For the dual focal spots, there is an uneven distribution of energy between the spots. As discussed in Section 7.3.1, this leads to the production of dual electron beams that are slightly mismatched in both energy and charge. The same set of filters and imaging system was used to obtain these images.

Analyses of the focal spot images obtained from the Imaging Source camera show that the FWHM of the single and double focal spots is approximately the same at 28 μm. In addition, the total energy in the FWHM of the dual focal spots is similar compared to the energy contained in the FWHM of a single focal spot, although slightly more energy exists in top focal spot compared with the bottom focal spot. The separation between the dual focal spots in the vertical direction is approximately 70 μm.

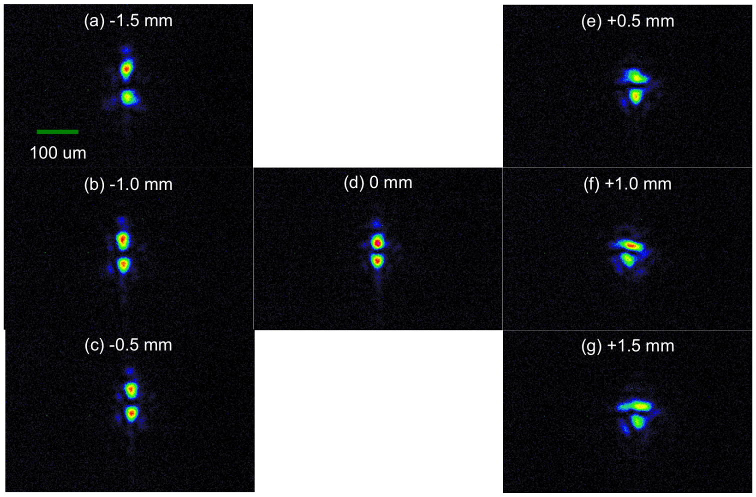

Figure 7.3: Representative images of the energy distribution within dual focal spots, generated using a coated mirror, throughout the confocal length of the $f/20$ focusing optic. A slight asymmetry in the energy distribution (weighted towards the top beam) can be seen for the dual focal spots. 0 mm denotes the position of best focus. Positive numbers denote positions after focus and vice versa for negative numbers.

7.3 Experimental results

7.3.1 Electron beam spectra

The energy spectra of the electron beam(s) generated using either a single or dual focal spots in the 3 mm single stage cell are shown in Fig. 7.4. The spectra in both columns were generated using the same laser parameters, plasma density, and gas mix. In the case of a single electron beam, more charge is loaded into the wakefield bubble and as a result, beam loading occurs earlier [cf. Fig. 7.6]. In the case of dual electron beams, the maximum energy and charge between the two beams are not equal, a direct result of the uneven energy distribution in the two focal spots. In addition, the overall beam divergence (taken as the vertical spread of the beam in the images) is larger for a single beam than for the combined dual beams. The "hour-glass" shaped feature at the low-energy end of the dual beam spectra is mostly likely an artifact resulting from the interaction of lower energy electrons with the fringe fields of the dipole magnet inside the main chamber.

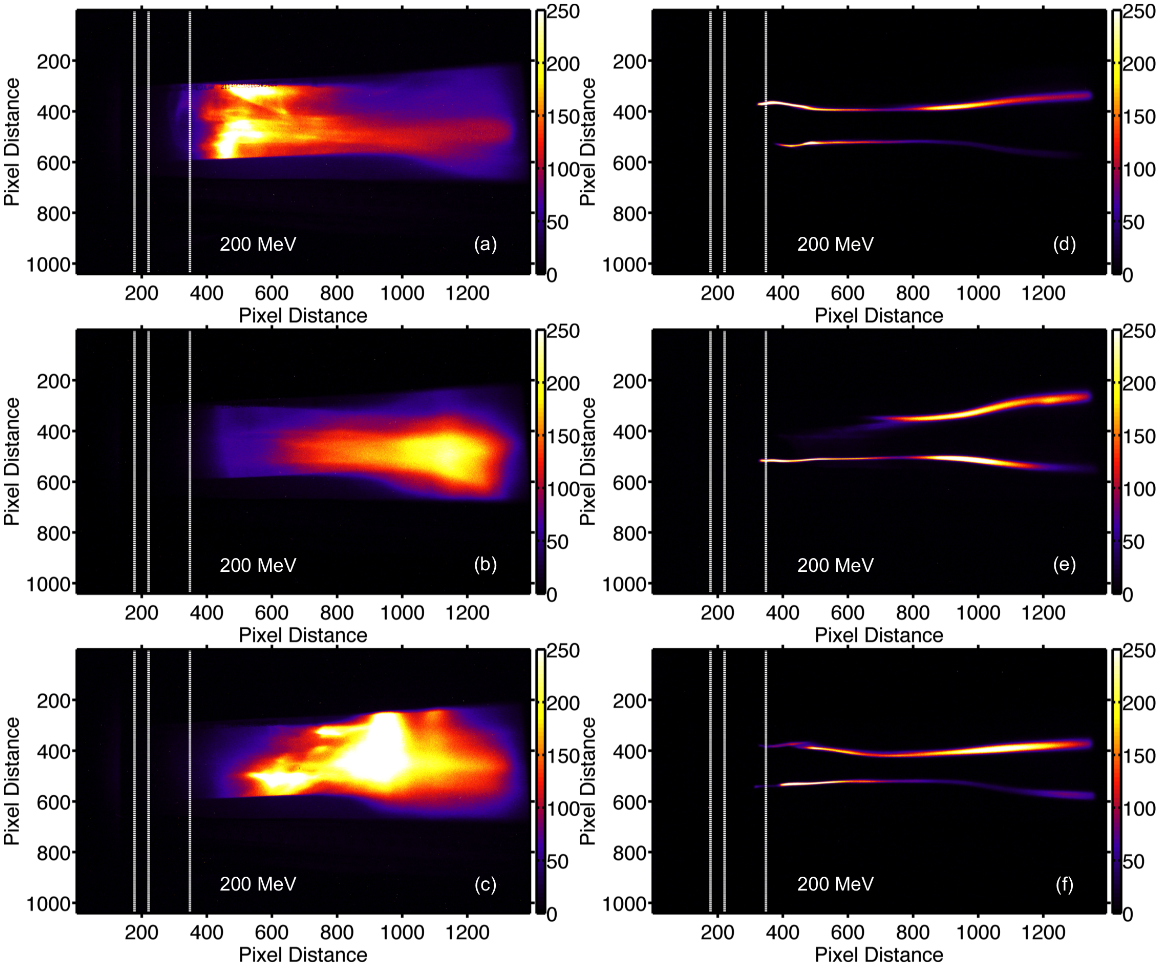

Figure 7.4: (a) - (c) Energy spectra of electron beams generated using a single focal spot. (d) - (f) Energy spectra of electron beams generated using dual focal spots. The beams in both columns were created using the same laser parameters, plasma density, and gas mix. The dotted vertical lines denote the energy levels of the beam in increments of 200 MeV starting from the right in each image.

The energy spectra of the dual electron beams showed some interesting dynamics occurring when a two-stage cell was used to drive the interaction to longer lengths. In Figs. 7.5 (a) - (c), trajectory crossing between the two beams and large amplitude oscillations are observed. In Figs. 7.5 (d) - (f), the formation of a third beam is observed whose energy and charge are comparable to the other two beams. The generation of the third beam only occurred in the two-stage cell due to the longer propagation distance available in the cell ($6.5-11.5$ mm). In addition, the probability of generating the dual beams was significantly enhanced when using the two-stage cell as opposed to the single-stage cell (greater than 50% reproducibility). This suggests that there is an optimal length over which the two wakefields can fully develop and trap charge. For the laser pulse parameters and densities used when operating with the two-stage cell, dual beams were consistently generated for all lengths. The formation of the triple beams was less consistent and is most likely due to the more stringent requirements for the formation of a third wakefield required to generate the third beam. This is discussed in Section 7.4.

7.3.2 Charge and energy comparisons

As mentioned earlier, the presence of dual electron beams appeared to delay the onset of beam loading in the wakefield cavities. Figures 7.6 (a) and (b) show the integrated electron signal for the 2.5% N_2 gas mixture and pure He gas, respectively, as a function of the electron density. In order to access a larger set of electron beam spectra, all spectra images obtained using the pi phase shift mirror were included for the case of dual beam generation. This data set is designated as “With Pi Mirror” in Figs. 7.6 (a) and (b). Similarly, all spectra images obtained without the pi phase shift mirror (i.e., images were only a single electron beam was generated) are designated as “No Pi Mirror” in the two figures. Inspection of the square and circular data points in Figs. 7.6 (a) and (b) show an increase in the density which produced the highest

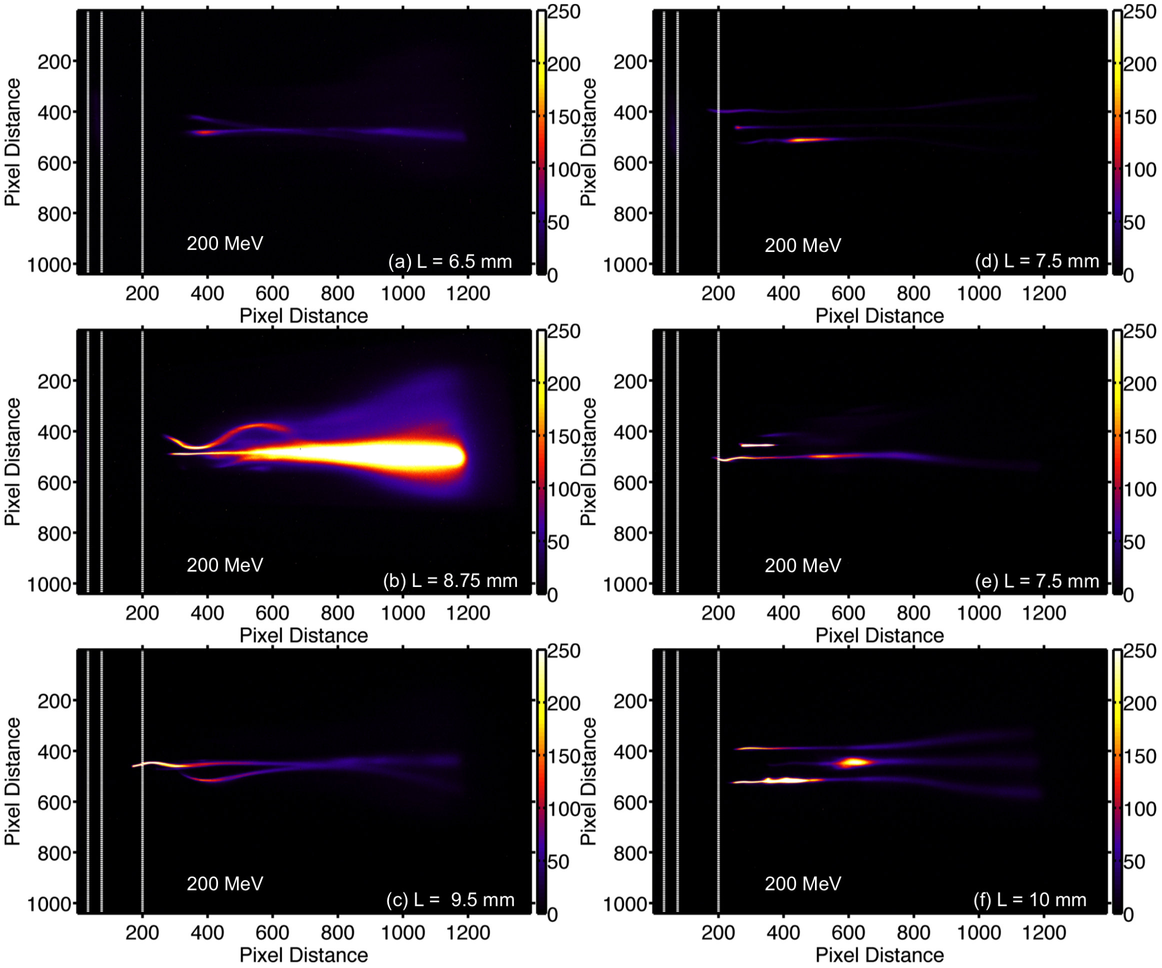

Figure 7.5: (a) - (c) Energy spectra of dual electron beams. Interaction between the electron beams led to trajectory crossing between the beams and increased transverse oscillations. (d) - (f) Injection and acceleration of a third electron beam occurs due to the coherent superposition between the diffracted parts of the original two focal spots as discussed in detail in Section 7.4. L is the total length over which the beam(s) in the two-stage cell are accelerated. The dotted vertical lines denote the energy levels of the beam in increments of 200 MeV starting from the right in each image.

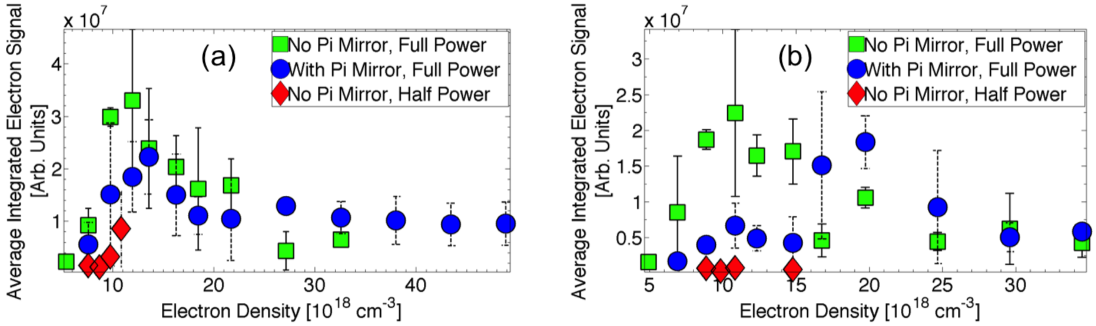

Figure 7.6: Integrated electron signal versus density for beams generated using the (a) gas mixture (b) pure He gas. The π-phase shift mirror was used to generated dual electron beams.

amount of electron signal. This effect is more pronounced for the pure He gas.

A null test was also conducted to see if electron beams with approximately half charge could be generated using a single focal spot at half power or equivalently, at half energy since the pulse duration was fixed. The energy spectra for these shots are represented by the diamond data points in Figs. 7.6 (a) and (b) for the two gases. Overall, no significant injection was observed for the same densities at half power. This trend suggests that injection of charge using dual focal spots is likely a result of interactions between the two wakefields. Efforts at producing electron beams at higher densities at half power were not successful and thus, are not shown in the figures for clarity.

The integrated electron signal on the ESPEC LANEX was characterized as a function of the electron density to determine if an increase in the total charge occurred in the case of distinct dual beams compared with a single beam. Figures 7.7 (a) and (b) show the integrated signal from the single and dual beams generated using the 2.5% N_2 gas mixture and pure He gas, respectively. The circular data points consists of images where two distinguishable electron beams were observed. Lower densities were below the injection threshold and thus didn't produce any beams, while higher densities failed to produce distinct dual beams. It is clear that the charge did not increase for the case of dual beams. In general, the charge contained in the dual

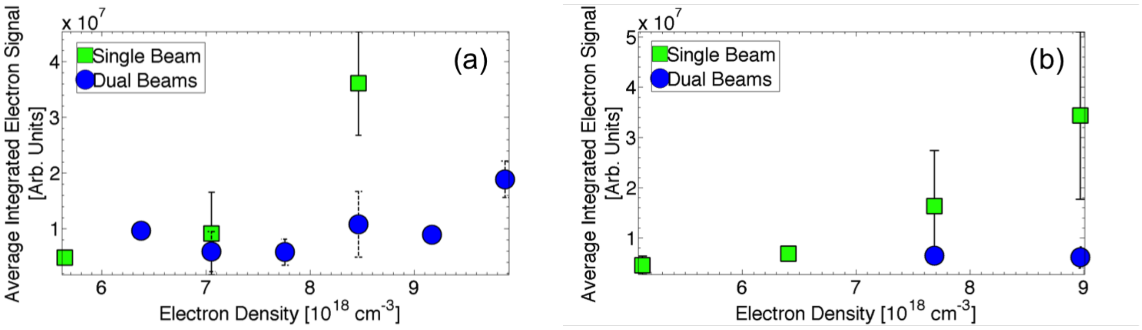

Figure 7.7: Integrated electron signal comparison between single and dual electron beams for the (a) 2.5% N_2 gas mixture and (b) pure He gas.

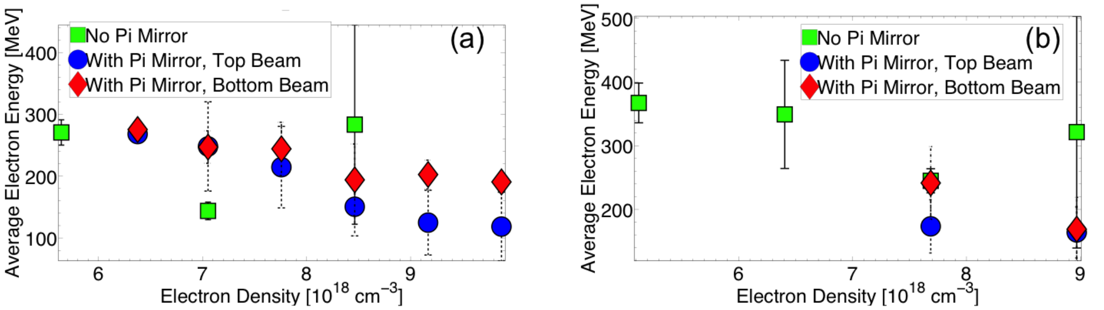

Figure 7.8: Maximum electron energy versus density for beams generated using the (a) mixed and (b) pure He gases. The designation of "top" and "bottom" correspond to the orientation of the beams on the ESPEC LANEX.

beams is less than (or, at best, equal to) the charge contained in a single beam.

The maximum energy of the electron beams, defined as the highest energy with signal, is plotted in Fig. 7.8 for beams generated using the two gas types. For a given density, the energy of the single beam is generally higher than that of either dual beams. The energies of the beams also decreased with increasing density as would be expected since both the dephasing and depletion lengths decrease with density. The slight asymmetry in the energy between the top and bottom beams for the dual beams is attributed to the uneven energy distribution in the two focal spots.

7.4 Discussion

Particle-in-Cell simulations are required to better understand the interaction between the two wakefields and the role of the separation distance between the spots in generating dual and triple electron beams. Such simulations were conducted in Refs. [142, 143] and a discussion on those simulations is presented in this section.

In Ref. [142], two linearly polarized parallel pulses, separated by a distance d_L, were propagated into a uniform plasma. The polarization of the two pulses were perpendicular to one another so that the total intensity was simply the sum of the two pulses. Each pulse drives its own wakefield and electrons are capable of being injected into the accelerating field of each wakefield bubble. Figure 7.9 shows a schematic of the two pulse setup. When the two pulses were too close to one another, they expelled electrons as a single, larger pulse and only one bubble is formed since the pulses propagate and self-focus as a unit. If a sufficient separation initially existed between the two pulses, then two bubbles are formed with a shared electron sheath boundary between them. After the pulses have self-focused, the bubbles remain clearly separated and trap and accelerate electrons independently. These scenarios are shown in Fig. 7.10. Figures 7.10 (a) - (c) show the wakefield evolution at three different time steps for pulses separated by $d_L = 0.5w$, where w is the FWHM of the Gaussian pulse and d_L is the separation distance between the pulses. Figures 7.10 (d) - (f) show the wakefield evolution for pulses separated by $d_L = 0.75w$ at the same time steps. For $d_L = 0.75w$, two distinct wakefields are generated along with the acceleration of two separate electron beams. The charge in this case can be almost double that in the single beam case for the same laser energy in both scenarios. It is worth pointing out that the trapping cross section depends on the dimensions of the bubble [78]. In these simulations, the overall size of the two bubbles is only slightly larger than the size of the single bubble by approximately 30% yet significantly more charge can be injected. Thus, and perhaps not so obvious, the total charge not only

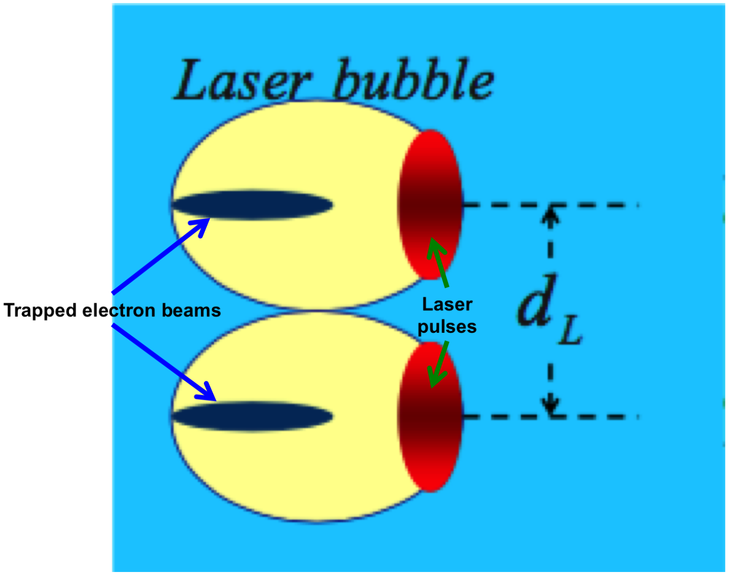

Figure 7.9: Schematic showing electron bunch acceleration in two wakefields by using dual laser pulses separated in the transverse direction by a distance d_L. Figure adapted from Ref. [142] with the permission of AIP Publishing.

depends on the bubble dimensions but also on the number of injection points into the accelerating wakefield cavities. The accelerating gradient inside the two bubbles is similar to the gradient for the single bubble case, leading to approximately equal electron energies between these cases.

Simulations from Ref. [143] showed that the coherent superposition of the diffracted parts of the two focal spots can create a third spot between the two that is intense enough to drive a third wakefield. The optimal separation between the two spots was found to be 30 μm for 10 μm spots (at $1/e^2$ in intensity). This scenario is shown in Fig. 7.11. At the earlier time, two distinct pulses and wakefields can be seen with electrons being accelerated inside the bubbles. The superposition of the electric fields of the two spots starts to form a third spot. At the later time, the third focal spot is fully formed and drives its own wakefield. When the separation was enlarged to 40 μm, the superposition of the diffracted parts was not intense enough to form a third bubble and the two pulses propagated independently instead. A smaller separation of 20 μm yielded a single pulse, similar to the case depicted in Figs. 7.10 (a) -

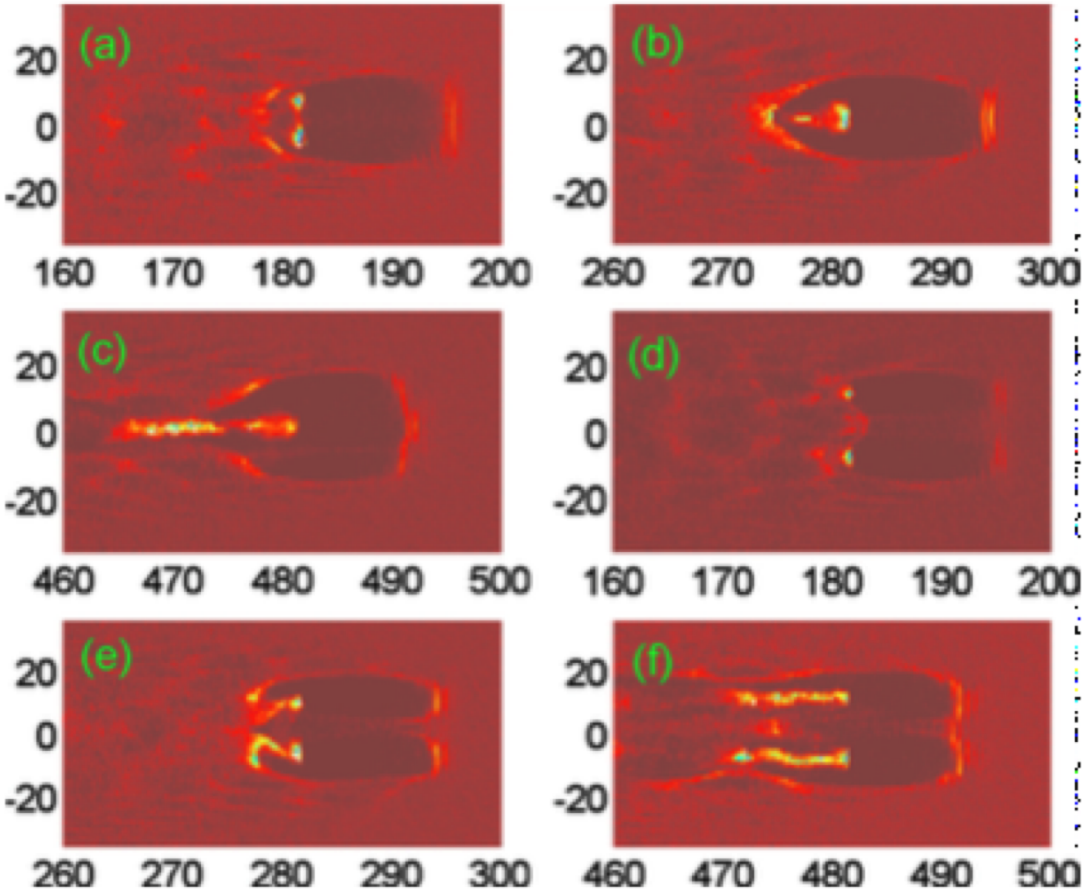

Figure 7.10: Charge-density countour maps at $t = 0.67$ ps [(a) and (d)], $t = 1.00$ ps [(b) and (e)], and $t = 1.67$ ps [(c) and (f)]. (a)-(c) are for $d_L = 0.5w$ and (d)-(f) are for $d_L = 0.75w$. The transverse and longitudinal coordinates represent the directions parallel and perpendicular to the laser propagating direction, respectively. Distances are given in microns. Figure from Ref. [142] with the permission of AIP Publishing.

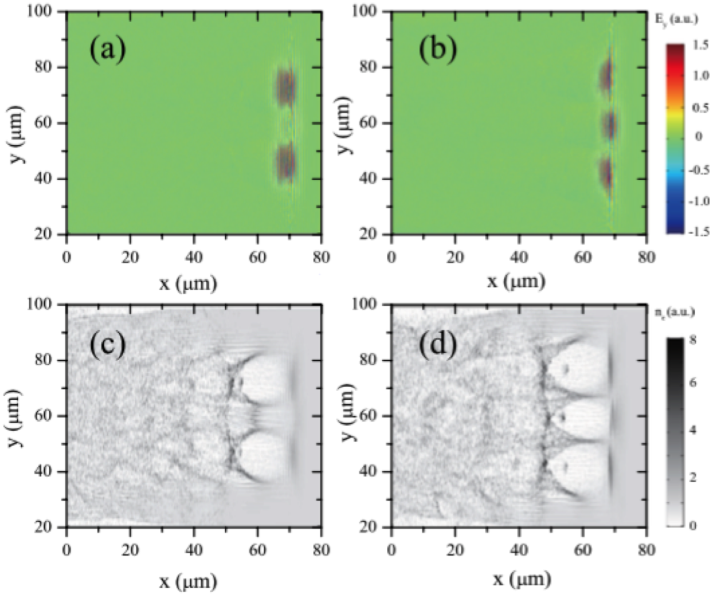

Figure 7.11: Evolution of the laser field (top row) and charge-density distribution (bottom row) for t = 8.5 ps (a) and (c) and t = 14.9 ps (b) and (d), respectively. Figure from Ref. [143] with the permission of AIP Publishing.

(c). These scenarios are depicted in Fig. 7.12.

The simulations from both groups and the experimental data Ref. [143] showed an increase in the number of injected electrons when multiple beams were generated. In Ref. [143], the dual electron beams were generated in an uncontrolled manner since the two focal spots evolved naturally over the Rayleigh range of their focusing optic. The charge increase observed in their experimental data was attributed to the increase of laser energy contained within the FWHM of the dual focal spots compared to the single spot (500 vs. 300 mJ). The total energy in the FWHM of the dual spots generated using the π-phase shift mirror was approximately the same as that contained in the single focal spot. Thus, an increase in charge was not observed. The ratio of the separation between focal spots to the spot size for this experiment is approximately 2.3 which is smaller than the corresponding ratio, 3, from the simulations in Ref. [143]. This could perhaps explain the inconsistency in generating three electron beams at the longer lengths.

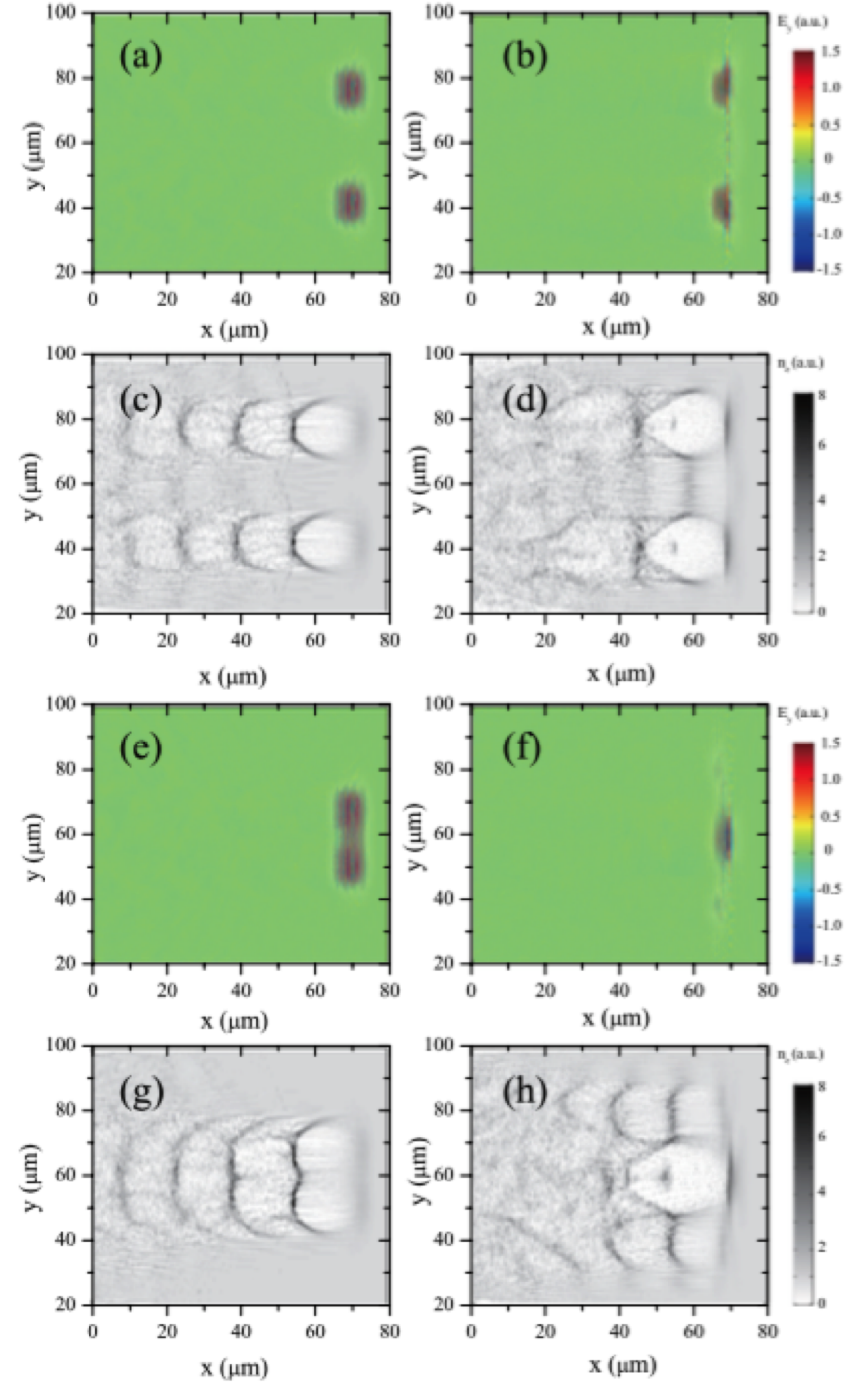

Figure 7.12: Differences in the overall wakefield evolution due to the initial focal spot separation distance. (a) - (d) A separation of 40 μm leads to the propagation of two independent wakefields. (e) - (h) A separation of 20 μm results in the formation of a single focal spot and thus, a single wakefield. (a), (b), (e), and (f) represents the electric fields of the laser pulses and (c), (d), (g), and (g) represents the charge-density distributions of the electrons. Figure from Ref. [143] with the permission of AIP Publishing.

7.5 Conclusion

It is interesting to note that a charge increase was not observed in the presence of dual beams for this experiment. Pulse energy/power differences between this experiment and the ones in Refs. [142, 143] cannot account for this fact since Ref. [143] actually used a much lower pulse energy and power. A more likely explanation is the fact that the total energy contained within the two focal spots did not increase compared with the energy contained in the FWHM of a single focal spot. Yet, this does not explain why the dual beams contained only 50% of the charge instead of the same charge as a single beam. It is clear that both the spot separation and energy distribution play an important role in generating the beams and increasing the total charge. To control both of these factors, a deformable mirror can be used to precisely manipulate the wavefront of the laser beam in order to obtain the optimal separation and maximum energy contained in the FWHM. Once these parameters are optimized, the corresponding radiation emission should also increase accordingly provided that the charge and peak energy of the electron beams in each wakefield cavity is comparable to the charge and energy of an electron beam in a single wakefield cavity. By fine-tuning the focal spot parameters (and hence, the electron beam parameters), one could also manipulate the X-ray spectrum and beam divergence. In theory, these simulations also suggest that an unlimited amount of charge can be injected provided the plasma is large enough to accommodate the number of pulses. However, the power contained in each pulse still has to be greater than the relativistic self-focusing power. Since the pulse energy is evenly divided between the pulses, a natural limitation to this scheme is the total pulse energy available for a given system.

The number of wakefields can be precisely controlled by using the π-phase shift mirror. The null test conducted for this experiment showed that interaction between the wakefields can cause injection to occur for situations in which a single wakefield shows no significant injection. The combination of two such mirrors would result in four focal spots, leading to the simultaneous generation of four wakefields. The region between these wakefields can potentially serve as an accelerating structure for positrons.

CHAPTER VIII

Conclusions

8.1 Summary

This thesis presents novel methods of controlling the injection and acceleration of electron beams by using a combination of methods involving the laser pulse parameters, plasma density profile, and the electron hosing instability. These methods led to either the generation of quasimonoenergetic, GeV-level electron beams, an enhancement in the radiation emission, or both.

The first set of experiments demonstrated the dependency of the electron beam and X-ray properties on the laser pulse parameters for a typical Ti:Sapphire CPA laser system. Altering the pulse properties can affect the electron injection process which in turn directly affects the emitted radiation. Positively chirped pulses with a fast-rising leading edge led to an increase in the electron charge compared with negatively chirped pulses with a slow-rising leading edge but produced electron beams with lower peak energies. The X-ray flux trend matched that of the integrated electron charge. The emitted radiation also scaled linearly with the electron charge over a threefold change in the electron density, independent of the laser pulse characteristics. X-ray spectra showed that the 2.5% mixed gas produced more photons than the pure He gas and had a smaller spread in the spectra due to ionization injection. In all cases, however, optimal pulse characteristics generally produced the highest number and highest peak energy of injected electrons and photons.

In the second experiment, localized injection of a group of electrons using a density downramp led to the creation of a two-component electron beam. The beam is initially injected in a laser wakefield accelerator and subsequently accelerated in a plasma wakefield accelerator. The annular portion of the beam produced almost an order of magnitude increase in the X-ray flux per unit charge. Experimental data indicates that the monoenergetic annular beams are always accompanied by a high-charge collimated axial electron beam, and have energies in the hundreds of MeV. The energy and energy spread of the annular beams were favorably modified using positively chirped, longer duration pulses. The monoenergetic nature and phase space distribution of these electrons, along with the associated increase in emitted radiation, can be useful for applications in accelerator science where a high X-ray flux per unit charge is required.

The third experiment used the electron hosing instability to increase the radiation emission in a laser wakefield accelerator for a fixed electron density. An electron bunch is initially injected in the LWFA regime and accelerated to high energies. After propagating past the pump depletion length, the wakefield transitions into the PWFA regime and a secondary bunch is then trapped and accelerated. The interaction of the primary electron beam with the laser pulse led to an order of magnitude increase in the X-ray emission, with an increase in the photon divergence in the laser polarization direction. Since the only requirement for this enhancement is propagating the electrons to longer lengths, this method offers a simple way to effectively achieve a high X-ray flux with minimal changes to experimental design and setup.

The final set of experiments showcased a unique way of generating co-propagating wakefields by using a π-phase shift mirror to create two focal spots. The wakefields are capable of independently injecting and accelerating electrons. These experiments demonstrated the ability to consistently generate dual electron beams and the appearance of triple beams at longer interaction lengths using just the two focal spots. The total charge contained in the multiple beams was approximately 50% of the charge contained in a single beam and their maximum energy was less than that of a single beam. Simulations conducted by other groups demonstrated the importance of the initial separation of the two spots in generating the multiple beams. In addition, the energy contained within the FWHM of the spots is essential in providing a net increase in the total charge when two beams are present.

8.2 Future work and outlook

Compared with conventional accelerators, laser wakefield accelerators offer the advantage of high accelerating gradient ($\geq$ 100 GeV/m), ultrashort beam duration ($\sim$fs), beam synchronization with the laser pulse, and the natural generation of high quality X-rays whose properties are linked with those of the electron beam. However, wakefield accelerators also suffer from beams with large energy spreads and issues related to existing laser technologies such as relatively poor conversion efficiencies, shot-to-shot variability, and low operating rates. The work presented here have aimed to address some of these issues and ways to move forward are discussed here.

Although the optimal pulse duration still produced the highest electron charge and energy, the asymmetry in the electron properties between positively and negatively chirped pulses signify that the pulse shape and frequency chirp can have noticeable effects on the injection and acceleration process. These effects are evident even with the relatively small bandwidth and differences in pulse shape from the HERCULES laser system. With a sufficiently large bandwidth, it should be possible to significantly change the pulse length and achieve a net increase in the charge (energy) of the accelerated beam using positively (negatively) chirped pulses compared with the shortest pulse duration. In addition, pulse shaping methods can be used to optimize the leading edge slope of the pulse. Finding technologically and experimentally feasible methods of adjusting the pulse bandwidth and shape is an important design factor for future table-top petawatt-class systems.

The generation of the annular electron beams is a promising source of high flux radiation emission. Under optimal conditions, these beams were generated 40% of the time. Although experimental data point out several key factors associated with the appearance of these annular beams, the precise physics concerning the formation and acceleration of the annuli are still not fully understood. To date, the common thread running through all simulations and experimental data concerning these rings is the dynamic evolution of the laser pulse and the plasma wakefield. For example, in Ref. [128], self-focusing increased the laser a_0 and allowed the laser spot size to evolve to a matched spot size such that the wakefield progressed in the bubble regime and sheath splitting occured over a wide range of parameters. The sheath splitting forms the toroidal pockets that contains and accelerates the annular electrons. In the experiments conducted here, the presence of a density downramp played an important role in generating the annular beams. The downramp (in the direction of laser propagation) elongates the wakefield cavity and decreases the wake phase velocity, thus reducing the trapping condition. Simulations and experimental data showed that both the magnitude of the density drop and the length of the downramp plays an important role in the creation of the annulus. The experiments also showed that the annular component is accelerated in the PWFA regime by the axial beam and is not dephased. Instead, it maintains its monoenergetic nature after the axial beam has propagated significantly past the dephasing and depletion lengths. The production of increasingly monoenergetic annluar beam with longer duration, positively chirped pulses also requires further study. The combined effects of pulse duration, frequency chirp, and density downramp on the injection process have not been previously studied.

It is also interesting to note that an annular electron beam, without an axial component, can be created using Laguerre-Gaussian pulses [144, 145]. The hollow region between the annular beam electrons is suitable for positron beam collimation and acceleration and can be used for a wakefield-based electron-positron collider. Current wakefield-based schemes for positron acceleration involves either an electron or positron beam driver. These schemes tend to produce large energy spread and emittance in the positron beam and low accelerating fields [146, 147]. Using the annular beams, the accelerating field for positrons is proportional to the total charge in the annular beam while the length of the acceleration region (i.e., one plasma wavelength) remains approximately the same. Studies have shown that this scheme offers a linear scaling of the accelerating electric field with the charge in the driver beam without dramatically reducing the acceleration region [148].

As a final remark, it should be possible to use two π-phase shift mirrors to create four focal spots and drive four simultaneous wakefields. Under these circumstances, the region between the wakefields can also serve as a positron accelerator. This requires at least twice the energy used for the experiments in Chapter VII. It would be interesting to see if dual annular electron beams can be generated as well under these conditions. With proper photon engineering (e.g., using adaptive optics), one can then tailor the parameters of the laser spots to maximize the resulting radiation emission.

APPENDICES

APPENDIX A

Single Photon Counting

Charged coupled device cameras can be used as a dispersionless spectrometer to measure high-energy radiation in the multi-keV range when operated in the single photon counting (SPC) regime. They offer many benefits such as statistical assurance through multiple data acquisitions, the ability to analyze data in-situ, operation in both single and multi-shot modes, a near Fano-limited energy resolution, and low noise level. In the SPC regime, the probability of the detector recording n photons is governed by Poisson statistics,

$$P(n) = \frac{\lambda^k e^{-\lambda}}{k!} \tag{A.1}$$

where λ is the average signal value per pixel on the camera sensor. This probability is the first moment of the distribution $\lambda = \sum_{n=0}^{\infty} nP(n)$. The probability of a double-hit, $P(2)$, occurring relative to a single-hit, $P(1)$, is then $P(2)/P(1) = \lambda/2$.

In the typical SPC operation, the camera sensor is exposed to photons over a time period relevant to the radiation emission timescale. When the photons strike the sensor and deposit their energy, the analog-to-digital converter unit will produce a signal proportional to the incident photon energy. The radiation spectrum can then be calculated by computing a pulse height histogram of the accumulated signal on the camera. In reality, the measurement is complicated by two main factors which can skew the reconstructed spectrum. First, more than one photon can land on a pixel (within the response time of the detector) and deposit its energy solely in that pixel. Typically, the likelihood for an $n > 2$ event is largely reduced compared to the case of an $n = 2$ event. Thus, only the latter scenario is considered in LWFA experiments. Secondly, it is also possible for the signal from a single high-energy photon to spread over neighboring pixels. To minimize these effects, one can either use filters to reduce the X-ray signal or place the detector at a sufficient distance from the interaction region so that the number of activated pixels on the sensor is small compared to the total number of pixels, i.e., $\lambda \ll N^2_{\text{pixels}}$, where N^2_{pixels} is the total number of pixels for a square sensor. For the detection of low-energy photons, filters are not preferred since they can significantly attenuate the X-ray signal.

For the betatron spectra measurements made in this thesis, the CCD camera was placed 2.5 m away from the interaction region and a low-Z material filter was used to protect the camera sensor from the laser light (either Be or Al). This ensured that the chip occupancy (i.e., λ) remained at a sufficiently low level. For cases where a high X-ray signal cannot be avoided, a Monte-Carlo algorithm was developed that is capable of correcting for double-hits for a chip occupancy below 30% or equivalently, a double-hit probability less than 15%. The camera was cooled to -40° C using its built-in thermo-electric cooling platform in order to reduce background noise from cosmic radiation. An energy calibration was also conducted using an Fe-55 source to fine tune the A/D conversion parameters and calculate the inherent resolution of the camera [cf. Fig. 3.12 (b)]. Figure A.1 shows an example of a betatron spectrum corrected for double-hits using the Monte-Carlo algorithm. The calculated spectrum represents a simulated betatron spectrum with double-hits occurring on the sensor. Double-hits manifests themselves in the spectrum by reducing the number of low-energy photons and transferring the energy of these photons to the high-energy end of the spectrum.

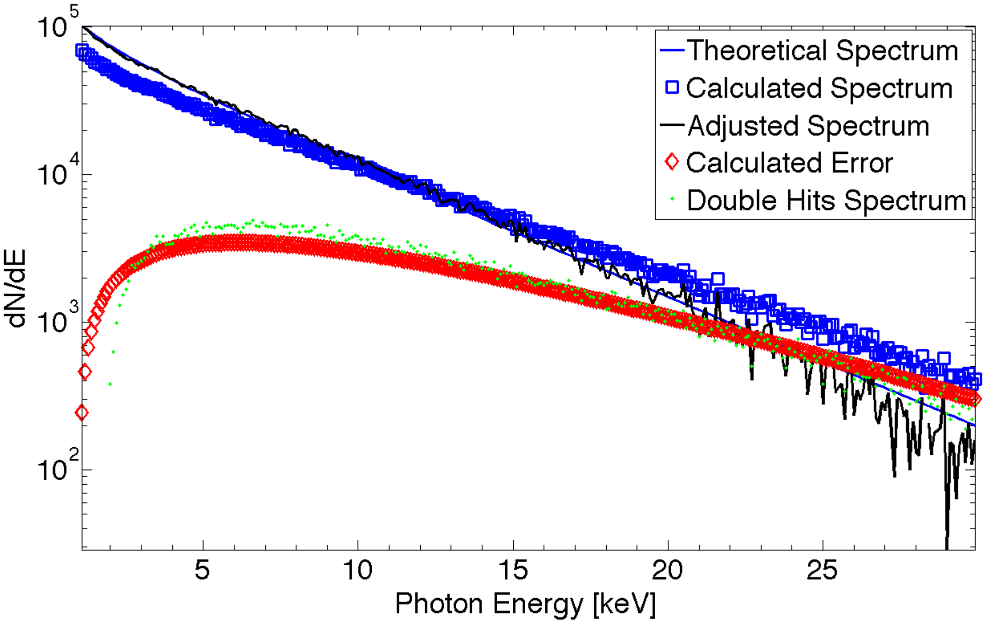

Figure A.1: An example of a betatron spectrum corrected for double-hits. The double-hits present in the calculated spectrum is corrected so that a good agreement is found between the theoretical and adjusted spectra.

The algorithm then applies a correction to the calculated spectrum and the result is shown as the adjusted spectrum. Good agreement is obtained between the theoretical betatron spectrum and the adjusted spectrum. The green dots represent a spectrum constructed solely from double-hits and the diamond markers represent the calculated error from the double-hits spectrum that is used to correct the calculated spectrum.

APPENDIX B

List of Publications

This thesis presents work reported by the Author in the following publications:

1. **T. Z. Zhao**, K. Behm, C. F. Dong, X. Davoine, S. Y. Kalmykov, V. Petrov, V. Chvykov, P. Cummings, B. Hou, A. Maksimchuk, J. A. Nees, V. Yanovsky, A. G. R. Thomas, and K. Krushelnick. High Flux Femtosecond X-ray Emission from Controlled Generation of Annular Beams in a Laser Wakefield Accelerator. Submitted to *Physical Review Letters*.

2. **T. Z. Zhao**, K. Behm, A. Maksimchuk, J. A. Nees, V. Yanovsky, A. G. R. Thomas, and K. Krushelnick. Characterization of Electrons and X-rays Produced using Chirped Laser Pulses in a Laser Wakefield Accelerator. Submitted to *Plasma Physics and Controlled Fusion*.

3. C.F. Dong, **T. Z. Zhao**, K. Behm, P. G. Cummings, J. Nees, A. Maksimchuk, V. Yanovsky, K. Krushelnick, A. G. R. Thomas. Enhanced X-ray radiation from laser wakefield acceleration beyond the depletion length. Submitted to *Physical Review Letters*.

4. M. Vargas, W. Schumaker, Z.-H. He, **Z. Zhao**, K. Behm, V. Chvykov, B. Hou, K. Krushelnick, A. Maksimchuk, V. Yanovsky, and A.G.R. Thomas. Improve-

ments to Laser Wakefield Accelerated Electron Beam Stability, Divergence and Energy Spread Using 3D Printed Two-Stage Gas Cell Targets. *Applied Physics Letters*, **104**, 174103, 2014.

The Author has also participated in research reported in the following publications which are not presented in this thesis:

1. **T. Z. Zhao**, T. Batson, B. Hou, J. A. Nees, A. G. R. Thomas, and K. Krushelnick. Characterization of Hard X-ray Sources Produced via the Interaction of Relativistic Femtosecond Laser Pulses with Metallic Targets. Submitted to *Physics of Plasmas*.

2. K. Behm, **T. Z. Zhao**, A. Maksimchuk, J. A. Nees, V. Yanovsky, K. Krushelnick, A. G. R. Thomas, J. M. Cole, J. Wood, and S. P. D. Mangles. Ionization Injection Effects in X-ray Spectra Generated by Betatron Oscillations in a Laser Wakefield Accelerator. *Plasma Physics and Controlled Fusion*, **58**, 055012, 2016.

3. L. Willingale, A. Maksimchuk, A. V. Arefiev, M. J.-E. Manuel, G. J. Williams, E. Marley, C. Zulick, W. Nazarov, F. J. Dollar, **T. Z. Zhao**, A. U. Hazi, and H. Chen. The Unexpected Role of Evolving Longitudinal Electric Fields in Generating Energetic Electrons in Relativistically Transparent Plasmas. Submitted to *Physical Review Letters*.

4. C. A. Di Stefano, C. C. Kuranz, J. F. Seely, A. G. R. Thomas, R. P. Drake, P. A. Keiter, G. J. Williams, J. Park, H. Chen, M. J. MacDonald, A. M. Rasmus, W. C. Wan, N. R. Pereira, A. S. Joglekar, A. McKelvey, **Z. Zhao**, S. R. Klein, G. E. Kemp, L. C. Jarrott, C. M. Krauland, J. Peebles, and B. Westover. Measurements of the energy spectrum of electrons emanating from solid materials irradiated by a picosecond laser. *Physics of Plasmas*, **22**, 043113, 2015.

5. G. Sarri, D. J. Corvan, W. Schumaker, J. Cole, A. Di Piazza, H. Ahmed, C. Harvey, C. H. Keitel, K. Krushelnick, S. P. D. Mangles, Z. Najmudin, D. Symes, A. G. R. Thomas, M. Yeung, **Z. Zhao**, and M. Zepf. Ultra-high Brilliance Multi-MeV Gamma-ray Beam from Non-Linear Thomson Scattering. *Physical Review Letters*, **113**, 224801, 2014.

6. W. Schumaker, G. Sarri, M. Vargas, **Z. Zhao**, K. Behm, V. Chvykov, B. Dromey, B. Hou, A. Maksimchuk, J. Nees, V. Yanovsky, M. Zepf, A.G.R. Thomas, and K. Krushelnick. Measurements of high-energy radiation generation from laser-wakefield accelerated electron beams. *Physics of Plasmas*, **21**, 056704, 2014.

7. C. Zulick, B. Hou, F. Dollar, A. Maksimchuk, J. Nees, A.G.R. Thomas, **Z. Zhao**, and K. Krushelnick. High resolution bremsstrahlung and fast electron characterization in ultrafast intense laser-solid interactions. *New Journal of Physics*, **15**, 123038, 2013.

BIBLIOGRAPHY

BIBLIOGRAPHY

[1] W. C. Röentgen. On a new kind of rays. *Nature*, **53**:274, 1896.

[2] Soft x-ray materials science (sxr). `https://portal.slac.stanford.edu/sites/lcls_public/Instruments/SXR/Pages/Specifications.aspx`. Accessed: 2016-03-23.

[3] Facts and figures. `http://www.xfel.eu/overview/facts_and_figures/`. Accessed: 2016-03-23.

[4] Compact linear collider in a nutshell. `http://clic-study.web.cern.ch/content/clic-nutshell`, . Accessed: 2016-03-23.

[5] The compact linear collider study. `http://clic-meeting.web.cern.ch/clic-meeting/CTF3_Coordination_Mtg/Table_MoU.htm`, . Accessed: 2016-03-24.

[6] Roberto Corsini. CLIC plans for the next european strategy update, and beyond. `http://clic-study.web.cern.ch/content/latest-general-presentations`. Accessed: 2016-03-24.

[7] D. Strickland and G. Mourou. Compression of amplified chirped optical pulses. *Opt. Commun.*, **55**:6, 1985.

[8] P. Gibbon. *Short Pulse Laser Interactions with Matter*. Imperial College Press, London, 2005.

[9] S. P. D. Mangles, C. D. Murphy, Z. Najmudin, A. G. R. Thomas, J. L. Collier, A. E. Dangor, E. J. Divall, P. S. Foster, J. G. Gallacher, C. J. Hooker, D. A. Jaroszynski, A. J. Langley, W. B. Mori, P. A. Norreys, F. S. Tsung, R. Viskup, B. R. Walton, and K. Krushelnick. Monoenergetic beams of relativistic electrons from intense laser plasma interactions. *Nature*, **431**:535, 2004.

[10] C. G. R. Geddes, Cs. Toth, J. van Tilborg, E. Esarey, C. B. Schroeder, D. Bruhwiler, C. Nieter, J. Cary, and W. P. Leemans. High-quality electron beams from a laser wakefield accelerator using plasma-channel guiding. *Nature*, **431**:538, 2004.

[11] J. Faure, Y. Gilnec, A. Pukhov, S. Kiselev, S. Gordienko, E. Lefebvre, J.-P. Rousseau, F. Burgy, and V. Malka. A laser-plasma accelerator producing monoenergetic electron beams. *Nature*, **431**:541, 2004.

[12] S. Kneip, C. McGuffey, F. Dollar, M. S. Bloom, V. Chvykov, G. Kalintchenko, K. Krushelnick, A. Maksimchuk, S. P. D. Mangles, T. Matsuoka, Z. Najmudin, C. A. J. Palmer, J. Schreiber, W. Schumaker, A. G. R. Thomas, and V. Yanovsky. X-ray phase contrast imaging of biological specimens with femtosecond pulses of betatron radiation from a compact laser plasma wakefield accelerator. *Appl. Phys. Lett.*, **99**:9, 2011.

[13] S. Fourmaux, S. Corde, K. Ta Phuoc, P. Lassonde, G. Lebrun, S. Payeur, F. Martin, S. Sebban, V. Malka, A. Rousse, and J. C. Kieffer. Single shot phase contrast imaging using laser-produced betatron x-ray beams. *Opt. Lett.*, **36**:13, 2013.

[14] W. L. Kruer. *The Physics of Laser Plasma Interactions.* Westview Press, Boulder, Colorado, 2003.

[15] P. Gibbon and E. Förster. Short-pulse laser-plasma interactions. *Plasma Phys. Control. Fusion*, **38**:769, 1996.

[16] S. C. Wilks and W. L. Kruer. Absorption of ultrashort, ultra-intense laser light by solids and overdense plasmas. *IEEE J. Quantum Electron.*, **33**:1954, 1997.

[17] W. L. Kruer and S. C. Wilks. Introduction to ultraintense laser plasma interactions. *AIP Conf. Proc.*, **314**:16, 1994.

[18] E. Esarey, C. B. Schroeder, and W. P. Leemans. Physics of laser-driven plasma-based electron accelerators. *Rev. Mod. Phys.*, **81**:1229, 2009.

[19] S. Corde, K. Ta Phuoc, G. Lambert, R. Fitour, V. Malka, A. Rousse, A. Beck, and E. Lefebvre. Femtosecond x rays from laser-plasma accelerators. *Rev. Mod. Phys.*, **85**:1, 2013.

[20] W. B. Mori. The physics of nonlinear optics of plasmas at relativistic intensities for short-pulse lasers. *IEEE J. Quantum Electron*, **33**:1942, 1997.

[21] A. Einstein. Über einen die Erzeugung und Verwandlung des Lichtes betreffenden heuristischen Gesichtspunkt. *Annalen der Physik*, **322**:132, 1905.

[22] M. Göppert-Mayer. Über Elementarakte mit zwei Quantensprüngen. *Annalen der Physik*, **401**:273, 1931.

[23] G. Mainfray and C. Manus. Multiphoton ionization of atoms. *Rev. Mod. Phys.*, **54**:1333, 1991.

[24] L. V. Keldysh. Ionization in the field of a strong electromagnetic wave. *Sov. Phys. JETP*, **20**:1307, 1965.

[25] A. I. Akhiezer and R. V. Polovin. Theory of wave motion in an electron plasma. *Sov. Phys. JETP*, **3**:696, 1956.

[26] E. Esarey and M. Pilloff. Trapping and acceleration in nonlinear plasma waves. *Phys. Plasmas*, **2**:1432, 1995.

[27] C. B. Schroeder, E. Esarey, and B. A. Shadwick. Warm wave breaking of nonlinear plasma waves with arbitrary phase velocities. *Phys. Rev. E*, **72**:055401, 2005.

[28] S. V. Bulanov, F. Pegoraro, A. M. Pukhov, and A. S. Sakharov. Transverse-wake wave breaking. *Phys. Rev. Lett.*, **78**:4205, 1997.

[29] P. Sprangle, C. M. Tang, and E. Esarey. Relativistic self-focusing of short-pulse radiation beams in plasmas. *IEEE Trans. Plasma Sci.*, **PS-15**:145, 1987.

[30] P. Sprangle, E. Esarey, and A. Ting. Nonlinear interaction of intense laser pulses in plasmas. *Phys. Rev. A*, **41**:4463, 1990.

[31] K. Krushelnick, A. Ting, C. I. Moore, H. R. Burris, E. Esarey, P. Sprangle, and M. Baine. Plasma channel formation and guiding during high intensity short pulse laser plasma experiments. *Phys. Rev. Lett.*, **78**:4047, 1997.

[32] W. P. Leemans, P. Catravas, E. Esarey, C. G. R. Geddes, C. Toth, R. Trines, C. B. Schroeder, B. A. Shadwick, J. van Tilborg, and J. Faure. Electron-yield enhancement in a laser-wakefield accelerator driven by asymmetric laser pulses. *Phys. Rev. Lett.*, **89**:174802, 2002.

[33] B. Hafizi, A. Ting, P. Sprangle, and R. F. Hubbard. Relativistic focusing and ponderomotive channeling of intense laser beams. *Phys. Rev. E*, **62**:4120, 2000.

[34] A. Ting, E. Esarey, and P. Sprangle. Nonlinear wakefield generation and relativistic focusing of intense laser pulses in plasmas. *Physics of Fluids B*, **2**:1390, 1990.

[35] K. Krushelnick, C. I. Moore, A. Ting, and H. R. Burris. Frequency mixing of high intensity laser light with stimulated raman backscattered radiation in underdense plasmas. *Phys. Rev. E*, **58**:4030, 1998.

[36] C. Joshi, T. Tajima, J. M. Dawson, H. A. Baldis, and N. A. Ebrahim. Forward raman instability and electron acceleration. *Phys. Rev. Lett.*, **47**:1285, 1981.

[37] P. Bertrand, A. Ghizzo, S. J. Karttunen, T. J. H. Pättikangas, R. R. E. Salomaa, and M. Shoucri. Two stage electron acceleration by simultaneous stimulated raman backward and forward scattering. *Physics of Plasmas*, **2**:3115, 1995.

[38] T. Tajima and J. M. Dawson. Laser electron accelerator. *Phys. Rev. Lett.*, **43**:267, 1979.

[39] GuoZheng Sun, Edward Ott, Y. C. Lee, and Parvez Guzdar. Self-focusing of short intense pulses in plasmas. *Physics of Fluids*, **30**:526, 1987.

[40] E. Esarey and A. Ting. Comment on "cascade focusing in the beat-wave accelerator". *Phys. Rev. Lett.*, **65**:1961, 1990.

[41] J. Krall, A. Ting, E. Esarey, and P. Sprangle. Enhanced acceleration in a self-modulated-laser wake-field accelerator. *Phys. Rev. E*, **48**:2157, 1993.

[42] T. Auguste, P. Monot, L.-A. Lompre, G. Mainfray, and C. Manus. Defousing effects of a picosecond terawatt laser pulse in an underdense plasma. *Optics Commun.*, **89**:145, 1992.

[43] M. Born and E. Wolf. *Principles of Optics.* Cambridge University Press, England, 7 edition, 1999.

[44] S. P. D. Mangles, G. Genoud, M. S. Bloom, M. Burza, Z. Najmudin, A. Persson, K. Svensson, A. G. R. Thomas, and C.-G. Wahlström. Self-injection threshold in self-guided laser wakefield accelerators. *Phys. Rev. ST Accel. Beams*, **15**: 011302, 2012.

[45] S. Y. Kalmykov, X. Davoine, R. Lehe, A. F. Lifschitz, and B. A. Shadwick. Optical control of electron phase space in plasma accelerators with incoherently stacked laser pulses. *Physics of Plasmas*, **22**:56701, 2015.

[46] Loren C. Steinhauer and Wayne D. Kimura. A new approach for laser particle acceleration in vacuum. *Journal of Applied Physics*, **72**:3237, 1992.

[47] Eric Esarey, Phillip Sprangle, and Jonathan Krall. Laser acceleration of electrons in vacuum. *Phys. Rev. E*, **52**:5443, 1995.

[48] W. D. Kimura, G. H. Kim, R. D. Romea, L. C. Steinhauer, I. V. Pogorelsky, K. P. Kusche, R. C. Fernow, X. Wang, and Y. Liu. Laser acceleration of relativistic electrons using the inverse cherenkov effect. *Phys. Rev. Lett.*, **74**: 546, 1995.

[49] Phillip Sprangle, Eric Esarey, and Jonathan Krall. Laser driven electron acceleration in vacuum, gases, and plasmas. *Physics of Plasmas*, **3**:2183, 1996.

[50] Pisin Chen, J. M. Dawson, Robert W. Huff, and T. Katsouleas. Acceleration of electrons by the interaction of a bunched electron beam with a plasma. *Phys. Rev. Lett.*, **54**:693, 1985.

[51] R. Ruth, A. Chao, P. Morton, and P. Wilson. A plasma wake field accelerator. *Particle Accelerators*, **17**:171, 1985.

[52] S. C. Wilks, J. M. Dawson, W. B. Mori, T. Katsouleas, and M. E. Jones. Photon accelerator. *Phys. Rev. Lett.*, **62**:2600, 1989.

[53] A. Pukhov and J. Meyer-ter Vehn. Laser wake field acceleration: the highly non-linear broken-wave regime. *Applied Physics B*, **74**:355, 2002.

[54] J. B. Rosenzweig, B. Breizman, T. Katsouleas, and J. J. Su. Acceleration and focusing of electrons in two-dimensional nonlinear plasma wake fields. *Phys. Rev. A*, **44**:R6189, 1991.

[55] V. Malka, S. Fritzler, E. Lefebvre, M.-M. Aleonard, F. Burgy, J.-P. Chambaret, J.-F. Chemin, K. Krushelnick, G. Malka, S. P. D. Mangles, Z. Najmudin, M. Pittman, J.-P. Rousseau, J.-N. Scheurer, B. Walton, and A. E. Dangor. Electron acceleration by a wake field forced by an intense ultrashort laser pulse. *Science*, **298**:1596, 2002.

[56] S. Kalmykov, S. A. Yi, V. Khudik, and G. Shvets. Electron self-injection and trapping into an evolving plasma bubble. *Phys. Rev. Lett.*, **103**:135004, 2009.

[57] I. Kostyukov, E. Nerush, A. Pukhov, and V. Seredov. Electron self-injection in multidimensional relativistic-plasma wake fields. *Phys. Rev. Lett.*, **103**:175003, 2009.

[58] D. H. Froula, C. E. Clayton, T. Döppner, K. A. Marsh, C. P. J. Barty, L. Divol, R. A. Fonseca, S. H. Glenzer, C. Joshi, W. Lu, S. F. Martins, P. Michel, W. B. Mori, J. P. Palastro, B. B. Pollock, A. Pak, J. E. Ralph, J. S. Ross, C. W. Siders, L. O. Silva, and T. Wang. Measurements of the critical power for self-injection of electrons in a laser wakefield accelerator. *Phys. Rev. Lett.*, **103**:215006, 2009.

[59] T. Katsouleas, S. Wilks, P. Chen, J. M. Dawson, and J. J. Su. Plasma wakefield acceleration utilizing multiple election bunches. *Particle Accelerators*, **22**:81, 1987.

[60] M. Tzoufras, W. Lu, F. S. Tsung, C. Huang, W. B. Mori, T. Katsouleas, J. Vieira, R. A. Fonseca, and L. O. Silva. Beam loading in the nonlinear regime of plasma-based acceleration. *Phys. Rev. Lett.*, **101**:145002, 2008.

[61] C. Rechatin, X. Davoine, A. Lifschitz, A. Ben Ismail, J. Lim, E. Lefebvre, J. Faure, and V. Malka. Observation of beam loading in a laser-plasma accelerator. *Phys. Rev. Lett.*, **103**:194804, 2009.

[62] C. McGuffey, A. G. R. Thomas, W. Schumaker, T. Matsuoka, V. Chvykov, F. J. Dollar, G. Kalintchenko, V. Yanovsky, A. Maksimchuk, K. Krushelnick, V. Yu. Bychenkov, I. V. Glazyrin, and A. V. Karpeev. Ionization induced trapping in a laser wakefield accelerator. *Phys. Rev. Lett.*, **104**:025004, 2010.

[63] A. Pak, K. A. Marsh, S. F. Martins, W. Lu, W. B. Mori, and C. Joshi. Injection and trapping of tunnel-ionized electrons into laser-produced wakes. *Phys. Rev. Lett.*, **104**:025003, 2010.

[64] S. Bulanov, N. Naumova, F. Pegoraro, and J. Sakai. Particle injection into the wave acceleration phase due to nonlinear wake wave breaking. *Phys. Rev. E*, **58**:R5257, 1998.

[65] C. G. R. Geddes, K. Nakamura, G. R. Plateau, Cs. Toth, E. Cormier-Michel, E. Esarey, C. B. Schroeder, J. R. Cary, and W. P. Leemans. Plasma-density-gradient injection of low absolute-momentum-spread electron bunches. *Phys. Rev. Lett.*, **100**:215004, 2008.

[66] J. Faure, C. Rechatin, O. Lundh, L. Ammoura, and V. Malka. Injection and acceleration of quasimonoenergetic relativistic electron beams using density gradients at the edges of a plasma channel. *Physics of Plasmas*, **17**:083107, 2010.

[67] K. Schmid, A. Buck, C. M. S. Sears, J. M. Mikhailova, R. Tautz, D. Herrmann, M. Geissler, F. Krausz, and L. Veisz. Density-transition based electron injector for laser driven wakefield accelerators. *Phys. Rev. ST Accel. Beams*, **13**:091301, 2010.

[68] T.-Y. Chien, C.-L. Chang, C.-H. Lee, J.-Y. Lin, J. Wang, and S.-Y. Chen. Spatially localized self-injection of electrons in a self-modulated laser-wakefield accelerator by using a laser-induced transient density ramp. *Phys. Rev. Lett.*, **94**:115003, 2005.

[69] C. D. Decker, W. B. Mori, K.C. Tzeng, and T. Katsouleas. The evolution of ultra intense, shortpulse lasers in underdense plasmas. *Physics of Plasmas*, **3**: 2047, 1996.

[70] W. Lu, M. Tzoufras, C. Joshi, F. S. Tsung, W. B. Mori, J. Vieira, R. A. Fonseca, and L. O. Silva. Generating multi-gev electron bunches using single stage laser wakefield acceleration in a 3d nonlinear regime. *Phys. Rev. ST Accel. Beams*, **10**:061301, 2007.

[71] S. Kiselev, A. Pukhov, and I. Kostyukov. X-ray generation in strongly nonlinear plasma waves. *Phys. Rev. Lett.*, **93**:135004, 2004.

[72] Antoine Rousse, Kim Ta Phuoc, Rahul Shah, Alexander Pukhov, Eric Lefebvre, Victor Malka, Sergey Kiselev, Fréderic Burgy, Jean-Philippe Rousseau, Donald Umstadter, and Daniéle Hulin. Production of a kev x-ray beam from synchrotron radiation in relativistic laser-plasma interaction. *Phys. Rev. Lett.*, **93**:135005, 2004.

[73] Félicie Albert, Rahul Shah, Kim Ta Phuoc, Romuald Fitour, Fréderic Burgy, Jean-Philippe Rousseau, Amar Tafzi, Denis Douillet, Thierry Lefrou, and Antoine Rousse. Betatron oscillations of electrons accelerated in laser wakefields characterized by spectral x-ray analysis. *Phys. Rev. E*, **77**:056402, 2008.

[74] O. Lundh, J. Lim, C. Rechatin, L. Ammoura, A. Ben-Isamil, X. Davoine, G. Gallot, J-P. Goddet, E. Lefebvre, V. Malka, and J. Faure. Few femtosecond, few kiloampere electron bunch produced by a laser-plasma accelerator. *Nat. Phys.*, **7**:219, 2011.

[75] S. Kneip, C. McGuffey, J. L. Martins, M. S. Bloom, V. Chvykov, F. Dollar, R. Fonseca, S. Jolly, G. Kalintchenko, K. Krushelnick, A. Maksimchuk, S. P. D. Mangles, Z. Najmudin, C. A. J. Palmer, K. Ta Phuoc, W. Schumaker, L. O. Silva, J. Vieira, V. Yanovsky, and A. G. R. Thomas. Characterization of transverse beam emittance of electrons from a laser-plasma wakefield accelerator in the bubble regime using betatron x-ray radiation. *Phys. Rev. ST Accel. Beams*, **15**:021302, 2012.

[76] S. Kneip, C. McGuffey, J. L. Martins, S. F. Martins, C. Bellei, V. Chvykov, F. Dollar, R. Fonseca, C. Huntington, G. Kalintchenko, A. Maksimchuk, S. P. D. Mangles, T. Matsuoka, S. R. Nagel, C. J. Palmer, J. Schreiber, K. Ta Phuoc, A. G. R. Thomas, V. Yanovsky, L. O. Silva, K. Krushelnick, and Z. Najmduin. Bright spatially coherent synchrotron x-rays from a table-top source. *Nat. Phys.*, **6**:980, 2010.

[77] J. D. Jackson. *Classical Electrodynamics*. Wiley, New York, 3 edition, 2001.

[78] I. Kostyukov, A. Pukhov, and S. Kiselev. Phenomenological theory of laser-plasma interaction in bubble regime. *Physics of Plasmas*, **11**:5256, 2004.

[79] A. G. R. Thomas. Scalings for radiation from plasma bubbles. *Physics of Plasmas*, **17**:056708, 2010.

[80] E. Treacy. Optical pulse compression with diffraction gratings. *IEEE Journal of Quantum Electronics*, **5**:454, 1969.

[81] O. Martinez. Design of high-power ultrashort pulse amplifiers by expansion and recompression. *IEEE Journal of Quantum Electronics*, **23**:1385, 1987.

[82] P. S. Banks, M. D. Perry, V. Yanovsky, S. N. Fochs, B. C. Stuart, and J. Zweiback. Novel all-reflective stretcher for chirped-pulse amplification of ultrashort pulses. *IEEE Journal of Quantum Electronics*, **36**:268, 2000.

[83] Experimental facilities. `http://cuos.engin.umich.edu/researchgroups/hfs/facilities/`. Accessed: 2016-04-04.

[84] V. Yanovsky, V. Chvykov, G. Kalinchenko, P. Rousseau, T. Planchon, T. Matsuoka, A. Maksimchuk, J. Nees, G. Cheriaux, G. Mourou, and K. Krushelnick. Ultra-high intensity-300-tw laser at 0.1 hz repetition rate. *Opt. Express*, **16**: 2109, 2008.

[85] V. Chvykov, P. Rousseau, S. Reed, G. Kalinchenko, and V. Yanovsky. Generation of 10^{11} contrast 50 tw laser pulses. *Opt. Lett.*, **31**:1456, 2006.

[86] F. Dollar, T. Matsuoka, G. M. Petrov, A. G. R. Thomas, S. S. Bulanov, V. Chvykov, J. Davis, G. Kalinchenko, C. McGuffey, L. Willingale, V. Yanovsky, A. Maksimchuk, and K. Krushelnick. Control of energy spread and dark current in proton and ion beams generated in high-contrast laser solid interactions. *Phys. Rev. Lett.*, **107**:065003, 2011.

[87] X. Liu, R. Wagner, A. Maksimchuk, E. Goodman, J. Workman, D. Umstadter, and A. Migus. Nonlinear temporal diffraction and frequency shifts resulting from pulse shaping in chirped-pulse amplification systems. *Opt. Lett.*, **20**:1163, 1995.

[88] R. N. Gyuzalian, S. B. Sogomonian, and Z.Gy. Horvath. Background-free measurement of time behaviour of an individual picosecond laser pulse. *Optics Communications*, **29**:239, 1979.

[89] Rick Trebino, Kenneth W. DeLong, David N. Fittinghoff, John N. Sweetser, Marco A. Krumbgel, Bruce A. Richman, and Daniel J. Kane. Measuring ultrashort laser pulses in the time-frequency domain using frequency-resolved optical gating. *Review of Scientific Instruments*, **68**:3277, 1997.

[90] Tutorials. `http://www.swampoptics.com/tutorials.html`. Accessed: 2016-04-04.

[91] C. S. McGuffey. *Studies of Laser Guiding and Electron Injection in a High Power Laser Wakefield Accelerator*. PhD thesis, University of Michigan, 2011.

[92] W. A. Schumaker. *Pump-Probe Experiments & Radiation Generation using Laser Wakefield Accelerators*. PhD thesis, University of Michigan, 2014.

[93] M. Vargas, W. Schumaker, Z.-H. He, Z. Zhao, K. Behm, V. Chvykov, B. Hou, K. Krushelnick, A. Maksimchuk, V. Yanovsky, and A. G. R. Thomas. Improvements to laser wakefield accelerated electron beam stability, divergence, and energy spread using three-dimensional printed two-stage gas cell targets. *Applied Physics Letters*, **104**:174103, 2014.

[94] A. J. Gonsalves, K. Nakamura, C. Lin, D. Panasenko, S. Shiraishi, T. Sokollik, C. Benedetti, C. B. Schroeder, C. G. R. Geddes, J. Van Tilborg, J. Osterhoff, E. Esarey, C. Toth, and W. P. Leemans. Tunable laser plasma accelerator based on longitudinal density tailoring. *Nature Physics*, **7**:862, 2011.

[95] V. P. Kulesh. Measurement of gas density by heterodyne interferometry. *Measurement Techniques*, **39**:162, 1996.

[96] Mitsuo Takeda, Hideki Ina, and Seiji Kobayashi. Fourier-transform method of fringe-pattern analysis for computer-based topography and interferometry. *J. Opt. Soc. Am.*, **72**:156, 1982.

[97] P. Tomassini and A. Giulietti. A generalization of abel inversion to non-axisymmetric density distribution. *Optics Communications*, **199**:143, 2001.

[98] Hui Chen, Norman L. Back, Teresa Bartal, F. N. Beg, David C. Eder, Anthony J. Link, Andrew G. MacPhee, Yuan Ping, Peter M. Song, Alan Throop, and Linn Van Woerkom. Absolute calibration of image plates for electrons at energy between 100 keV and 4 MeV. *Review of Scientific Instruments*, **79**: 033301, 2008.

[99] B. R. Maddox, H. S. Park, B. A. Remington, N. Izumi, S. Chen, C. Chen, G. Kimminau, Z. Ali, M. J. Haugh, and Q. Ma. High-energy x-ray backlighter spectrum measurements using calibrated image plates. *Review of Scientific Instruments*, **82**:023111, 2011.

[100] C. G. Freeman, G. Fiksel, C. Stoeckl, N. Sinenian, M. J. Canfield, G. B. Graeper, A. T. Lombardo, C. R. Stillman, S. J. Padalino, C. Mileham, T. C. Sangster, and J. A. Frenje. Calibration of a thomson parabola ion spectrometer and fujifilm imaging plate detectors for protons, deuterons, and alpha particles. *Review of Scientific Instruments*, **82**:073301, 2011.

[101] M. J. Haugh, J. Lee, E. Romano, and M. Schneider. Calibrating image plate sensitivity in the 700 to 5000 ev spectral energy range. In *Proc. SPIE*, volume **8850**, page 885007, 2013.

[102] G. Fiksel, F. J. Marshall, C. Mileham, and C. Stoeckl. Note: Spatial resolution of Fuji BAS-TR and BAS-SR imaging plates. *Review of Scientific Instruments*, **83**:086103, 2012.

[103] K. Zeil, S. D. Kraft, A. Jochmann, F. Kroll, W. Jahr, U. Schramm, L. Karsch, J. Pawelke, B. Hidding, and G. Pretzler. Absolute response of fuji imaging plate detectors to picosecond-electron bunches. *Review of Scientific Instruments*, **81**: 013307, 2010.

[104] S Fourmaux, S Corde, K Ta Phuoc, P M Leguay, S Payeur, P Lassonde, S Gnedyuk, G Lebrun, C Fourment, V Malka, S Sebban, A Rousse, and J C Kieffer. Demonstration of the synchrotron-type spectrum of laser-produced betatron radiation. *New Journal of Physics*, **13**:033017, 2011.

[105] C. Fourment, N. Arazam, C. Bonte, T. Caillaud, D. Descamps, F. Dorchies, M. Harmand, S. Hulin, S. Petit, and J. J. Santos. Broadband, high dynamics and high resolution charge coupled device-based spectrometer in dynamic mode for multi-kev repetitive x-ray sources. *Review of Scientific Instruments*, **80**: 083505, 2009.

[106] Nudat 2.6. `http://www.nndc.bnl.gov/nudat2/`. Accessed: 2016-04-07.

[107] J. M. Dawson. Particle simulation of plasmas. *Rev. Mod. Phys.*, **55**:403, 1983.

[108] R. A. Fonseca, L. O. Silva, F. S. Tsung, V. K. Decyk, W. Lu, C. Ren, W. B. Mori, S. Deng, S. Lee, T. Katsouleas, and J. C. Adam. *Computational Science — ICCS 2002: International Conference Amsterdam, The Netherlands, April 21–24, 2002 Proceedings, Part III*, chapter OSIRIS: A Three-Dimensional, Fully Relativistic Particle in Cell Code for Modeling Plasma Based Accelerators, page 342. Springer Berlin Heidelberg, 2002.

[109] S. Y. Kalmykov, A. Beck, S. A. Yi, V. N. Khudik, M. C. Downer, E. Lefebvre, B. A. Shadwick, and D. P. Umstadter. Electron self-injection into an evolving

plasma bubble: Quasi-monoenergetic laser-plasma acceleration in the blowout regimea). *Physics of Plasmas*, **18**:056704, 2011.

[110] A. Pukhov, Z.-M. Sheng, and J. Meyer-ter Vehn. Particle acceleration in relativistic laser channels. *Physics of Plasmas*, **6**:2847, 1999.

[111] Cs. Tóth, J. Faure, J. van Tilborg, C. G. R. Geddes, C. B. Schroeder, E. Esarey, and W. P. Leemans. Tuning of laser pulse shapes in grating-based compressors for optimal electron acceleration in plasmas. *Opt. Lett.*, **28**:1823, 2003.

[112] A. Spitkovsky and P. Chen. Longitudinal laser shaping in laser wakefield accelerators. *Physics Letters A*, **296**:125, 2002.

[113] V. B. Pathak, J. Vieira, R. A. Fonseca, and L. O. Silva. Effect of the frequency chirp on laser wakefield acceleration. *New Journal of Physics*, **14**:023057, 2012.

[114] Evan S. Dodd and D. Umstadter. Coherent control of stimulated raman scattering using chirped laser pulses. *Physics of Plasmas*, **8**:3531, 2001.

[115] C. B. Schroeder, E. Esarey, C. G. R. Geddes, Cs. Tth, B. A. Shadwick, J. van Tilborg, J. Faure, and W. P. Leemans. Frequency chirp and pulse shape effects in self-modulated laser wakefield accelerators. *Physics of Plasmas*, **10**:2039, 2003.

[116] B. S. Rao, A. Moorti, P. A. Naik, and P. D. Gupta. Effect of chirp on self-modulation and laser wakefield electron acceleration in the regime of quasimonoenergetic electron beam generation. *Phys. Rev. ST Accel. Beams*, **16**:091301, 2013.

[117] K. W. DeLong, R. Trebino, J. Hunter, and W. E. White. Frequency-resolved optical gating with the use of second-harmonic generation. *J. Opt. Soc. Am. B*, **11**:2206, 1994.

[118] J. Krall, E. Esarey, P. Sprangle, and G. Joyce. Propagation of radiustailored laser pulses over extended distances in a uniform plasma*. *Physics of Plasmas*, **1**:1738, 1994.

[119] Daniel Herrmann, Laszlo Veisz, Raphael Tautz, Franz Tavella, Karl Schmid, Vladimir Pervak, and Ferenc Krausz. Generation of sub-three-cycle, 16 TW light pulses by using noncollinear optical parametric chirped-pulse amplification. *Opt. Lett.*, **34**:2459, 2009.

[120] Andrew M. Weiner. Ultrafast optical pulse shaping: A tutorial review. *Optics Communications*, **284**:3669, 2011.

[121] Xiaomei Zhang, Baifei Shen, Liangliang Ji, Wenpeng Wang, Jiancai Xu, Yahong Yu, Longqing Yi, Xiaofeng Wang, Nasr A. M. Hafz, and V. Kulagin. Effect of pulse profile and chirp on a laser wakefield generation. *Physics of Plasmas*, **19**: 053103, 2012.

[122] A. G. R. Thomas, Z. Najmudin, S. P. D. Mangles, C. D. Murphy, A. E. Dangor, C. Kamperidis, K. L. Lancaster, W. B. Mori, P. A. Norreys, W. Rozmus, and K. Krushelnick. Effect of laser-focusing conditions on propagation and monoenergetic electron production in laser-wakefield accelerators. *Phys. Rev. Lett.*, **98**: 095004, 2007.

[123] S. Banerjee, S. Y. Kalmykov, N. D. Powers, G. Golovin, V. Ramanathan, N. J. Cunningham, K. J. Brown, S. Chen, I. Ghebregziabher, B. A. Shadwick, D. P. Umstadter, B. M. Cowan, D. L. Bruhwiler, A. Beck, and E. Lefebvre. Stable, tunable, quasimonoenergetic electron beams produced in a laser wakefield near the threshold for self-injection. *Phys. Rev. ST Accel. Beams*, **16**:031302, 2013.

[124] Z-H He, B. Hou, J. A. Nees, J. H. Easter, J. Faure, K. Krushelnick, and A. G. R. Thomas. High repetition-rate wakefield electron source generated by few-millijoule, 30 femtosecond laser pulses on a density downramp. *New J. Phys.*, **15**:053016, 2013.

[125] A. Buck, J. Wenz, J. Xu, K. Khrennikov, K. Schmid, M. Heigoldt, J. M. Mikhailova, M. Geissler, B. Shen, F. Krausz, S. Karsch, and L. Veisz. Shock-front injector for high-quality laser-plasma acceleration. *Phys. Rev. Lett.*, **110**: 185006, 2013.

[126] F. Y. Li, Z. M. Sheng, Y. Liu, J. Meyer-ter Vehn, W. B. Mori, W. Lu, and J. Zhang. Dense attosecond electron sheets from laser wakefields using an up-ramp density transition. *Phys. Rev. Lett.*, **110**:135002, 2013.

[127] D. Kaganovich, D. F. Gordon, M. H. Helle, and A. Ting. Shaping gas jet plasma density profile by laser generated shock waves. *Journal of Applied Physics*, **116**: 13304, 2014.

[128] B. B. Pollock, F. S. Tsung, F. Albert, J. L. Shaw, C. E. Clayton, A. Davidson, N. Lemos, K. A. Marsh, A. Pak, J. E. Ralph, W. B. Mori, and C. Joshi. Formation of ultrarelativistic electron rings from a laser-wakefield accelerator. *Phys. Rev. Lett.*, **115**:055004, 2015.

[129] P. E. Masson-Laborde, M. Z. Mo, A. Ali, S. Fourmaux, P. Lassonde, J. C. Kieffer, W. Rozmus, D. Teychenn, and R. Fedosejevs. Giga-electronvolt electrons due to a transition from laser wakefield acceleration to plasma wakefield acceleration. *Physics of Plasmas*, **21**:123113, 2014.

[130] A.F. Lifschitz, X. Davoine, E. Lefebvre, J. Faure, C. Rechatin, and V. Malka. Particle-in-cell modelling of laserplasma interaction using fourier decomposition. *Journal of Computational Physics*, **228**:1803, 2009.

[131] David H. Whittum, William M. Sharp, Simon S. Yu, Martin Lampe, and Glenn Joyce. Electron-hose instability in the ion-focused regime. *Phys. Rev. Lett.*, **67**: 991, 1991.

[132] E. S. Dodd, R. G. Hemker, C.-K. Huang, S. Wang, C. Ren, W. B. Mori, S. Lee, and T. Katsouleas. Hosing and sloshing of short-pulse gev-class wakefield drivers. *Phys. Rev. Lett.*, **88**:125001, 2002.

[133] C. Huang, W. Lu, M. Zhou, C. E. Clayton, C. Joshi, W. B. Mori, P. Muggli, S. Deng, E. Oz, T. Katsouleas, M. J. Hogan, I. Blumenfeld, F. J. Decker, R. Ischebeck, R. H. Iverson, N. A. Kirby, and D. Walz. Hosing instability in the blow-out regime for plasma-wakefield acceleration. *Phys. Rev. Lett.*, **99**:255001, 2007.

[134] S. Deng, C. D. Barnes, C. E. Clayton, C. O'Connell, F. J. Decker, R. A. Fonseca, C. Huang, M. J. Hogan, R. Iverson, D. K. Johnson, C. Joshi, T. Katsouleas, P. Krejcik, W. Lu, W. B. Mori, P. Muggli, E. Oz, F. Tsung, D. Walz, and M. Zhou. Hose instability and wake generation by an intense electron beam in a self-ionized gas. *Phys. Rev. Lett.*, **96**:045001, 2006.

[135] Thomas M. Antonsen and Zhigang Bian. Ionization induced scattering of short intense laser pulses. *Phys. Rev. Lett.*, **82**:3617, 1999.

[136] V. B. Gil'denburg, A. G. Litvak, and N. A. Zharova. Microfilamentation in optical-field-induced ionization process. *Phys. Rev. Lett.*, **78**:2968, 1997.

[137] P. Sprangle, E. Esarey, and J. Krall. Self-guiding and stability of intense optical beams in gases undergoing ionization. *Phys. Rev. E*, **54**:4211, 1996.

[138] N. A. M. Hafz, T. M. Jeong, I. W. Choi, S. K. Lee, K. H. Pae, V. V. Kulagin, J. H. Sung, T. J. Yu, K.-H. Hong, T. Hosokai, J. R. Cary, D.-K. Ko, and J. Lee. Stable generation of gev-class electron beams from self-guided laser-plasma channels. *Nauture Photonics*, **2**:571, 2008.

[139] W. P. Leemans, B. Nagler, A. J. Gonsalves, C. S. Toth, K. Nakamura, C. G. R. Geddes, E. Esarey, C. B. Schroeder, and S. M. Hooker. Gev electron beams from a centimetre-scale accelerator. *Nauture Physics*, **2**:696, 2006.

[140] J. Faure, C. Rechatin, A. Norlin, A. Lifschitz, Y. Glinec, and V. Malka. Controlled injection and acceleration of electrons in plasma wakefields by colliding laser pulses. *Nature*, **444**:737, 2006.

[141] Baifei Shen, Yuelin Li, Karoly Nemeth, Hairong Shang, Yong-chul Chae, Robert Soliday, Robert Crowell, Edward Frank, William Gropp, and John Cary. Electron injection by a nanowire in the bubble regime. *Physics of Plasmas*, **14**:053115, 2007.

[142] Meng Wen, Baifei Shen, Xiaomei Zhang, Liangliang Ji, Wenpeng Wang, Jiancai Xu, and Yahong Yu. Generation of high charged energetic electrons by using multiparallel laser pulses. *Physics of Plasmas*, **17**:103113, 2010.

[143] Y. Ma, L. M. Chen, M. H. Li, Y. F. Li, J. G. Wang, M. Z. Tao, Y. J. Han, J. R. Zhao, K. Huang, W. C. Yan, D. Z. Li, Z. Y. Chen, J. L. Ma, Y. T. Li, Z. M. Sheng, and J. Zhang. Multiple quasi-monoenergetic electron beams from laser-wakefield acceleration with spatially structured laser pulse. *Physics of Plasmas*, **22**:083102, 2015.

[144] J. Vieira and J. T. Mendonca. Nonlinear laser driven donut wakefields for positron and electron acceleration. *Phys. Rev. Lett.*, **112**:215001, 2014.

[145] Guo-Bo Zhang, Min Chen, Ji Luo, Ming Zeng, Tao Yuan, Ji-Ye Yu, Yan-Yun Ma, Tong-Pu Yu, Lu-Le Yu, Su-Ming Weng, and Zheng-Ming Sheng. Acceleration of on-axis and ring-shaped electron beams in wakefields driven by Laguerre-Gaussian pulses. *Journal of Applied Physics*, **119**:103101, 2016.

[146] K. V. Lotov. Acceleration of positrons by electron beam-driven wakefields in a plasma. *Physics of Plasmas*, **14**, 2007.

[147] S. Lee, T. Katsouleas, R. G. Hemker, E. S. Dodd, and W. B. Mori. Plasma-wakefield acceleration of a positron beam. *Phys. Rev. E*, **64**:045501, 2001.

[148] N. Jain, T. M. Antonsen, and J. P. Palastro. Positron acceleration by plasma wakefields driven by a hollow electron beam. *Phys. Rev. Lett.*, **115**:195001, 2015.